Anatomically and microstructure-informed tractography for connectivity assessment in neurological pathologies

Thomas Durantel

COLLEGE DOCTORAL BRETAGNE
MATHS, TELECOMS
INFORMATIQUE, SIGNAL
SYSTEMES, ELECTRONIQUE

Université de Rennes

THÈSE DE DOCTORAT DE

L'UNIVERSITÉ DE RENNES

ÉCOLE DOCTORALE N° 601
Mathématiques, Télécommunications, Informatique, Signal, Systèmes, Électronique
Spécialité : *Mathématiques et leurs Interactions*

Par
Thomas DURANTEL

Tractographie informée par l'anatomie et la microstructure pour l'évaluation de la connectivité dans les pathologies neurologiques

Thèse présentée et soutenue à Rennes , le 15/12/2023
Unité de recherche : IRISA - UMR 6074

Rapporteurs avant soutenance :

Jean-Philippe THIRAN	Full professor, EPFL, Lausane, Suisse
Olivier COULON	Directeur de recherche INT, Marseille

Composition du Jury :

Président :	Pierre MAUREL	Professeur des universités, INRIA, Rennes
Examinateurs :	Jean-Philippe THIRAN	Full professor, EPFL, Lausane, Suisse
	Olivier COULON	Directeur de recherche, INT, Marseille
	Ileana JELESCU	Assistant Professor, Université de Lausane, Suisse
	Rachid DERICHE	Directeur de recherche, INRIA, Sophia Antipolis
Dir. de thèse :	Julie COLOIGNER	Chargée de recherche, CNRS, Rennes
Co-dir. de thèse :	Olivier COMMOWICK†	Chargé de recherche, INRIA, Rennes

Table of Contents

RÉSUMÉ EN FRANÇAIS

Contexte

L'imagerie par résonance magnétique (IRM) est une technique efficace et non invasive qui permet une exploration complète de la structure complexe du cerveau. Combinée avec des methodes d'analyse innovante, elle permet d'estimer une veritable cartographie anatomique et fonctionnelle. Le développement continu d'approches IRM innovantes a considérablement amélioré notre capacité à quantifier l'organisation de ces réseaux cerebraux et ainsi à detecter les altérations du cerveau liées à diverses maladies, faisant progresser notre compréhension de ces altérations à un rythme rapide.

Parmi ces techniques, l'IRM de diffusion (IRMd) permet de mesurer l'agitation thermique des molécules d'eau dans le cerveau [E. Stejskal and Tanner, 1965]. Cette agitation étant contrainte par les micro-structures des tissus, typiquement les axones du système nerveux, l'IRMd permet d'estimer au niveau du voxel les orientations des fibres de la matière blanche [Dell'Acqua and Tournier, 2017 D. Jones, 2010]. En outre, l'IRM de diffusion, combinée à des techniques de tractographie, nous permet d'estimer les trajets des fibres nerveuses dans le cerveau en suivant les orientations locales des fibres voxel par voxel. L'ensemble des fibres qui en résulte est appelé tractogramme [Mori and Van Zijl, 2002]. Grace à ces techniques, nous pouvons cartographier la connectivité cérébrale et comprendre les connexions physiques qui facilitent l'échange d'informations entre les régions corticales [D. Jones, 2010]. Elles offrent un immense potentiel pour l'étude de l'anatomie, du développement, et de la fonction cérébrale [Jeurissen et al., 2019a]. Par ailleurs, il convient de souligner l'importance de la tractographie en neurochirurgie, où elle joue un rôle essentiel dans la planification chirurgicale, notamment en ce qui concerne la préservation des voies critiques de la substance blanche lors des résections cérébrales [Mancini et al., 2019]. De plus, des recherches axées sur la diffusion ont contribué à des avancées notables dans l'étude des maladies neurologiques et psychiatriques tels que la depression [Coloigner et al., 2019].

Malgré les avancées dans les techniques d'acquisition des données en IRM ainsi que dans les méthodes de tractographie, l'estimation des fibres de la matière blanche reste

confrontée à des limitations. Des recherches récentes ont mis en lumière que de nombreuses connexions ne sont pas détectées par les algorithmes de tractographie traditionnels en raison du fait que la plupart des modèles de diffusion ne permettent pas une analyse détaillée de la microstructure [D. B. Aydogan et al., 2018]. Ce problème constitue un défi essentiel, notamment dans des domaines tels que la planification chirurgicale. De plus, d'autres recherches ont indiqué que les algorithmes de tractographie les plus avancés ont tendance à generer un grand nombre de faisceaux de fibres, ce qui entraîne par conséquent un taux élevé de faux positifs. [K. Maier-Hein et al., 2017b]. Cette limitation entrave la compréhension précise des caractéristiques des réseaux présents dans le connectome cérébral [Zalesky et al., 2016].

Organisation du manuscrit

État de l'art

La première section de ce manuscrit est consacrée à un aperçu complet de l'état actuel des connaissances. Nous reviendrons sur les concepts fondamentaux qui servent de base aux sections suivantes de cette thèse.

Tout d'abord, nous débuterons en fournissant un résumé succinct de la structure organisationnelle du cerveau humain. Ensuite, nous exposerons les principes fondamentaux de l'imagerie par résonance magnétique de diffusion, y compris la diffusion des molécules d'eau dans le cerveau et les séquences d'IRM employées pour quantifier cette diffusion. En outre, nous détaillerons les modèles de diffusion employés pour décrire la diffusion à l'échelle locale, tels que les tenseurs de diffusion et la déconvolution sphérique contrainte, tout en explorant les techniques employées pour leur estimation.

La dernière partie de cette section sera consacrée à l'exposition des diverses méthodes de tractographie de la matière blanche, en particulier : Les méthodes déterministes locales, les méthodes probabilistes locales et les méthodes globales.

Nous décrirons les avantages, les inconvénients et les principales caractéristiques de chaque catégorie de méthode avant d'aborder les techniques de filtrage post-traitement nouvellement introduites. Enfin, nous présenterons les principaux défis rencontrés par les algorithmes de tractographie.

Distance de Wasserstein convolutive pour l'évaluation de la tractographie

La diversité des techniques disponibles pour reconstruire les faisceaux de fibres entraîne une variabilité importante entre les estimations, ce qui complique l'interprétation des résultats par les cliniciens et la comparaison des algorithmes de tractographie par les chercheurs. Des challenges tels que tractometer [Côté et al., 2013a] et ironTract [Maffei et al., 2020] s'attaquent à ce problème en étudiant les sources de variabilité et en établissant un cadre commun pour la comparaison. Bien que les évaluations visuelles donnent un aperçu rapide de la qualité des tractogrammes, elles ne permettent pas d'effectuer des comparaisons approfondies. Pour faciliter des comparaisons équitables, diverses mesures ont été mises au point, notamment le score de Dice, la corrélation de la densité et les mesures de plausibilité anatomique telles que la régularité topographique et les évaluations métriques de TractoMeter. Néanmoins, ces mesures sont basées sur des quantités distinctes extraites des tractogrammes et, par conséquent, elles peuvent évaluer différentes facettes de la qualité des tractogrammes.

Au chapitre 3, nous proposons tout d'abord une analyse comparative qui englobe à la fois des données synthétiques (simulant la translation, la rotation, la déformation et la dégradation de faisceaux de fibres) et des données issues d'un vrai scanner. Notre objectif est d'étudier les performances de plusieurs mesures d'évaluation de tractogrammes couramment employées, notamment le score de Dice, la corrélation de la densité, ainsi que le pourcentage de vraies connections et de vraies fibres. En plus de ces mesures, nous introduisons et évaluons une nouvelle mesure d'évaluation pour les tractogrammes, qui s'appuie sur les principes du transport optimal. Nous montrons l'intérêt de cette nouvelle mesure lorsqu'elle est intégrée à d'autres mesures d'évaluation. Nos résultats démontrent qu'en combinant ces diverses mesures, une comparaison plus approfondie et plus complète des tractogrammes devient possible, ce qui conduit à une évaluation plus complète.

Ce travail a été accepté et présenté à la 19ème édition de l'International Symposium on Biomedical Imaging (ISBI) en 2022

Un framework Riemannien pour l'incorporation d'a priori anatomiques issus de faisceaux de fibres de la substance blanche dans les algorithmes de tractographie basés sur l'ODF.

Malgré les avancées en matière d'acquisition de données en IRM de diffusion, de modélisation de la diffusion et d'estimation des faisceaux, la tractographie de la substance

blanche demeure confrontée à des limitations qui restreignent son utilité en contexte clinique. Les algorithmes recents parviennent à estimer une grande partie des faisceaux de matière blanche, mais ils rencontrent des obstacles en ce qui concerne l'ampleur spatiale et génèrent fréquemment des faisceaux non valides. Par exemple, les méthodes de tractographie locale visent à déduire une connectivité globale à partir d'informations directionnelles locales. En conséquence, ces algorithmes ont souvent tendance à privilégier le trajet le plus simple, même dans des zones complexes, comme des régions de croisement de fibres, engendrant ainsi des résultats parfois peu réalistes. Plusieurs études suggèrent que l'intégration de modèles de microstructure de diffusion avancés, l'application de techniques de filtration des fibres a posteriori, ou le recours à des méthodes de tractographie basées sur l'apprentissage automatique pourraient contribuer à éliminer ces fausses fibres.

Une stratégie alternative consiste à pallier le manque d'informations globales en intégrant des connaissances anatomiques préexistantes sur la structure du cerveau humain. Des approches récentes qui combinent des atlas anatomiques avec des techniques de tractographie déterministe ont montré des résultats prometteurs. D'autres méthodes introduisent des a priori relatifs à la diffusion lors du processus d'estimation des fibres, ce qui renforce la précision de la reconstruction des faisceaux de matière blanche. Par exemple, une méthode associe des informations anatomiques et des orientations préalables issues d'un atlas dans le but d'améliorer la reconstruction des fibres longues [Rheault et al., 2019].

Sur la base de ces résultats prometteurs, nous proposons dans le chapitre 4 une méthode de création et de combinaison d'a priori anatomiques qui peut être utilisée avec n'importe quel algorithme de tractographie basé sur les "orientation distribution function" (ODF). Notre approche utilise des faisceaux de fibres pré-segmentés pour agréger des informations globales provenant de plusieurs cerveaux, capturant la variabilité d'orientation dans des régions cérébrales complexes. Ces prédictions sont représentées sous la forme de "track orientation distribution" (TOD) et sont combinées avec les données ODF à l'aide d'une approche riemannienne. Ensuite, nous évaluons cette méthode avec deux algorithmes modernes, MRtrix iFOD2 et Trekker PTT, sur deux ensembles de données : 1/ Les données simulées DiSCo et 2/ les données réelles du Human Connectome Project (HCP). Nos résultats démontrent des améliorations dans la qualité du tractogramme, en particulier en ce qui concerne l'étendue spatiale ainse que la quantité de vraies fibres.

Un preprint de ce travail est disponible à https://hal.science/hal-04246380. De plus, il sera soumis courant octobre au journal Human Brain mapping (HBM).

Modifications de la microstructure de la matière blanche le long des fibres dans la dépression résistante

La dépression affecte environ 350 millions de personnes dans le monde et se classe parmi les maladies chroniques les plus invalidantes. Il est important de noter que seulement environ la moitié des patients réagissent favorablement à leur traitement initial, et les thérapies antidépressives standard ne conduisent à une rémission que dans 30 à 40% des cas Malheureusement, il n'existe actuellement pas de biomarqueurs fiables pour identifier les personnes à risque de TRD et guider les stratégies thérapeutiques. Certaines études de neuro-imagerie suggèrent que la TRD pourrait être associée à des anomalies microstructurelles spécifiques de la matière blanche, en particulier dans des régions telles que le cortex cingulaire sous-callosal (SCC) et le cortex préfrontal (PFC).

Dans le cinquième chapitre, nous proposons une analyse comparative entre deux groupes de patients atteints de dépression résistantes et non-résistantes, en fonction de l'amélioration de leur état 6 mois après le début de l'étude, en utilisant une approche tractométrique. Pour caractériser la microstructure de diffusion le long des faisceaux de fibres qui relient les régions impactées par la TRD, nous avons utilisé des métriques basées sur l'ODF. Pour améliorer notre analyse, nous avons effectué des évaluations statistiques conjointement avec une analyse en composantes principales. Cette méthode de réduction de données nous a permis de réduire la redondance entre les variables et d'affiner le pouvoir discriminant de notre analyse.

De plus, la méthode de création et de combinaison d'a priori anatomiques, développée dans le chapitre 4, est testée sur cet ensemble de données. Nous avons étudié l'influence et l'intérêt de l'ajout d'a priori anatomiques lors de la tractographie pour une cohorte de patients. Notre hypothèse sous-jacente était que l'amélioration de la qualité des tractogrammes, en particulier en termes d'extension spatiale et de nombre de vraies fibres, pourrait avoir un impact significatif sur cette étude, en termes d'interprétabilité des mesures de diffusion et de détection de différences potentielles entre les groupes.

Nos résultats révèlent deux points essentiels. Premièrement, l'incorporation d'a priori améliore l'estimation des fibres en éliminant les fibres erronées et en améliorant leur orientation. Cette amélioration a contribué à une décorrélation plus prononcée des mesures microstructurelles, les rendant plus sensibles et interprétables. Deuxièmement, chez les patients atteints de TRD, nous avons observé des diminution des mesures liées à la restriction et à la dispersion des fibres dans le Splenium du corps calleux, ce qui est cohérent avec des résultats antérieurs issus d'études portant sur la TRD.

Chapter 1

Introduction

1.1 Context

Magnetic resonance imaging (MRI) is a powerful, non-invasive technique that allows for a comprehensive exploration of the intricate structure, functional processes, and molecular makeup of brain tissues. The continual development of innovative MRI approaches has significantly enhanced our capacity to detect alterations within the brain closely linked to various diseases, advancing our understanding at a rapid pace.

Among these techniques, diffusion MRI allows to measure the thermal agitation of the water molecule in the brain [E. Stejskal and Tanner, 1965]. This agitation being constrained by the tissues micro-structures, typically the nervous system axons, dMRI enables the voxelwise estimation of the orientations of the white matter fibers [Dell'Acqua and Tournier, 2017; D. Jones, 2010]. Additionally, diffusion MRI, combined with tractography techniques, allows us to estimate the pathways of nerve fibers in the brain. By selecting seed points within the brain's white matter and following local fiber orientations voxel by voxel, we can map out brain connectivity and understand the physical connections that facilitate information exchange between cortical regions [D. Jones, 2010]. This process is known as fiber tracking or fiber tractography, and the resulting collection of white matter pathways is referred to as tractograms [Mori and Van Zijl, 2002]. These approaches have the remarkable capability to delineate white matter fiber pathways, offering unprecedented insights into the structural connections within the human brain. They hold enormous potential for studying brain anatomy, development, and function [Jeurissen et al., 2019a]. Furthermore, tractography has demonstrated its substantial worth in the field of neurosurgery, playing a pivotal role in surgical planning, particularly in the preservation of critical white matter pathways during brain resections [Mancini et al., 2019]. In addition to this, diffusion studies have spurred significant progress in the exploration of psychiatric conditions like depression [Coloigner et al., 2019].

Despite advancements in dMRI acquisition and tracking methods, white matter fiber

tractography continues to grapple with certain limitations. Recent studies reported the existence of a significant number of connections that remain undetected by tractography, resulting in false negatives [D. B. Aydogan et al., 2018]. This issue poses a critical challenge, particularly in applications like surgical planning. Furthermore, the outcomes of other studies indicate that state-of-the-art tractography algorithms produce substantial numbers of false positives as well [K. Maier-Hein et al., 2017b]. This drawback hampers the accurate exploration of network properties within the brain's connectome [Zalesky et al., 2016].

1.2 Organization of the manuscript

State of the art

The initial section of this manuscript is dedicated to provide a comprehensive overview of the current state of the art, where we will return to the fundamental concepts that serve as the foundation for the subsequent sections of this work.

First, we will provide a concise summary of the structural organization of the human brain. We will, then, introduce the fundamental principles underlying diffusion MRI, including the diffusion of water molecules within the brain and the MRI sequences employed for measuring this diffusion. Afterward, we will describe the diffusion models used to locally describe the diffusion, such as diffusion tensors and multi-tissue constrained spherical deconvolution, while also delving into the methods utilized for their estimation.

The last part of this section is devoted to explain the different methods of white matter tractography, specifically:

— The local deterministic methods
— The local probabilistic methods
— The global methods

We will outline the benefits, drawbacks, and principal features of each method category before delving into the newly introduced post-processing filtering techniques. Finally, we will present the primary challenges encountered by tractography algorithms.

A convolutional Wasserstein distance for tractography evaluation

The multitude of available techniques for reconstructing fiber bundles leads to significant variability, making it challenging for clinicians to interpret results and for researchers

to compare tractography algorithms. Challenges like tractometer [Côté et al., 2013a] and ironTract [Maffei et al., 2020] address this by investigating variability sources and establishing a common framework for comparison. While visual evaluations offer quick insights into tractogram quality, they do not allow for an in-depth comparisons. To facilitate fair comparisons, various measures have been developed, including the Dice score, density correlation, and anatomical plausibility metrics like topographic regularity and TractoMeter's metric evaluations. Nevertheless, these metrics are based on distinct quantities extracted from the tractograms, and as a result, they may assess different facets of tractogram quality.

In Chapter 3, we first propose a comprehensive analysis that encompasses both synthetic data (involving translation, rotation, deformation, and degradation) and real-world scenarios. Our aim is to investigate the performance of several commonly employed tractogram evaluation metrics, including the Dice score, density correlation, as well as the percentage of valid connections and valid streamlines. In addition to these established metrics, we introduce and evaluate a novel evaluation measure for tractograms, which leverages optimal transport principles. This novel metric proves its worth when integrated with other evaluation measures. Our findings demonstrate that by combining these diverse metrics, a more profound and comprehensive comparison of tractograms becomes possible, leading to a more comprehensive evaluation.

This work was accepted and presented in the 2022 19th International Symposium on Biomedical Imaging (ISBI)

A Riemannian framework for incorporating white matter bundle priors in ODF-based tractography algorithms.

Despite advancements in diffusion MRI acquisition, modeling, and tracking, white matter fiber tractography still faces limitations that hinder its clinical applicability. Modern algorithms can recover a significant portion of white matter bundles but struggle with spatial extent and often also produce invalid bundles. For example, local tractography methods aim to recover a global connectivity by inferring from local directional information. This often results in the algorithm favoring the simplest path available, even in complex regions, occasionally leading to unrealistic decisions. Various studies suggest that advanced diffusion microstructure modeling, streamline filtering techniques, or machine-learning-driven tractography could help to remove these false fibers.

An alternative approach involves compensating for the lack of global information by

incorporating anatomical priors. Recent methods combine anatomical atlases with deterministic tractography and have shown encouraging outcomes. Additional techniques introduce diffusion priors during tracking, improving white matter bundle delineation. For instance, one method combines anatomical and orientational priors based on a template to enhance the reconstruction of long fibers [Rheault et al., 2019].

Based on these promising results we propose in Chapter 4 a method for creating and combining anatomical priors that can be used with any tractography algorithm based on orientation distribution function (ODF). Our approach utilizes pre-segmented fiber bundles to aggregate global information from multiple brains, capturing orientational variability in complex brain regions. These priors are represented as track orientation distribution objects and are combined with ODF data using a Riemannian framework. We then evaluate this method whith two state-of-the-art algorithms MRtrix iFOD2 and Trekker PTT on two dataset: 1/the DiSCo dataset and 2/ the Human Connectome Project (HCP) data. Our result demonstrate improvements in tractogram quality, particularly in terms of spatial extent.

A preprint of this work is available at https://hal.science/hal-04246380. In addition, it will be submitted in the coming weeks to the journal Human Brain mapping (HBM).

White matter microstructure changes along the fiber in treatment resistant depression

Mood Depressive Disorder (MDD) affects 350 million individuals across the globe and stands as one of the most incapacitating chronic illnesses. Its recurrent nature and resistance to conventional treatments make it a significant contributor to global disability. It's noteworthy that merely 50% of patients experience a positive response to their initial treatment, and standard antidepressant therapies achieve remission in only 30-40% of cases. Additionally, around 25% of individuals diagnosed with MDD, and who have undergone treatments for it, develop what is known as treatment-resistant depression (TRD). This means they do not respond to the typical and first-line therapeutic options. Reliable biomarkers to identify individuals at risk of TRD and guide therapeutic strategies are lacking. Some neuroimaging studies suggest that TRD may be linked to specific microstructural white matter abnormalities, particularly in regions like the sub-callosal cingulate cortex (SCC) and the prefrontal cortex (PFC).

In chapter 5, we therefore propose to analyse group differences between 2 groups of depressed patients – responders / non-responders – based on illness improvement at 6-

month follow-up, using a tractometry approach. We employed metrics based on ODF to characterize the diffusion microstructure along fiber bundles connecting regions affected by pathology in TRD. To enhance our analysis, we conducted statistical assessments coupled with a principal component analysis. This reduction analysis allows us to mitigate redundancy among sensitivities and refine the discriminative power of our analysis.

In addition, the method for creating and combining anatomical priors, developed in chapter 4 is tested on this dataset. We studied the influence and the interest of adding anatomical priors during the tractography for a patient cohort. We hypothesized that the improvement in tractogram quality, particularly in terms of spatial extent could greatly enhance this study, in terms of interpretability and potential group differences.

Our findings reveal two key points. Firstly, the incorporation of priors improved fiber estimation by eliminating erroneous fibers and enhancing their orientation. This enhancement contributed to a more pronounced decorrelation of microstructural metrics, making them more sensitive and interpretable. Secondly, among TRD patients, we observed reduced measures of restriction and dispersion in the Splenium of the corpus callosum, aligning with prior findings in TRD.

An article on this work is in preparation

Chapter 2

State of the art

2.1 Introduction

The human brain is an intricately structured and highly interconnected network of specialized nerve cells known as neurons. These neurons possess distinct components, including cell bodies housing the nucleus, dendrites responsible for receiving electrochemical signals, and axons that transmit these signals to other neurons. The brain can be conceptually divided into three major components: grey matter (GM), white matter (WM), and cerebrospinal fluid, each serving vital roles in neural functioning [Finger, 1994].

Grey matter, comprising neuronal cell bodies, plays a crucial role in processing information and is notably prominent in the cortex, which is responsible for higher-order cognitive functions. In contrast, WM primarily consists of long-range neuronal branches called axons, which serve as the neural highways connecting different regions of the brain. These axonal connections enable the transmission of signals over extended distances, facilitating communication and coordination among various brain regions.

The Figure 2.1 provides a schematic illustration of the brain organisation and a neuron anatomy. Neurons employ two distinct methods for transmitting electrical signals to communicate with each other. Dendrites enable communication with neighboring neurons and axons that terminate nearby, while axons are responsible for connecting various groups of neurons across long distances.

In this thesis, we will focus on WM, which is mainly composed of axons, whose length can vary from a few micrometers to several centimeters, and even over a meter in the human central nervous system. The diameters varie from $0,1\mu m$ to $20\mu m$ for the larger ones. Axons are generally grouped into large bundles fascicles that enable communication between different distant brain regions. For a long time, analysis of the brain was only possible through intrusive and post-mortem examinations. Yet understanding, and therefore initially being able to correctly represent and vsualize the way in which different brain regions communicate with each other is a key step, both for progress in diagnosing many

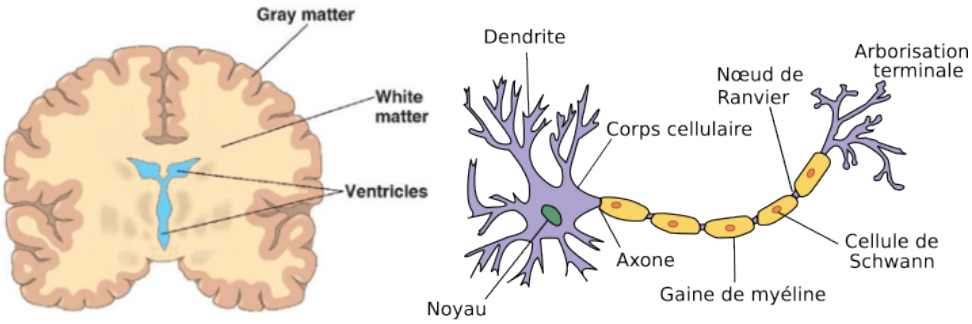

Figure 2.1 – On the left: Illustration of a coronal slice, showing the GM and the WM (from http://elearningbiology.weebly.com). On the right: Simple illustration of a neuron (from https://fr.wikipedia.org/wiki/Neuromorphologie).

neurodegenerative diseases, and contribute to advancing our knowledge of the organization and functioning of the human brain. Thus, the remainder of this chapter describes two key methods for studying brain connectivity: diffusion MRI and tractography.

2.2 Diffusion magnetic resonance imaging

2.2.1 Water diffusion in the brain

Diffusion characterizes the migration of molecules from the highest to the lowest concentration within a liquid, solid or gas solution.

At the macroscopic scale, in a liquid, the diffusion flux J can be modeled by the Fick's firt law [Fick, 1855]:

$$J = -D\nabla C \tag{2.1}$$

where J (mol/m^{2}s) is the diffusion flux, D (mol/m^3) is the chemical species concentration and ∇C (m^2/s) is the concentration gradient.

At the microscopic scale, this migration of molecules is due to the thermal agitation. When a homogeneous concentration is reached, the diffusion flux in a liquid become null. However, the motion of molecules still persists. Thermal agitation, or Brownian motion, first observed by the botanist Robert Brown in 1828 [Brown, 1828], is a phenomenon that describes the random movement of microscopic particles suspended in a fluid. This erratic motion arises from the constant collisions between the particles and the fluid molecules, causing them to move in seemingly unpredictable directions, giving rise to a characteristic

"random walk" pattern. While, due to the random nature of this motion, the trajectory of an unique molecule is difficult to estimate, the prediction of the behavior of a large number of molecule is possible using a probabilistic framework. In 1905, Einstein proposed the concept of the "displacement distribution" or "diffusion probability density function," denoted as $p(r)$. This function quantifies the proportion of particles that are expected to experience a displacement of r within a specific "diffusion time" t. Alternatively, it represents the probability that an individual particle will undergo such a displacement during that time. Einstein demonstrated that when the number of particles is abundant, and they are allowed to freely diffuse in all directions, $p(r)$ follows a Gaussian distribution [Einstein, 1905]:

$$p(r) = \frac{1}{\sqrt{(4\pi\Delta_t D)^3}} exp(-\frac{||r^2||}{4\Delta_t D}) \tag{2.2}$$

where D is is the diffusion coefficient from equation 2.1, Δ_t the diffusion time and r the displacement vector. An interesting feature of this equation is that the isoprobabilily surface of p take the form of a sphere, meaning that if the molecules are unconstrained, the diffusion is isotropic, i.e. there is a equal probability of displacing, regardless of the direction observed. From this probabilistic model, Einstein also proposed a relationship between the mean-squared displacement, $\langle||r||^2\rangle$, and the diffusion coefficient D:

$$\langle||r||^2\rangle = 6D\Delta_t \tag{2.3}$$

where Δ_t is the diffusion time.

Knowing that approximately 75% of the brain's composition consists of water [Kreis et al., 1993; Lentner, 1981], measuring the mean squared displacement of water molecules provides powerful information about brain's tissues and structures. The diffusion of water molecules is constrained by brain's structure, such as tumors or axons within the white matter . For example, the average squared displacement per unit time will be higher in the direction of the axon than perpendicular to the axon. This measure is referred to as the apparent diffusion coefficient (ADC) [Bihan et al., 1986]. This characteristic of diffusion, crucial in diffusion MRI, enables us to obtain valuable insights into the microstructural properties of biological tissue.

2.2.2 Diffusion-weighted magnetic resonance imaging acquisition techniques

Basic principle of MRI

The MRI scanner produces a robust static magnetic field, usually ranging from 1 to 7 Teslas. Hydrogen nuclei possess magnetic dipoles known as spins, which align themselves proportionally with the strength of the magnetic field B_0. An initial Spin-echo sequence [Hahn, 1950] begins by exciting hydrogen nuclei with a 90° radiofrequency (RF) pulse, causing their magnetization vector to lean towards a plane perpendicular to the main magnetic field B_0. The hydrogen nuclei then undergo precession around the magnetic field, a phenomenon known as Larmor precession (see Figure 2.3 for an illustration of this phenomenon) [Bloch et al., 1946; Purcell et al., 1946]. The Larmor equation establishes a direct relationship between the precession frequency ω (rad/s) of spins in a magnetic field and the strength B_0 of the main magnetic field (T).

$$\omega = \gamma B_0 \tag{2.4}$$

Where γ is the gyromagnetic ratio, a constant nuclei specific.

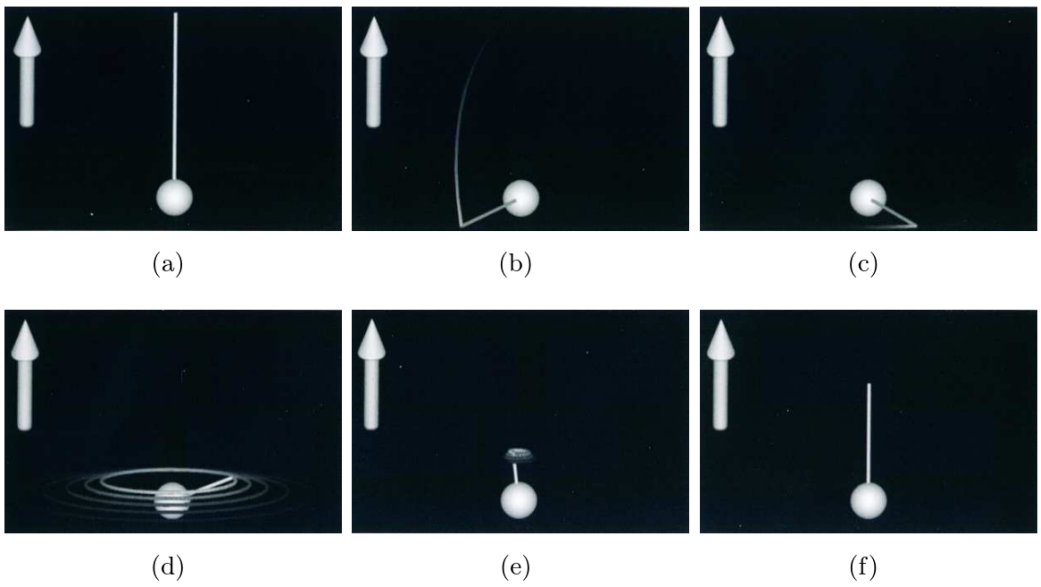

Figure 2.2 – Illustration of spin dephasing. The spin are initially in sync (a), they quickly begin to dephase due to magnetic field variations (b,c,d), followed by a relaxation causing the signal to decay (e) and finally return to sync (f). From [Johansen-Berg and Rushworth, 2009]

The precessing magnetic fields of the spins induce a voltage in the receiver coil. Initially, the spins are synchronized, but they quickly begin to dephase due to magnetic field variations and dipolar interactions, causing the induced signal to decay. The illustration of this process can be seen in Figure 2.3. This dephasing can be reversed by applying a subsequent 180° reversed RF pulse, refocusing the signal into an echo. In this spin-echo sequence, the time between the first RF pulse and the echo is referred to as TE, and it is twice the duration between the two RF pulses. The resulting echo is captured by a receiver coil, and from this raw data MR images are reconstructed.

As previously stated, the Larmor frequency is influenced by the strength of the magnetic field. Since the MRI scanner maintains a constant magnetic field B_0, all hydrogen nuclei are excited simultaneously. Therefore, it is impossible to accurately reconstruct a spatial map of the signal's origin from the received signal by the coils. To address this, a linear magnetic field, known as a gradient, is applied to select a specific area that will be exclusively excited by a particular RF pulse. The overall magnetic field of the scanner is then expressed as follows:

$$B(t) = G_0 + xG_x(t) + yG_y(t) + zG_z(t) \tag{2.5}$$

where $G_x(t)$, $G_y(t)$ and $G_z(t)$ are the gradients applied in the three direction (x, y and z). The gradient G_z is used to select a 2D plan in which G_x and G_y are employed to image a specific point within this plane.

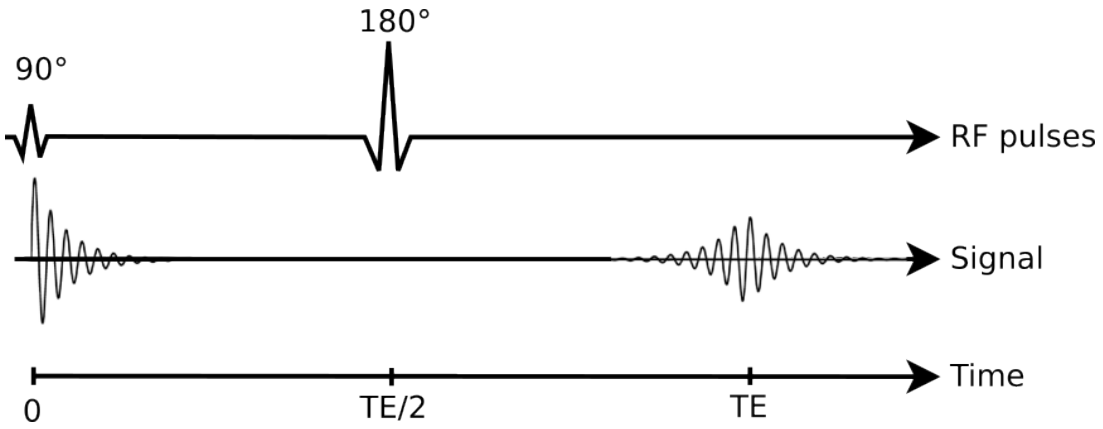

Figure 2.3 – The spin echo sequence: The first RF pulse at $t = 0$ cause the spins to be dephased between $t = 0$ and $t = TE/2$. The application of the second, 180°, RF pulse rephase the spins up to TE. The signal echo is then captured by a receiver coil, and from this raw data MR images are reconstructed.

Pulsed Gradient Spin-echo (PGSE)

By incorporating two linear dephasing gradients, symmetrically placed around the 180° refocusing RF pulse, the spin echo sequence can be made sensitive to diffusion along a specific orientation [E. O. Stejskal and Tanner, 1965], as displayed in the Figure 2.4. These linear diffusion-encoding gradients, $G_x(t)$, are two rectangular diffusion gradient pulses functions along the x-direction, with duration δ and with time delay Δ between the two pulses. The initial dephasing gradient pulse causes a phase shift ϕ_1 in the spin's transverse magnetization, which varies depending on its position:

$$\phi_1 = \gamma \int_0^{\delta} G_x(t)x(t)dt = \gamma\delta g_x x_1 \tag{2.6}$$

where ϕ_1 is the spin phase shift after the application of the dephasing gradient, γ the gyromagnetic ratio for hydrogen nuclei, $x(t)$ is the position of the spin a time t and $G_x(t)$ is the pulsed gradient along the direction x. The spin position x_1 is constant during δ and

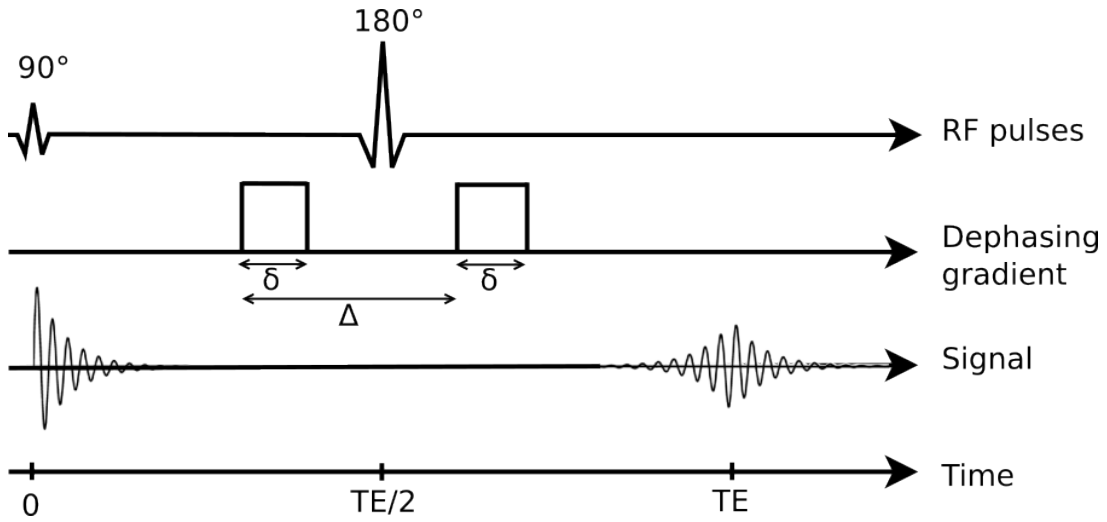

Figure 2.4 – The Pulsed Gradient Spin-echo sequence: The initial gradient pulse, of length δ and known as the dephasing pulse, introduces a spin phase shift. When dealing with stationary spins, this phase shift is nullified through the application of a subsequent gradient pulse called the rephasing pulse. Spins that undergo motion within the time interval Δ will encounter a phase shift that is directly proportional to the distance they have traveled, leading to a reduction in signal intensity. This signal loss is captured by the receiver coil and is a measure of the diffusion along the gradients direction.

The amount of dephasing is directly related to both the duration δ and the strength g_x of the gradient. Likewise, the second rephasing gradient pulse causes a phase shift ϕ_2 and is given by:

$$\phi_2 = \gamma \int_{\Delta}^{\Delta+\delta} G_x(t)x(t)dt = -\gamma\delta g_x x_2 \tag{2.7}$$

where ϕ_2 is the spin phase shift after the application of the rephasing gradient and x_2 is the position of the spin when the gradient is applied.

By applying the 180° RF pulse between both gradients, the phase change that occurred before it is reversed. In the case of static spins, where there is no diffusion along the gradient direction ($x_1 = x_2$), the resulting phase shift ϕ will be zero. Conversely, in the case of diffusion along the the gradient direction during the period between the two gradient applications, Δ, the spins will experience a net phase shift, depending on the distance $(x_2 - x_1)$. After the two RF pulses, the spins are not completely refocused, the amplitude of the PGSE signal S is then given by:

$$S = S_0\langle e^{i\phi}\rangle \leq S_0 \tag{2.8}$$

where $\phi = \phi_2 - \phi_1$ is the resulting phase shift, $\langle ...\rangle$ is the average over the spin population and S_0 represents the signal intensity when no diffusion-encoding gradient is applied. Note that the acquisition of S_0 over the all volume produces an image called b_0. On the opposite, when $S \neq S_0$, the diffusion weighting factor, known as the b-value, is defined as [Bihan et al., 1986]:

$$b = \gamma^2 G^2 \delta^2 (\Delta - \frac{\delta}{3}) \tag{2.9}$$

where G is the gradient amplitude, δ is the gradient application time and Δ is the sum of gradient.

Because the displacement distribution of diffusing spins follows a random pattern caused by Brownian motion, the phase distribution of the spins also becomes random. Consequently, this leads to a reduction in the amplitude of the signal when averaged across the the spin population. The signal attenuation is given by:

$$A(q) = \frac{S(q)}{S_0} \tag{2.10}$$

$$A(q) = e^{-bD} \tag{2.11}$$

where $S(q)$ is a signal acquired with an unit gradient g and D the ADC in this direction.

The equation 2.11 gives a direct relation between the diffusion coefficient, D, and the signal attenuation for an unique gradient direction, $A(q)$. Although this is enough to characterize the diffusion in isotropic diffusion areas (i.e. diffusion homogeneous in all direction), this is not sufficient to describe anisotropic situations where the diffusion coefficient differs according to the direction observed. As described in [E. O. Stejskal and Tanner, 1965], the signal attenuation $A(q)$ can also be expressed as the 3D Fourier transform $\mathcal{F}$ of the diffusion probability density function $p(r)$:

$$A(q) = \int_{R^3} p(r) exp(-iq^T r) dr = \mathcal{F}[p(r)] \tag{2.12}$$

where $q = \gamma \delta g$ is the q-vector and g is the applied diffusion gradient vector.

The q-space in then defined as the ensemble of all possible q-vectors. The simplest method for estimating the diffusion probability density function (PDF) is then to sample the q-space on an evenly distributed sphere and performing an inverse 3D Fourier transform. This method is called the q-space imaging [Callaghan et al., 1988].

Another technique for characterizing the local diffusion characteristics involves estimating a tensor from a collection of multiple 3D ADC images acquired with gradients in various directions. In this approach, the principal eigenvector of the tensor provides the primary local diffusion direction. This method is known as diffusion tensor imaging, and will be described in the following section.

2.3 Diffusion tensor imaging (DTI)

2.3.1 Tensor estimation and description

As explained in the previous section, estimating the ADC from the weighted attenuated signal gives us insight on isotropic diffusion situation or for a an unique diffusion direction. However, in brain regions where diffusion is constrained by the microstructure, typically the water molecule in the axons, several measures in different directions are needed to describe the situation. Thus, the generalization of the ADC model, the diffusion tensor, estimated from a set of multiple diffusion weighted images (DWI), allows to represent the diffusion in any directions images [P. J. Basser et al., 1994a; P. J. Basser et al., 1994b]. This model represent, in each voxel, the PDF $p(r)$ in the form of a 3D gaussian tensor, defined by a 3×3 symmetric positive-definite matrix:

$$D = \begin{pmatrix} D_{xx} & D_{xy} & D_{xz} \\ D_{yx} & D_{yy} & D_{yz} \\ D_{zx} & D_{zy} & D_{zz} \end{pmatrix} \tag{2.13}$$

This model requires at least 7 images (6 DWI and 1 b_0) to be estimated. Each DWI is represented by its b-value and its gradients directions components $g = (g_x, g_y, g_z)$ The equation 2.11 then becomes:

$$A(q) = e^{-B^T DB} \tag{2.14}$$

with $B = \sqrt{b_0}g$. A simple and fast method to analytically calculate D is is to perform a linear least square estimation on the logarithm of $A(q)$ [Koay et al., 2006]. Other solutions exist, as in [Chang et al., 2005], where the tensor is estimated through an iterative least square regression in order to remove the outlier.

Interpreting the tensor involves an analysis of its eigenvectors and eigenvalues. As the tensor is a symmetrical matrix with real coefficients, it enables its diagonalization in an orthonormal basis. Subsequently, the main diffusion direction corresponds to the eigenvector linked to the largest eigenvalue

$$D = R^T PR \tag{2.15}$$

with $R = \begin{pmatrix} v_1 & v_2 & v_3 \end{pmatrix}$ and $P = \begin{pmatrix} \lambda_1 & 0 & 0 \\ 0 & \lambda_2 & 0 \\ 0 & 0 & \lambda_3 \end{pmatrix}$ respectively the matrix of eigenvectors and eigenvalues [Hasan et al., 2001]. The three eigenvalues λ_i corresponds to the diffusion coefficients along the three axes of the tensor. The Figure 2.5 show a visual comparison between two anisotropic and isotropic diffusion tensor. Using the 3 eigenvalues of the tensor, various scalar measures are computed to characterize the diffusion process.

— The largest eigenvalue, λ_1, denotes the diffusivity in the principal direction of D and is called the axial diffusivity (AD).
— The mean of the two other eigenvalues, λ_2, λ_3, is the radial diffusivity (RD) and gives information about the diffusion perpendicular to the main direction.

$$RD = \frac{\lambda_1 + \lambda_2}{2} \tag{2.16}$$

— The mean diffusivity (MD) is the average of the diffusion in all directions:

$$MD = \frac{\lambda_1 + \lambda_2 + \lambda_3}{3} \tag{2.17}$$

— The fractional anisotropy (FA) quantifies the fraction of diffusion that is anisotropic, such as: [P. J. Basser and Pierpaoli, 1996]:

$$FA = \sqrt{\frac{3((\lambda_1 - \hat{\lambda})^2 + (\lambda_2 - \hat{\lambda})^2 + (\lambda_3 - \hat{\lambda})^2}{2(\lambda_1^2 + \lambda_2^2 + \lambda_3^2)}} \tag{2.18}$$

This metric spans from 0 to 1, with 0 denoting an isotropic tensor (a sphere) and 1 indicating a fully anisotropic tensor, when diffusion occurs in one unique direction.

The MD metric is the first biomarker observed in clinical context, as it allows to detect various pathology, such as edema, ischemic strokes [Lythgoe et al., 1997] and cystic metastatic tumors [Toh et al., 2011]. AD and RD are both used to characterize the general condition of axons. AD has been shown to be significantly correlated with axonal integrity [Tu et al., 2016], whereas in other studies, RD is strongly associated with electrophysiological markers of demyelination. [Kronlage et al., 2017]. FA is highly sensitive to microstructural changes, but not very specific to the type of changes. This DTI-derived metric is a marker of so-called white matter integrity and finds extensive utilization in numerous clinical studies [Beaulieu, 2002; Assaf and Pasternak, 2007; H. Zhang et al., 2012b].

Despite being the simplest diffusion model, the tensor is widely used both in clinical and research contexts for a variety of reasons. First, it offers a direct visual interpretation of the diffusion configuration of the studied regions, both locally, by shape, and globally, by direction or color (see Figure 2.6). Next, it provides simple tissue microstructure parameters. Finally, its estimation is fast, simple and robust. However, this model suffers from several major limitations.

2.3.2 Limitations of the DTI

The size of the dMRI voxel is typically 1.5 to $3mm^3$ in clinical DTI, which contains multiple bundles of axons, myelin sheaths, astrocytes, and extracellular spaces. However, since only one tensor is fitted for each voxel, all directional information will be averaged in the tensor parameters. And in complex areas, the DTI model can not estimate fibers

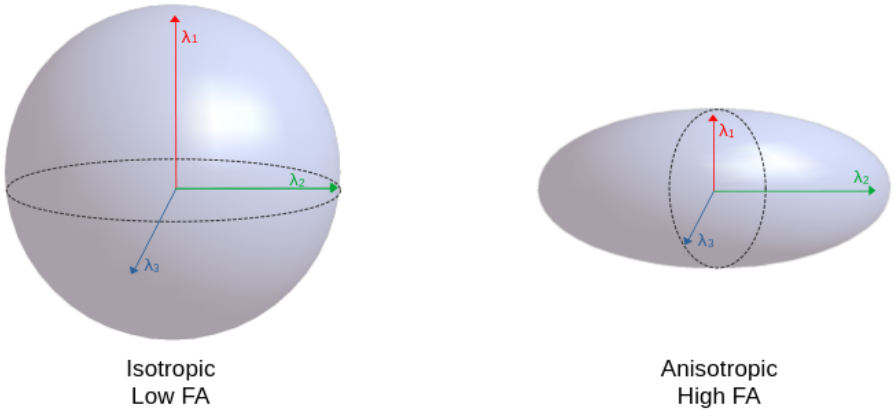

Figure 2.5 – Diffusion tensor for isotropic and anisotropic diffusion. See how, for the isotropic diffusion tensor, no main diffusion direction can be extracted.

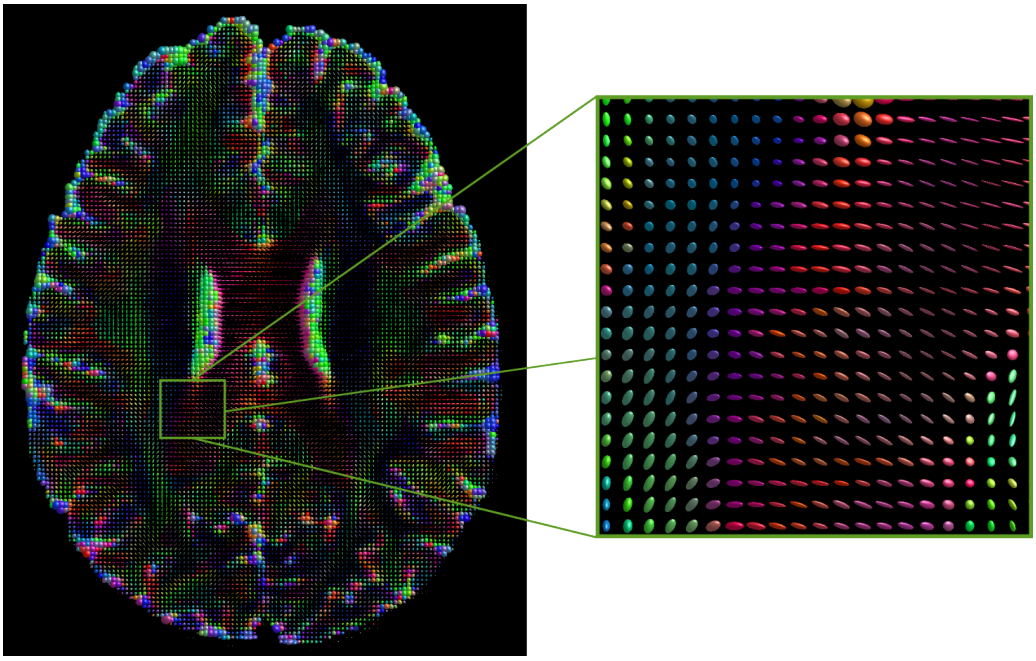

Figure 2.6 – Diffusion tensor map. Note how the shape of the DT offers a direct interpretation of the local diffusion. Its color and orientation can quickly reveal the presence and direction of a fiber bundle. However, this model is unable to tell us whether a spherical tensor refers to a free-water area or a complex fibers structure.

with different orientation. Tensors correctly represent the structure when all fibers have the same orientation but in the crossing areas the tensor is represented as isotropic in the plane of the crossing fibers, as displayed in the Figure 2.7 [A. L. Alexander et al., 2001; D. S. Tuch et al., 2002]. Hence, DTI cannot distinguish free water area and multi-orientation structure.

Nonetheless, the interpretation of changes in the measured diffusion tensor is complex and should be performed with care. For example, in clinical research, FA is frequently interpreted as a measure of "white matter integrity." However, it's important to note that several factors, including cell death, alterations in myelination, shifts in extracellular or intracellular water content, among others, can lead to changes in FA [O'Donnell and Westin, 2011].

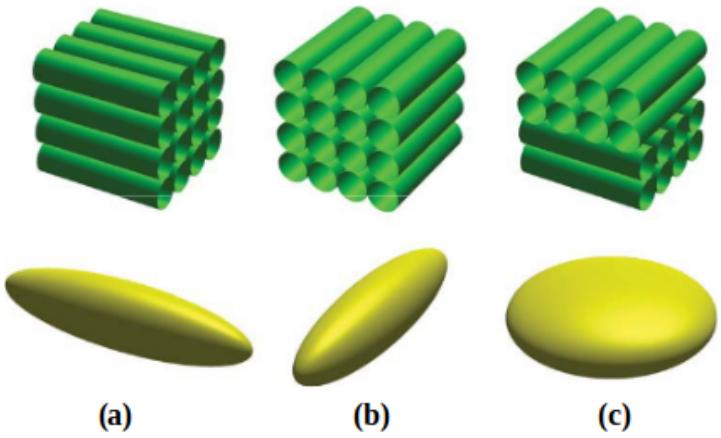

Figure 2.7 – Different fibers structure and their corresponding tensor. In (a) and (b) the principal orientation of the tensor correctly fit the direction of the fibers. In (c), the tensor is isotropic in the crossing plan and is thus unable to represent the two fibers directions. From [D. K. Jones, 2010

To overcome these limitations, more complex models capable of representing multiple orientations within a voxel were subsequently developed. The following section presents these models, their estimates and their applications.

2.4 Multi-fiber models

Most of the multi-fiber models examined in this section are based on orthogonal bases, which enable them to efficiently capture a large amount of signal information with just

a few coefficients. Some examples of such bases are the Fourier space [Bracewell et al., 1986], wavelets [Mallat, 1989] or the curvelet [Starck et al., 2003].

2.4.1 Spherical harmonics

In this manuscript, we will focus on the spherical harmonics (SH) basis, defined as:

$$Y_l^m(\theta,\phi) = \sqrt{\frac{(2l+1)}{4\pi}\frac{(l-m)!}{(l+m)!}}P_l^m(\cos\theta)e^{im\theta} \tag{2.19}$$

where $l = 0, 1, 2, ...$ and $m = -l, ..., 0, ..., l$ are the order and the degree of the SH, respectively; (θ, ϕ) are the spherical coordinates with $\theta \in [0, \pi]$ and $\phi \in [0, 2\pi]$; and P_l^m is the associated Legendre polynomial. The real parts of the SH basis function up to order $l = 3$ are displayed in the Figure 2.8. It can be shown [Courant and Hilbert, 1953] that any function of the unit sphere $f(\theta, \phi)$ can be expressed with a series of SH:

$$f(\theta,\phi) = \sum_{l=0}^{\inf}\sum_{m=-l}^{l} c_l^m Y_l^m(\theta,\phi) \tag{2.20}$$

with c_l^m, the SH basis coefficients.

Descoteaux et al. proposed a modified SH basis [Descoteaux et al., 2007c], which is designed to be antipodally symmetric, real and orthonormal. This modified basis is defined as:

$$Y_j^{'}(\theta,\phi) = \begin{cases} \sqrt{2}Re[Y_l^m(\theta,\phi)] & \text{if } m < 0 \\ Y_l^m(\theta,\phi) & \text{if } m = 0 \\ \sqrt{2}Im[Y_l^{-m}(\theta,\phi)] & \text{if } m > 0 \end{cases} \tag{2.21}$$

where j is an index: $j(l, m) = l^2 + l + 1 + m$.

In [Descoteaux et al., 2007c], authors showed that any real and antipodaly symmetric spherical function can be approximated with a truncated SH series:

$$f(\theta,\phi) = \sum_{l=0}^{l_{max}}\sum_{m=-l}^{l} c_j Y_j^{'}(\theta,\phi) \tag{2.22}$$

where j is an index: $j(l, m) = l^2 + l + 1 + m$.

Only the even degree coefficients are used, thus the number of coefficients needed to describe the functions is $N = \frac{(l_{max}+1)(l_{max}+2)}{2}$.

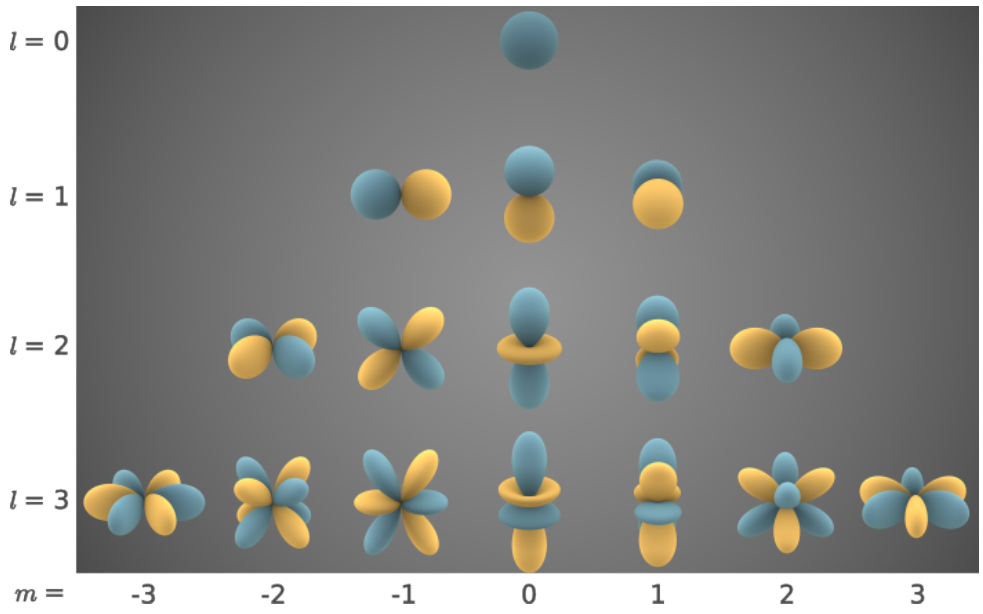

Figure 2.8 – Real part of the spherical harmonic basis up the order $l = 3$. The function value is visualized as the distance from the origin to the surface. Blue indicates positive function values. Yellow indicates negative function values. From https://en.wikipedia.org/wiki/Spherical_harmonics.

The previous equation can be rewrited as:

$$f = Yc \tag{2.23}$$

with f is a vector containing samples of $f(\theta, \phi)$ on the sphere, Y is a $(N \times N)$ matrix containing the modified SH basis and c the vector of SH coefficient. One can thus retrieves the coefficient c by performing an least squares minimization method, such as:

$$\hat{c} = (Y^T Y)^{-1} Y^T f \tag{2.24}$$

2.4.2 Q-Ball imaging

The Q-Ball imaging method [D. S. Tuch, 2004] aims to recover the orientation distribution function (ODF) from a collection of DWI acquisitions. The ODF is a function defined on the sphere, that gives the probability of diffusion in a given direction. Given this property, in [D. S. Tuch, 2004], authors have shown that, for a sufficiently high b-value, the ODF ψ can be reconstruct from the FRT of the diffusion signal. Given a function on a sphere $f(\omega)$, where ω is a unit direction vector and u is a vector perpendicular to w,

the FRT $\mathcal{E}$, evaluated at radius r is given by:

$$\begin{aligned}\mathcal{E}[f(w)](u,r) &= \int f(w)dw \\ &= \int f(w)\delta(x^T u)\delta(|w|-r)dw\end{aligned} \tag{2.25}$$

where δ is the Dirac delta function.

The ODF is then given by the equation [D. S. Tuch et al., 2003]:

$$\psi(w) = \mathcal{E}[S(q)](q^{'}) = 2\pi q^{'} \int P(r,\theta,z)J_0(2\pi q^{'} r)rdrd\theta dz \tag{2.26}$$

where $S(q)$ is the diffusion signal, $P(r,\theta,z)$ is the PDF in cylindrical coordinate, $q^{'}$ is the radius of the sampling shell, J_0 the Bessel function at the order zero, and q the diffusion wavevector defined as:

$$q = (2\pi)^{-1}\gamma\delta g \tag{2.27}$$

where γ is the gyromagnetic ratio for the nucleus of interest, δ is the diffusion gradient duration, and g is the diffusion gradient vector.

The ODF being a continuous function on the sphere, this method allows to represent several fibers orientations within a voxel, contrary to the DTI, but this method requires more DWI acquisitions. The Figure 2.9 gives an overview of the Q-ball algorithm. In addition, one the main limitations of the QBI is its computation time, which increase with the number of DWI.

To overcome this, in [Descoteaux et al., 2007c], Descoteaux et al. proposed to use a discrete equivalent of the FRT, the Funk-Hecke transform. In this version, the diffusion PDF is modeled with a SH basis as previously described. Fiven the equations 2.22 and 2.25, the ODF can be represented by:

$$\psi(w) = \sum_{l=0}^{l_{max}} \sum_{m=-l}^{l} c_l^m \int Y_j^{'}(q)dq \tag{2.28}$$

In addition, the Funk-Hecke theorem gives:

$$\int Y_j^{'}(q)dq = 2\pi P_l(0)Y_j^{'}(w) \tag{2.29}$$

Therefore, the ODF can be directly calculated using the spherical harmonics repre-

sentation of the diffusion signal:

$$\psi(w) = \sum_{l=0}^{l_{max}} \sum_{m=-l}^{l} c_l^m 2\pi P_l(0) Y_j^{'}(w) \tag{2.30}$$

From this equation, the ODF SH coefficients can be calculated through a simple matrix multiplication:

$$C = P.S \tag{2.31}$$

where C is the SH coefficients vector of size $(R \times 1)$, S is the $(N \times 1)$ diffusion weighted signal vector and P is the diagonal $(R \times R)$ FRT matrix with $P_{ii} = 2\pi P_l(0)$, $R = \frac{(l_{max}+1)(l_{max}+2)}{2}$ the SH basis order and N the numbers of DWI. Therefore, compared with the original FRT counterpart, this analytical QBI method offers both faster and simpler estimation and a more efficient data storage However, QBI is commonly conducted using intermediate b-value shell, this has the effect of blurring the ODF image, reducing the angular resolution [J.-D. Tournier et al., 2008].

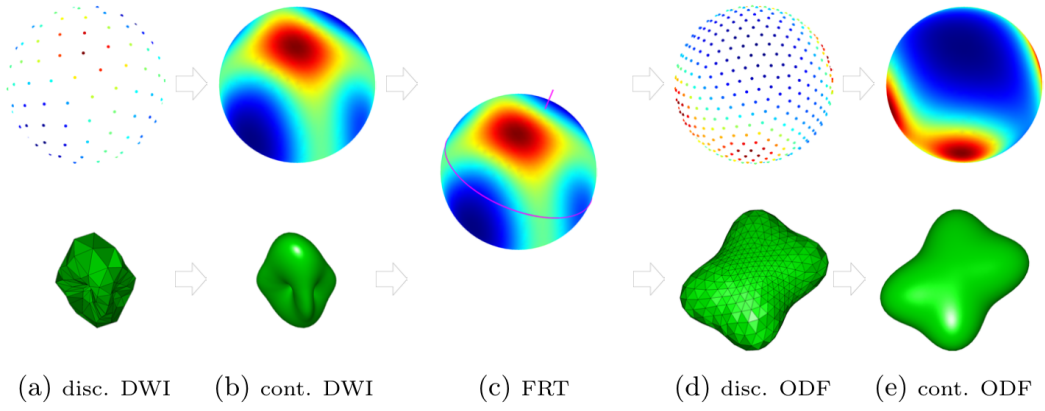

Figure 2.9 – Overview of the Q-ball imaging algorithm. First, the set of discrete measurements on a sphere in q-space (a) are interpolated to a continuous representation (b). On the interpolated measurements the FRT (c) is performed for a set of discrete ODF sample points (d) by taking equal steps along the great circle and summing all the q-space samples. Finally, the discrete ODF (d) is interpolated again to yield a continuous representation of the ODF (e). From [Jeurissen, 2012]

2.4.3 Spherical deconvolution

Another approach to reconstruct the ODF is to perform a deconvolution on the sphere between the DWI signal and a response function [J.-D. Tournier et al., 2004]. This method

is based on the assumption that the diffusion properties of every fiber population present in the brain are uniform, meaning that apart for their orientation and from the point of view of diffusion, nothing can distinguish several fibers taken from different parts of the brain. Moreover, we suppose that the diffusion signal measured by the scanner can be approximated by the sum of the individual contribution of every fiber bundle orientation present within the voxel, weighted by their respective volume fractions. With this conditions, in [J.-D. Tournier et al., 2004], authors demonstrated that the DWI signal $S(\theta, \phi)$ can be expressed as the convolution on the unit sphere between the ODF $\Psi(\theta, \phi)$ and a response function $R(\theta)$ (see Figure 2.10).

$$S(\theta, \phi) = \Psi(\theta, \phi) \circledast R(\theta) \tag{2.32}$$

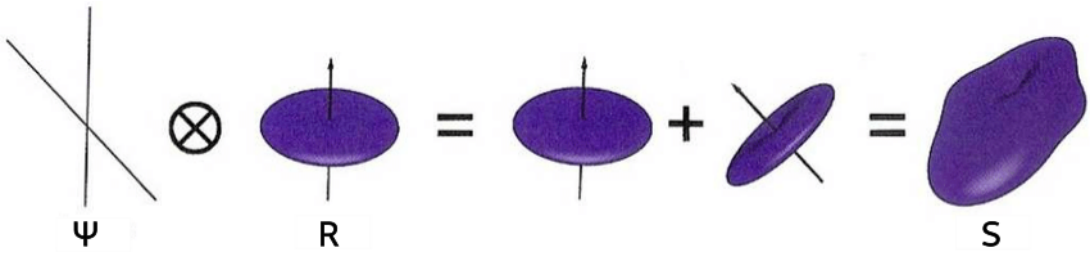

Figure 2.10 – Spherical convolution illustration. The DWI signal (S) is the convolution between the ODF (Ψ) and a single fiber response function (R). In this example the convolution is obtained by rotating the response function to match each ODF peaks and summing the resulting DW signal profiles. From [Johansen-Berg and Rushworth, 2009]

The response function is estimated from the data by analyzing the DW signal profile in regions characterized by the highest diffusion anisotropy. It represents the typical DW signal profile for a fiber bundle. If $S(\theta, \phi)$ is sampled along a large numbers of directions and $R(\theta)$ is known, then $\Psi(\theta, \phi)$ can be recover through a spherical deconvolution. The process of spherical convolution can be expressed as the effect of a combination of rotations applied to a function defined across a sphere [Healy et al., 1998]. Thus, using a set of rotational harmonics (i.e. a basis similar to the SH basis which represent function on the rotational space [Healy et al., 1998]) and a set of modified SH basis as described before, $S(\theta, \phi)$ can be given by:

$$S = R.\Psi \tag{2.33}$$

with the $(N \times N)$ matrix R representing the rotational harmonic decomposition of $R(\theta)$ and where S and Ψ are the $(N \times 1)$ vectors the DW signal and the SH coefficient,

respectively. The spherical deconvolution can then be performed by simply inverting the R matrix [J.-D. Tournier et al., 2004]:

$$\Psi = R^{-1}.S \tag{2.34}$$

The maximum harmonic order, N_{max}, determines the angular resolution of the ODF estimation but is limited by the numbers DW acquisitions. In addition, at high harmonic order, noise can produces false high frequency lobes in the fODF, as well as implausible negative lobes. One solution is to low-pass filter those high frequency lobes to reduces the impact of the noise (see Figure 2.11.a,b,c,d and Figure 2.12.a,b,c,d). However, for orders higher than 8, the lobes must be so attenuated that they no longer introduce any improvements in the angular resolution of the ODF. Moreover truncating the SH basis induces, similar to the Gibbs phenomenon with the Fourier transform, also creates small impossible negative lobes.

2.4.4 Constrained spherical deconvolution

In the absence of low-pass filtering, the noise will cause the reconstructed FOD to contain physically implausible large false negative lobes. An other approach to reduces the effect of noise on the reconstruction is to add a constraint on the presence of negative values in the ODF. Indeed, since the ODF lobes amplitude are supposed to be zero when they are not along a fiber direction, constraining these lobes to zero does not cause any loss of information, but decreases the high frequency noise and thus increase the angular resolution (see Figure 2.11.e and Figure 2.12.e). This method is referred as constrained spherical deconvolution (CSD) [J.-D. Tournier et al., 2007] and will be described now.

The non-negativity constraint is applied through an iterative process. First, an initial estimate of the ODF is obtained using unconstrained spherical deconvolution. Next, the amplitude u of the ODF is computed along a large numbers of evenly distributed directions sampled on the sphere (typically 300 directions, calculated using an electrostatic repulsion model [Jones et al., 1999]):

$$u = P.f_i \tag{2.35}$$

where f_i is SH coefficients vector and P is a matrix that maps f_i onto the amplitude u.

Then, a Tikhonov regularisation [Hansen, 1994] is used to estimated an improved ODF

called f_{i+1} by solving:

$$f_{i+1} = \underset{f_i}{\operatorname{argmin}}\{||Af_i - S||^2 + \lambda||Lf_i||^2\} \tag{2.36}$$

where A is the matrix performing the spherical deconvolution and S the DW signal intensities. The first term represent the spherical deconvolution and ensure that the ODF remains consistent with the DW signal. The second term is the regularisation term, which applies the non-negativity constraint. λ is the regularisation parameter, which controls the relative weighting between these two terms. L is the constraint matrix and is given by:

$$L = \begin{cases} P & \text{if } u < \tau \\ 0 & \text{if } u \geq \tau \end{cases} \tag{2.37}$$

where τ is is a user-specified threshold, controlling the amplitude below which the corresponding ODF is assumed to be zero and is typically set to 10% of the mean ODF amplitude.

A new matrix L is then computed using the improved ODF f_{i+1} and the process is repeated until there is no change change in L. i.e. until the collection of directions that can be considered to have zero fibre density is established. The numbers of iteration needed is typically between 5 and 10.

This method allows to estimate ODF with smaller b-value than with the original spherical deconvolution method, while increasing the angular resolution, the maximum SH order, and the robustness against noise.

Multi-shell multi-tissue constrained spherical deconvolution

Although CSD overcomes many limitations inherent to QBI and DTI estimation, it can only be estimated from single shell data (i.e. an unique b-value). However, modern DWI sequences enable to acquire multi-shell images [D. C. Alexander, 2008; H. Zhang et al., 2012b] so only using one shell can potentially discard valuable information from the other shells. Moreover, when several tissues (WM, grey matter, cerebrospinal fluid) are present within the voxel, CSD is known to produce unreliable and noisy ODF [Roine et al., 2014]. To address these issues, a generalization of the CSD, the multi-shell multi-tissue constrained spherical deconvolution (msmt-CSD) has been developed [Jeurissen, Tournier, et al., 2014].

The formulation of the msmt-CSD is a generalization of equation 2.36 under the form

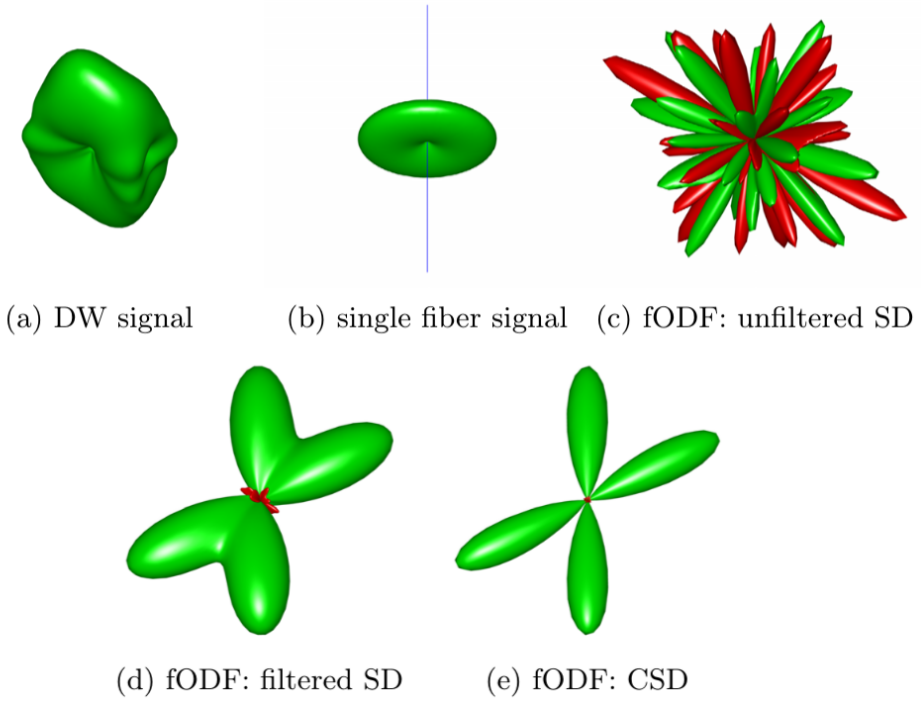

Figure 2.11 – Spherical deconvolution of a noisy DW signal (a) with a single fiber response function (b) using unfiltered (c), filtered (d) and constrained (e). Green indicates positive amplitude, while red indicates negative amplitude. From [Jeurissen, 2012]

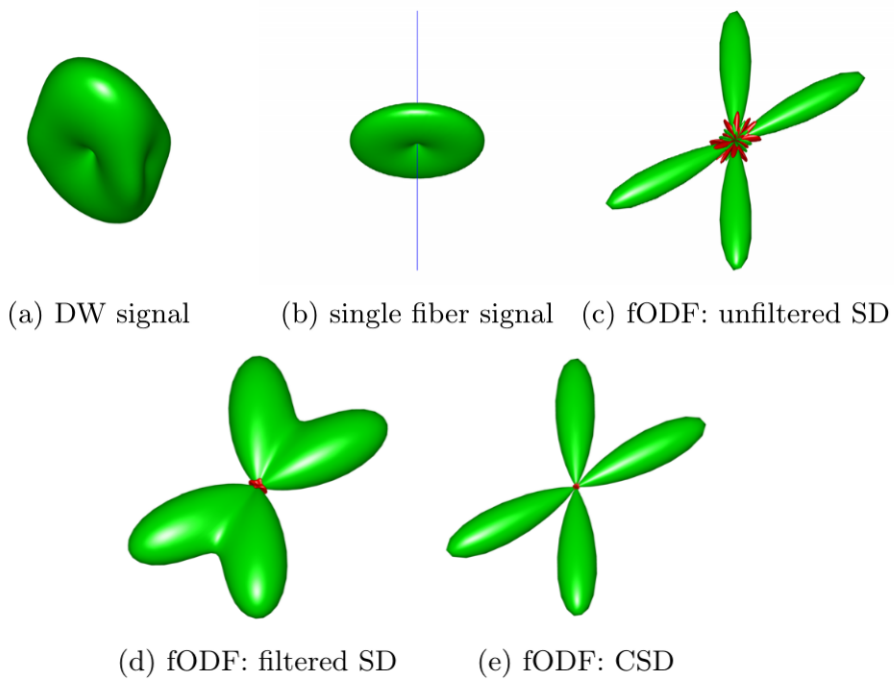

Figure 2.12 – Spherical deconvolution of a noiseless DW signal (a) with a single fiber response function (b) using unfiltered (c), filtered (d) and constrained (e). Green indicates positive amplitude, while red indicates negative amplitude. From [Jeurissen, 2012]

of a convex quadratic programming problem and is given by:

$$\hat{x} = \arg\min_x \frac{1}{2} x^T H x + f^T x \quad \text{subject to} \quad Ax \geq 0 \tag{2.38}$$

With

$$H = A^T A \qquad \text{and} \qquad f = -A^T S$$

Where x is the $(1 \times j)$ vector of the SH coefficients for the tissue j, A is the spherical deconvolution matrix and S is the $(1 \times i)$ vector of the DW signal measured on the S_i shell. This equation can be solved using convex quadratic programming solvers such as the primal-dual interior-point method [Mehrotra, 1992]. It is shown in [Jeurissen, Tournier, et al., 2014] that msmt-CSD allows to exploit multi-shell data to estimate a multi-tissue ODF and to improve the precision of the ODF and suppress almost all negative peaks.

2.5 White matter fiber tractography

2.5.1 Introduction

White matter fiber tractography, simply called tractography in the rest of this manuscript, aims to infer the global long-range brain connectivity from the diffusion models described in the previous sections. The generated connectivity map is called a tractogram. These methods greatly facilitated the diagnosis of neurological pathologies in the clinical context, and provided new insights in the academic context for the study and understanding of the brain.

Most tractography algorithm can be separated into three categories: the local deterministic methods, the local probabilistic methods and the global methods. The local methods track fibers independently of each other based on local diffusion information. The global methods are based on an optimization scheme that simultaneously compares the construction of all fibers, so that the creation of one fiber is constrained by the others ones.

2.5.2 Local deterministic methods

Local deterministic method was the first one to be proposed. [Mori et al., 1999; P. J. Basser et al., 2000 ; Poupon, 1999 ; J.-D. Tournier et al., 2012 ; Johansen-Berg and Behrens, 2014 ; Descoteaux, 2008; Catani et al., 2002 ; Jones et al., 1999 ; Hagmann

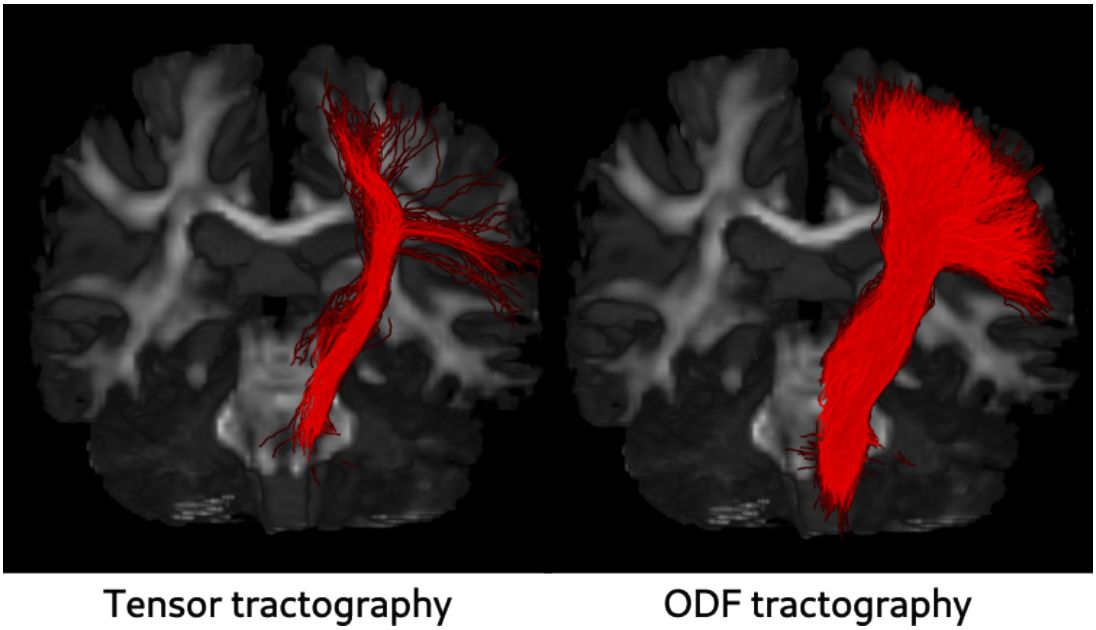

Figure 2.13 – DTI and ODF based tractography.

et al., 2007 ; Savadjiev et al., 2006 ; Merlet et al., 2012 ; Lazar, Weinstein, et al., 2003]. It consists in iteratively following the maximum of the local diffusion model that is most aligned with the previous direction, from one step to the next, until one of the stopping criteria is met. Among the many deterministic methods developed, we can mention in particular the Fiber Assignment by Continuous Tracking (FACT) method [Mori et al., 1999], the Tensor Deflection method (TEND) [Lazar, Weinstein, et al., 2003] and the SD-Stream method [J.-D. Tournier et al., 2004] Which, unlike the previous two method, use ODF imaging to represent the local orientation.

In order to reduce the propagation errors, two propagation distance (or step size) options are commonly used:

— A fixed step size chosen by the user (typically of the order of the size of a voxel edge in the image) combined to a quadratic interpolation method to determine the local orientations [Descoteaux, 2008; J.-D. Tournier et al., 2012].
— A step size dependent on voxel size [Jones, 2008b].

Different propagation methods are available [Jeurissen, 2012; Jeurissen et al., 2019b] (see Figure 2.14 for a visual example). Given a seed point r_0, the 3D vector field representing the local diffusion orientations $v[.]$ and a step size Δ, a fiber (or streamline) can

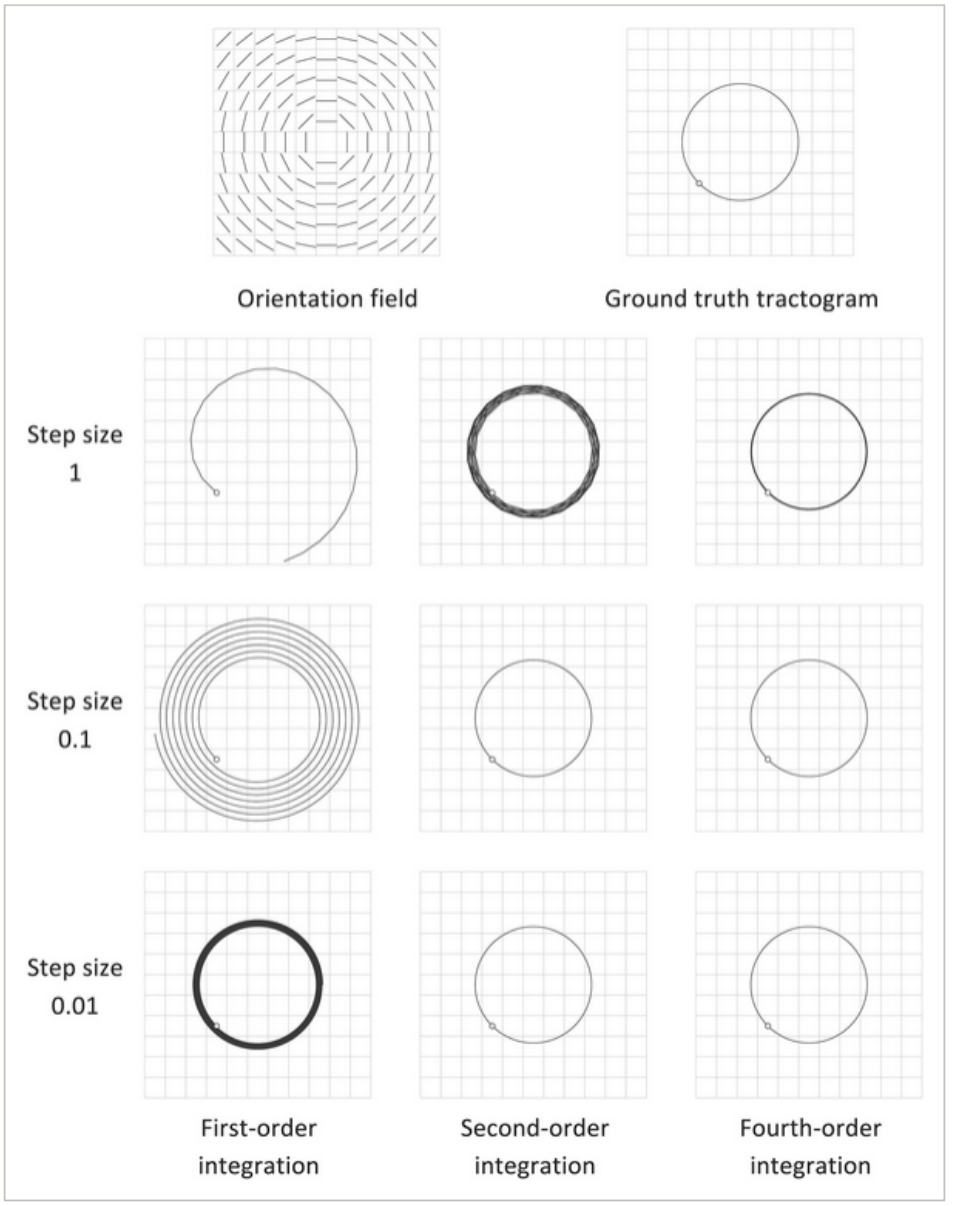

Figure 2.14 – Comparison of integration methods for different step sizes. The seed point is indicated as a white dot. Note that, as we move away from the seed point, the integration errors accumulate. For first-order integration the accumulated error can become quite large, especially for large step sizes. Using higher-order integration schemes drastically reduces the interpolation error made at each step, resulting in a much smaller accumulated error (even for relatively large step sizes) From [Jeurissen, Tournier, et al., 2014

be represented as a $3D$ space curve, parameterized by its arc length s and described by :

$$r(s) = r_0 + \int_0^{\Delta} v[r(s)]ds \tag{2.39}$$

Where $r(s)$ is the position along the streamline.

Typically, numerical integration of the preceding equation is carried out using Euler or Runge-Kutta schemes, often of order 2 or 4. In the case of Euler integration, the discrete evolution equation is as follows:

$$r_{i+1} = r_i + v(r_i)\Delta \tag{2.40}$$

The orientation $v(r_i)$ being constant the propagation, the major disadvantage of this method is that it is prone to accumulating propagation errors in highly curved regions. In order to be able to correctly reconstruct the fibers in those regions, higher-order numerical integration methods have been suggested, including the second-order Runge-Kutta scheme :

$$r_{i+1} = r_i + v(r_i + v(r_i)\frac{\Delta}{2})\Delta \tag{2.41}$$

Or the fourth-order Runge-Kutta scheme:

$$r_{i+1} = r_i + \frac{k_1}{6} + \frac{k_2}{3} + \frac{k_3}{3} + \frac{k_4}{6} \tag{2.42}$$

Where

$$\begin{aligned} k_1 &= v(r_i)\Delta \\ k_2 &= v(r_i + \tfrac{k_1}{2})\Delta \\ k_3 &= v(r_i + \tfrac{k_2}{2})\Delta \\ k_4 &= v(r_i + k_3)\Delta \end{aligned}$$

While deterministic tractography remains prevalent in clinical applications, research has indicated its limitations in accurately representing brain connectivity [T. E. J. Behrens et al., 2003]. These limitations primarily stem from two factors: the accumulation of propagation errors during the tracking process inherent to integration methods and the inherent noise in the DWI, which introduces uncertainty in local diffusion estimates. Deterministic methods are ill-equipped to effectively address this noise-induced uncertainty.

Although deterministic tractography is still widely used in the clinical context, it has been shown that these method failed to correctly describe the brain connectivity because

of, first, the accumulation of the propagation errors during the tracking inherent to the integration process, and second, DWIs being a noisy method causing uncertainty of the local diffusion estimation that deterministic method cannot take into account.

2.5.3 Local probabilistic methods

The aim of local probabilistic tractography algorithms is to characterize the uncertainty inherent to the DWI noise and to the diffusion orientation estimation inaccuracies and which introduces errors in the streamlines pathways [Jones, 2003; Lazar, Weinstein, et al., 2003], in order to produce a more realistic representation of the brain connectivity. Fundamentally, probabilistic algorithms do not differ much from the deterministic algorithms. They initialize seeds in the brain, propagate a fiber from a collection of rules and stop propagation when certain stopping conditions are met. But, whereas the deterministic method considers only one main orientation per voxel, the probabilistic method will generate several possible streamlines directions, a distribution of possible trajectories, at each propagation step. The probabilistic tractography algorithms use these local probability distributions functions (PDF) to estimate the probability that a fibre pathway (or streamline) leaving the 'seed voxel' will pass through any other voxel. The result of a probabilistic method is therefore a map representing the probability of the presence of a connection between different regions of the brain [T. E. J. Behrens et al., 2003, Parker et al., 2003]. The probabilistic tractograms contains more spurious fibers than the deterministic ones, but the streamlines pathways also provides richer and more accurate quantitative information [Côté et al., 2013b]] as these methods allow to traverse regions of high uncertainty where deterministic approaches would have stopped the tracking process.

Several different diffusion PDF estimation methods have been developed and can be found in the literature:

The random walk methods involve reconstructing orientation distributions through a Monte Carlo random walk. These methods have found applications in both DTI and ODF. In ODF-based algorithms, the local PDF is estimated either by directly sampling from the ODF [J.-D. Tournier et al., 2005] or by first fitting the parameters of another distribution and then sampling from it [Seunarine et al., 2007]. Conversely, in DTI-based algorithms, the random walk properties are associated with the DTI model specific to the voxel under examination. The fibers are then tracked using a front evolution process or by generating a family of possible trajectories [Parker et al., 2003]. The primary limitation of these approaches is that they rely solely on the diffusion model and make the assumption

that it accurately captures local diffusion phenomena. Consequently, to a lesser degree, they encounter similar challenges as deterministic methods.

The Bayesian methods, are based on a posterior probability density functions using Bayes theorem, which states that the posterior probability of the model knowing the data, $P(M|D)$ is given by:

$$P(M|D) = \frac{P(D|M).P(M)}{P(D)} \tag{2.43}$$

where $P(D|M)$ is the likelihood, $P(M)$ is the prior probability density functions and $P(D)$ a normalization term. The likelihood needs to encompass the parametric assumptions related to both the relationship between the model parameters and the data, as well as the noise parameters. [T. E. J. Behrens et al., 2007; Kaden et al., 2007; Hosey et al., 2005]. Based on the chosen parametric models, a Markov chain Monte Carlo (MCMC) method can be used to reconstruct the actual distributions of the parameters [T. E. J. Behrens et al., 2003, Hosey et al., 2005, T. E. J. Behrens et al., 2007, Kaden et al., 2007]. The streamlines are then propagated by sampling the possible directions from the posterior distribution.

The bootstrap methods, are based on the bootstrapping method, which is a statistical method for deriving measures of accuracy on statistical samples. One solution to implement bootstrap in a tractography context is to utilize multiple sets of DWI obtained from the same patient to construct the PDF [Jones and Pierpaoli, 2005]. However, this approach necessitates a significant number of acquisitions, which is impractical in practice due to the time-consuming, expensive, and potentially stressful nature of MRI examinations for patients. Another strategy involves utilizing the 'WILD bootstrap' method, which enables the retrieval of probability distributions through iterative resampling of residuals obtained from the diffusion model fitting process [Jones, 2008b]. This technique therefore does not require multiple sets of DWI scans. This method has been used with DTI [Jones, 2008b], QBI [Cohen-Adad et al., 2011] and CSD tractography [Jeurissen, Leemans, Jones, et al., 2011].

Once the diffusion PDF is obtained, the streamlines are tracked using either a deterministic approach by following the most probable direction or by using a rejection sampling method to choose the direction from the diffusion PDF [J.-D. Tournier et al., 2010a; J.-D. Tournier et al., 2012], or using a front propagation algorithm that determine the path globally minimizing the path between two regions [Jeurissen, Leemans, Jones, et al., 2011], or using a particle filtering framework [Stamm, Commowick, Barillot, and

Pérez, 2013b], or finally using a parallel transport frames framework [D. B. Aydogan and Shi, 2020].

2.5.4 Global methods

Contrary to local methods, which track a single fiber at a time based on local orientation, global methods generate multiple streamlines or even the entire tractogram by employing techniques such as minimizing a global distance function, maximizing the probability of connections, or utilizing graph-based or geodesic-based approaches. [Fillard et al., 2011 ; Kreher et al., 2008 ; Reisert et al., 2011]. Global tractography methods are generally more accurate and produce fewer false positives than local methods [Fillard et al., 2011], but those algorithms requires much more calculation time than deterministic or probabilistic tractography. Several different strategies exist for implementing global tractography methods [Girard, 2016]:

Global energy minimisation algorithms aims to generate tractograms that best match to the underlying diffusion data while respecting basic assumptions about the WM fibers organisation. Tractography is then expressed as a problem minimizing the energy of a system of interacting segments [Fillard et al., 2009 ; Kreher et al., 2008 ; Reisert et al., 2011].

Geodesic tractography algorithms are designed to reconstruct fibers by determining the shortest path between the two endpoints of the streamline within the curved space defined by the white matter and the local diffusion orientation metrics. In this context the streamlines are seen as geodesic, representing the shortest path between two points on a curved surface according to a specific metric. This concept is a generalization of the notion of a straight line in Euclidean space. Several methods have been proposed for recover the geodesic path [Jbabdi, Bellec, et al., 2007 ; Sepasian, 2011 ; D. S. Tuch et al., 2000; Lenglet et al., 2004 ; Parker et al., 2002 ; Pichon et al., 2005; Campbell et al., 2005].

Graph theory. Unlike geodesic approaches, where a graph is constructed and explored dynamically in the diffusion space, this category of methods explicitly constructs a graph from the image, where nodes are generally linked to voxels and edges represent the distance or probability of connection between nodes. Various graph traversal algorithms are then applied to search for graph connectivity features [Collins et al., 2010; Oguz et al., 2012 ; Iturria-medina et al., 2008 ; Sotiropoulos et al., 2010b].

Probabilistic approaches. These methods look for one or more tracts with the highest probability of connecting two regions. The tractography problem is posed within

a Bayesian inference framework. The advantage of these approaches is that they naturally provide information on the uncertainty of a connection [Jbabdi, Bellec, et al., 2007 ; Friman et al., 2006 ; F. Zhang et al., 2009 ; Pontabry and Rousseau, 2011 ; Wu et al., 2009 ; Zalesky, 2008 ; Schreiber et al., 2014].

A more detailed review of existing global tractography methods can be found in [R. E. Smith et al., 2020].

2.5.5 Tractograms post-filtering

Instead of focusing on optimizing the initial fiber estimation, an alternative category of methods seeks to refine tractograms after they have been generated using one of the previously described techniques. This section presents the main categories of tractogram filtering methods.

Filtering from the diffusion signal

These techniques involve assigning weights to individual fibers with the aim of providing an effective interpretation of the diffusion measurements. The objective is to estimate synthetic diffusion data based on a tractogram and subsequently compare it to the actual acquired diffusion data. If a significant disparity exists between these two sets of measurements, the fiber responsible for the synthetic data is pruned or eliminated from the tractogram. Here we can mention : Linear Fascicle Evaluation (LiFE) [Caiafa and Pestilli, 2017; Pestilli et al., 2014], Convex Optimization Modeling for Microstructure Informed Tractography (COMMIT) [Daducci, Palù, et al., 2015; Schiavi et al., 2020], Spherical-deconvolution Informed Filtering of Tractograms (SIFT) [R. E. Smith et al., 2013] and SIFT2 [R. E. Smith et al., 2015].

Filtering from regions of interest

Other approaches involve applying anatomical constraints through the use of segmentation masks to filter out streamlines that do not adhere to plausible anatomical structures. First, Smith et al. proposed to remove streamlines that fall outside an exclusion mask based on an atlas-based tractogram [S. M. Smith et al., 2006]. More recently, the segmentation masks were directly estimated from dMRI data. The TractSeg algorithm, [Wasserthal et al., 2018c; Wasserthal et al., 2019], adopts this approach by training a neural network to segment inclusion masks for 72 different fiber bundles.

Filtering from the streamlines geometry

In this methods, the determination of streamline plausibility is based on their shapes themselves. For example, ExTractor, [Petit et al., 2021], employs simple geometric priors to evaluate the credibility of streamlines. Additionally, there has been a proliferation of deep learning-based methods for tractogram filtering, with many of them primarily relying on streamline geometry as a criterion. Notable examples include FiberNet [Gupta et al., 2017], FiberMap [F. Zhang et al., 2019] and TRAFIC [Lam et al., 2018]. Some studies have also demonstrated that incorporating additional geometric priors derived from population data can be used to assess the plausibility of streamlines at a local level [Tax et al., 2016; Dong et al., 2017; Brusini et al., 2019].

Tractograms clustering

Streamlines are grouped into bundles prior to more extensive analysis. These clusters can serve as representations of the underlying white matter structure. Fibers within small clusters or those that do not exhibit properties consistent with the bundles of interest can be eliminated. Notable methods for performing this clustering include Quickbundles [Garyfallidis et al., 2012], Recobundles [Garyfallidis et al., 2017], which employs an atlas-based approach, and BundleMAP [Khatami et al., 2017], utilizing support vector machines.

A comprehensive review of a posteriori filtering methods can be found in [Jörgens et al., 2021].

2.5.6 Tractography parameters

Although the literature reports on a plethora of different tractography methods, each with its own unique characteristics, they all share five key parameters that require meticulous adjustment, depending on the nature of the study or experiment in question:

— A tracking mask that defines the region in which tractography is to be conducted.
— A step size
— An interpolation method
— A seeding method, which initialise the first points of the fibers.
— A collection of stopping criteria that terminate the fiber tracking

We have previously discussed the step size and interpolation method in section 2.5.2, and therefore, we will not delve into them again.

The seeding method is generally common to all algorithms. A first option is to carry a region of interest (ROI) based tractography, in this case the seeds are either generated by the user by manually selecting the seed voxel, or by using a ROI atlas produced by experts or they can also be obtained from cortical activation maps measured with functional MRI (fMRI). The second option is to generate a 'whole-brain' tractogram by initializing the algorithm using either all the voxels in the brain or the voxels at the interface between the WM and the GM.

Several common stop criteria exist and are used either alone or in combination.

The first one is the propagation limit domain, or tracking mask. Most algorithms need a binary mask matching the propagation domain to support the tracking. Leaving this mask cause the tracking to stop. The mask can be obtained from the b_0 image (i.e. the DWI without applied gradient) or by binarizing the fractional anisotropy map with a threshold typically set below 0.2.

An other criterion is the angle defined between two successive fiber segments. This criteria is based on the hypothesis that WM fibers follows a relatively 'smooth' geometry, characterized by a low curvature. Thus, a fiber pathways is stopped if, during the tracking process, the angle between the previous and the actual directions is superior to a user defined threshold (typically around 30°).

Finally, one last common criterion used is most tractography algorithm relies on the final length of the tracked fibers by setting a minimal and a maximal fibers length (typically $5mm$ and $300mm$). This allows to discard all the short fibers that correspond to false-positives generated by the tracking method, and also prevent the algorithm to enter in an infinite loop.

2.5.7 Limitations of tractography

In spite of the advancements achieved in data acquisition and the refinement of fiber pathway estimation techniques, tractography algorithms still face various limitations. These limitations not only hinder their clinical utility but also pose challenges in the study of the brain. Tractograms, in particular, face issues related to accuracy, quantifiability, and interpretability [Jbabdi and Johansen-Berg, 2011b]. In [Pujol et al., 2015], authors asked 8 different international teams to reconstruct the pyramidal bundle in four patients with gliomas near the motor cortex with DTI-based tractography. The results showed that, while most of the methods have been able to correctly reconstruct the pyramidal bundle, all share great inter-algorithm variability. In an other study, [K. Maier-Hein

et al., 2017b] evaluated 96 distinct tractography pipelines submitted by 20 different research groups, in order to assess how well the algorithms were able to reproduce the known connectivity. They demonstrated that most methods produce tractograms containing 90% of the ground truth bundles, but that these tractograms also contain many more invalid than valid bundles.

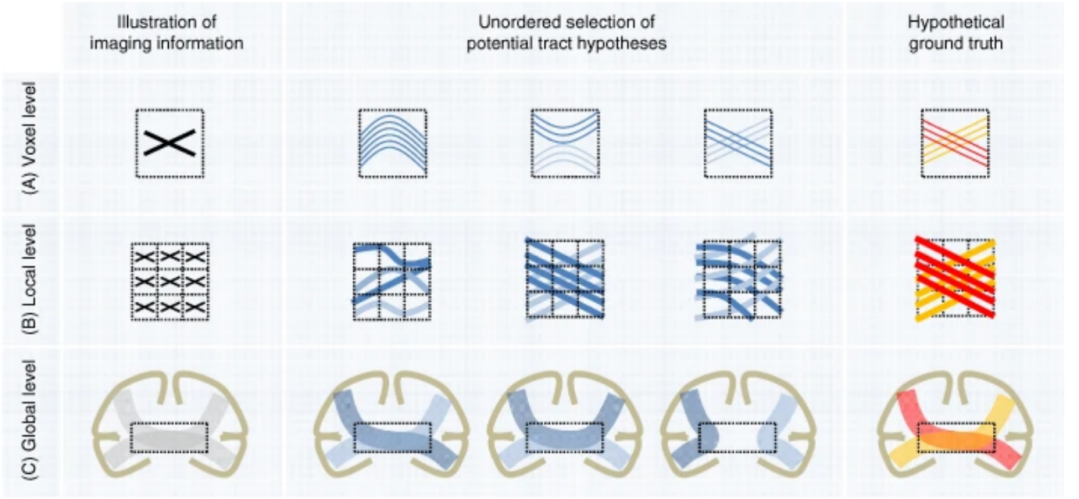

Figure 2.15 – Illustration of the bottleneck issue. (A) The presence of fiber crossings within a voxel in the hypothetical ground truth creates ambiguous information in the imaging data at the voxel level. (B) Similarly, the same fiber configuration can be explained by several different local diffusion structures. (C) At a global level, white matter regions that are shared by multiple bundles (so-called "bottlenecks", dotted rectangles) can lead to many false fibers reconstruction. Ultimately, with only two bundles in the hypothetical ground truth, four potential false positive bundles can be reconstructed. From [K. Maier-Hein et al., 2017b

These studies [Pujol et al., 2015; K. Maier-Hein et al., 2017b; Rheault et al., 2020] highlight the same limitations shared by all tractography algorithms:

— Due to the inherent scale disparity between MRI voxel dimensions and axon radius, the precise identification of fiber origins and departure points becomes an intricate task

— The limited reproducibility and consistency of results across various algorithms pose significant challenges when conducting large-scale analyses or longitudinal comparisons.

— The generation of a multitude of false positives often arises from local models being unable to adequately address complex configurations or lacking sufficient additional anatomical information, particularly in scenarios involving fiber crossings and other

special configurations.

— The "bottleneck" issue (see Figure 2.15), in regions where multiple white matter bundles converge within a single voxel and share the same parallel orientation, before diverging and continuing towards their final terminations, the algorithms are unable to determine the correct pathways without external information.

Furthermore, the absence of a definitive ground truth or a means to quantify outcomes without resorting to invasive post-mortem procedures presents a significant challenge. Consequently, there is no infallible method available to establish the absolute reliability and validity of tractography algorithm results, which creates uncertainty and complexity in the validation process.

For all these reasons, the validation of tractography algorithms and their ability to make the right decisions in regions with complex configurations and subject to bottlenecks is still an academic challenge and will be studied in the remainder of this manuscript.

Chapter 3

A convolutional Wasserstein distance for tractography evaluation

---

Authors of the article: Thomas Durantel, Julie Coloigner and Olivier Commowick

Submitted, accepted and presented in the 19th International Symposium on Biomedical Imaging (ISBI) in 2022

3.1 Introduction

Diffusion MRI and fiber tractography are promising methods for the evaluation of the brain nervous fiber pathways. Since the emergence of these techniques at the end of the previous century [P. J. Basser et al., 1994a], many new methods have appeared. The first ones were based on tensors, one of the simplest diffusion models [Mori et al., 1999]. Since then, numerous studies have shown the limitations of tensor-based tractography in complex fiber structures [Gao et al., 2013a]. To overpass these limitations, new algorithms, using either other diffusion models (orientation distribution functions [Descoteaux et al., 2007a] or multi-tensors [D. Tuch et al., 2002]) or new probabilistic tractography methods [Stamm et al., 2013; Jones, 2008a], have been developed. These methods have allowed a better reconstruction of complex fiber bundles like the corticospinal tract (CST) or the corpus callosum (CC) [Girard et al., 2020a], but still do not reach an acceptable false positive rate to be used in a clinical context [K. Maier-Hein et al., 2017a].

The large number of existing techniques results in a lot of variability in the reconstruction of fiber bundles, which prevents clinicians from correctly interpreting the results, and makes it difficult to evaluate and compare tractography algorithms [Schilling et al., 2021a].

Hence, many challenges [Côté et al., 2013a; Maffei et al., 2020] have been organized to 1- study the sources of this variability, 2- provide a general framework allowing to more easily compare tractography algorithms. In those challenges, a few probabilistic methods J.-D. Tournier et al., 2010b; R. E. Smith et al., 2012; D. B. Aydogan and Shi, 2021] have shared the first place.

When organizing such challenges or evaluating an algorithm, the question of evaluation of tractograms becomes essential. While visual evaluations are crucial to quickly judge the quality of tractograms, they do not allow for an in-depth comparison and a quantitative performance analysis. Therefore, comparison being at the core of these challenges, measures have been developed to quantify and study differences between methods. First, measures such as the Dice score, its generalized version [Crum et al., 2006a] or density correlation [Schilling et al., 2021a] analyze tractograms as an image derived from the fiber bundles being compared. Second, the anatomical plausibility can be studied with topographic regularity [D. B. Aydogan and Shi, 2018] or, as in TractoMeter, the number of valid connections (VC, the percentage of streamlines that correctly connect both ends of a fiber bundle) and the number of valid streamlines (VS, the percentage of streamlines that are part of VC, and that respect the general shape of the bundle).

As mentioned above, tractograms evaluation measures are a crucial and actual problem that lacks of a general answer. Multiple measures are available in the literature. However, as they work on different objects or quantities derived from tractograms, it is probable that one measure does not explain fully tractograms variations and errors, nor that they expose the same kind of errors. This has however never been explored in the literature. We thus propose first to study and compare the behavior of the most common of these measures when the reference and tested tractograms diverge from each other. This is done using simulated data by applying linear and non linear transformations, and also comparing results of different tractography algorithms in real cases. We also define and evaluate a new tractogram evaluation measure based on optimal transport. This measure provides a distance between two distributions and thus encompass information on both topographical similarities and the degree of overlap between two tractograms. We ultimately illustrate its value when used in conjunction with other metrics.

3.2 Background

3.2.1 Tractograms evaluation metrics

To assess the performance of our metric, we opted to compare it against four established measures commonly used in recent studies, [Côté et al., 2013a; Schilling et al., 2021a], to evaluate the quality of tractograms.

The generalized Dice score. The Dice and generalized Dice scores measure the overlap between a reference and a test image. There are several generalizations of the binary Dice score. We have chosen the one proposed in [Crum et al., 2006a] wich is defined as :

$$\text{Dice} = \frac{2\sum_i \min(A_i, B_i)}{\sum_i (A_i + B_i)} \tag{3.1}$$

with Dice $\in [0, 1]$ (0 corresponding to no overlap and 1 to perfect overlap), and A_i, B_i being respectively the reference and the test image values at voxel i.

Unlike the original Dice score, that assumes binary image inputs, the generalized Dice score handles weighted images. In the case of tractograms, these images are fiber density images (i.e. the weight of a voxel is the number of streamlines that pass through it). That property allows this measure to give more importance to the most dense regions.

The density correlation. This measure corresponds to the cross-correlation coefficient between the reference density image and the test density image, such as:

$$\text{Corr} = \frac{\sum_i (A_i - \overline{A})(B_i - \overline{B})}{\sqrt{\sum_i (A_i - \overline{A})^2 \sum_i (B_i - \overline{B})^2}} \tag{3.2}$$

with $\rho \in [-1, 1]$, A_i and B_i the value of the corresponding image at voxel i, and $\overline{A}$ and $\overline{B}$ the average voxel value of reference and test density images.

Contrary to the generalized Dice score, this metric provides insights into the similarity of streamline density rather than solely measuring the degree of overlap between streamlines and a reference. While the generalized Dice score primarily evaluates how well streamlines match a reference, the density correlation metric delves deeper by assessing the concordance in the density distribution of streamlines, offering a more comprehensive perspective on tractogram quality and consistency.

The number of valid connections. In many cases, obtaining the ground truth of tractography is difficult. Some measures thus assume that we do not know the complete

ground truth tractogram but rather only the start and end regions to which the fibers should pass through. In this case, the evaluation measure can be defined by counting fibers of the evaluated tractogram that actually start and stop in these regions. This percentage is named valid connections (VC) and was used in the TractoMeter challenge [Côté et al., 2013a].

The number of valid streamlines. Going one step further than VC, we can consider that, in addition to the start and end ROIs, we also know the envelope of the ground truth tractogram. If the full ground truth tractogram is available, this envelope can be extracted as a binary image highlighting voxels where at least one fiber passes through. The percentage of valid streamlines (VS) is then the percentage of all streamlines that are part of Valid Connections, and that do not leave the ground truth envelope. Hence the percentage of valid streamlines will always be lower than the percentage of valid connections.

3.2.2 Optimal transport

In this paper, we present a novel evaluation metric that relies on calculating the Wasserstein distance, a concept derived from optimal transport theory. We will begin by introducing these theoretical concepts and subsequently demonstrate their application in evaluating tractograms.

Let μ_0 and μ_1 be, respectively, a source and a target distributions and $\pi(x, y)$ a transport plan that describes the amount of mass transported from μ_0 at location x to μ_1 at location y. The 2-Wasserstein distance, simply called Wasserstein distance in the following, defines a distance that can be used to measure the discrepancy between two distributions, given by Eq. 3.3:

$$W_{2,\gamma}^2(\mu_0, \mu_1) = \inf_{\pi \in \Pi} [\iint_{M \times M} d(x, y)^2 \pi(x, y)\, dx\, dy - \gamma H(\pi)] \tag{3.3}$$

where M is a compact, connected Riemannian manifold and $d(x, y)$ is the distance function between two elements $x \in M$ and $y \in M$.

The last term of Eq. 3.3, $\gamma H(\pi)$, is an entropic regularization term which is used to smooth the function and thus to provide a unique solution to the problem.

Many methods have been devised in the literature to obtain this solution [Bonneel and Coeurjolly, 2019; Figalli, 2010]. Among these, the Sinkhorn algorithm [Cuturi, 2013] is the most commonly employed approach. However, this algorithm exhibits two signifi-

cant limitations. Firstly, it is an iterative algorithm that may require an extended period to reach convergence. Secondly, in the context of comparing two distributions of fibers, which in our case represent the individual fiber contributions at each point in the tractogram, the sheer quantity of pairwise distances that need to be calculated between these distributions can rapidly become overwhelming. This results in increased computational time and memory usage, especially considering that a typical fiber bundle may consist of up to $50,000$ points, necessitating the computation and storage of $50,000^2$ distances for computational efficiency.

Consequently, we have opted to utilize a recently efficient algorithm proposed by Solomon et al. [Solomon et al., 2015]. This method leverages Varadhan's formula to replace the kernel of the Sinkhorn algorithm with a Gaussian kernel derived from the heat equation, specifically when working with distributions represented as 3D images. The algorithm is based on two equations, denoted as Equation 3.4 and Equation 3.5:

$$\begin{aligned} v_{i+1} &= \mu_0 \oslash H_t(a \otimes w_i) \\ w_{i+1} &= \mu_1 \oslash H_t(a \otimes v_i) \end{aligned} \tag{3.4}$$

$$W_{2,\gamma}^2(\mu_0, \mu_1) = \gamma a^T[(\mu_0 \otimes \ln(v_i)) + (\mu_1 \otimes \ln(w_i))] \tag{3.5}$$

where μ_0 and μ_1 are a source and a target distributions, respectively. (v, w) are a pair of vector initialised to only contain 1, a is the vector of area weights, such as $a^T\mathbb{1} = 1$, H_t is a Gaussian kernel from the heat equation and γ is the entropic regularization constant.

Considering the tractograms as 3D density images, we can conduct Sinkhorn iterations using 3D Gaussian kernel convolutions. This involves iteratively computing Equation 3.4 and, at each step, evaluating Equation 3.5. This approach proves to be highly efficient in terms of both computational power and memory usage, as these operations can be directly executed on the images without the need to explicitly store the distance matrix.

3.3 Wasserstein distance for tractography evaluation

3.3.1 Methods

To compare the behaviour of the evaluated measures and to test the Wasserstein distance (WD), we performed two sets of experiments, one on simulated data and another

one on real data.

In the first set of experiments, the 5 evaluation measures (Dice, correlation, VC, VS and WD) were computed on 4 controlled transformations cases, often found at least partially in real cases. The data used here is the Cortico-Spinal Tract (CST) of 5 subjects of the Human connectome Project (HCP). This ground truth tract was obtained by Wasserthal et al. [Wasserthal et al., 2018a] by performing fiber tracking using Mrtrix followed by several filtering, first filtering from regions of interest, then filtering manualy by an expert. The 4 experiments were designed as follows:

Translation The reference track is translated along the x-axis from 0 to 12.5 mm, in step of 0.0125 mm.

Rotation The track is rotated around the z-axis (roughly the CST main axis) and the centre of gravity of the bundle by an angle from 0 to 360 degrees, with increments of 1 degree.

Deformation A stationary velocity field (SVF) [Arsigny et al., 2006a] is generated by randomly generating Gaussian weight functions inside the reference fiber bundle mask. To each weight function is associated an individual translation in a random direction, with a random magnitude. The SVF is the weighted combination of these translations using the Gaussian weight functions. In our case, we generated for each deformation from 1 to 75 Gaussian weight functions, with a random translation between 0 and 5 mm. This SVF is then integrated and applied to the tractograms. To characterize the global amplitude of each generated deformation, we compute the average vector norm at each voxel, inside the bundle envelope.

Degradation The track is degraded by randomly removing fibers from 0 to 100 percent of the reference fiber bundle

For each of these simulated dataset, we calculated cross-correlation coefficients between every pair of measurement curves (Dice, Corr, VC, VS and WD). This enabled us to assess the level of complementary between these measures, with lower correlation values indicating a greater degree of complementary information.

The second set of experiments is based on HCP data and more particularly on 3 bundles, the CST, the Optic radiation (OR) and the first Superior longitudinal fascicle (SLF) tracked with the parallel transport frame algorithm Trekker [D. B. Aydogan and Shi, 2021], the Mrtrix3 iFOD2 [J.-D. Tournier et al., 2010b] and the DIPY Probabilistic PFT algorithm [R. E. Smith et al., 2012]. For the 3 algorithms, the default parameters were used and 10000 streamlines were generated by running a whole brain tractography,

then by filtering the results with the start and end ROIs, segmented with TractSeg.

The evaluation was then performed between the ground truth tracks given by [Wasserthal et al., 2018a] and the resulting tractograms. For that experiment, we may note that the evaluation framework forces VC to be at 100%, thus only the other measures (Dice, Corr, VS and WD) were computed. The purpose of these experiments is not to compare the tractography methods but to study the behavior of our WD metrics in comparison with the other classical methods.

3.4 Results

Fig. 3.1 displays the results for the simulated data. For translation, Fig. 3.1.a shows that all measures follow the same behavior, except for VC that seems to provide different information. All combinations have indeed a correlation coefficient above 0.95, except for $\rho(\text{Corr}, \text{VC}) = 0.60$, $\rho(\text{Dice}, \text{VC}) = 0.63$, $\rho(\text{WD}, \text{VC}) = 0.70$ and $\rho(\text{VC}, \text{VS}) = 0.43$. We have a maximum of 0.99 for $\rho(\text{Corr}, \text{Dice})$.

For rotation, Fig. 3.1.b shows the same result as the translation, even more pronounced. We found $\rho(\text{WD}, \text{Corr}) = 0.41$, $\rho(\text{WD}, \text{Dice}) = 0.41$, $\rho(\text{WD}, \text{VC}) = 0.37$ and, $\rho(\text{WD}, \text{VS}) = 0.23$. All other are above 0.90 and the maximum is $\rho(\text{Corr}, \text{Dice}) = 0.99$.

For the deformation (Fig. 3.1.c), linear regression (plus a 95% confidence interval, in transparent on the plot) were computed and plotted to study the correlation between each measure against deformation. VC were not plotted because the major part of the deformation did not occur on the ending parts of the streamlines. The R^2 of each regression are as follows: 0.64 for Dice score, 0.40 for the density correlation, 0.38 for VS and 0.03 for WD. The regression plots show that, the density correlation, the Dice score and VS percentage (red, blue and black) appear to follow the expected trend: the metrics decrease when the average norm increases. However, the relationship between these measures and the average norm may not be linear and the x-axis is probably to simplistic to really conclude here without further experiments.

For degradation (Fig. 3.1.d), VC and VS, which by nature cannot measure a degradation (as the overall shape and the endings of the bundle are not affected), are not computed. Corr and WD are almost identical (except for the curves inversion). Dice follows a different trend, possibly leading to more information. In addition, $\rho(\text{WD}, \text{Corr}) = 0.51$ and $\rho(\text{WD}, \text{Dice}) = 0.48$. All other results are under 0.10. The minimum is $\rho(\text{Corr}, \text{Dice}) = 0.002$.

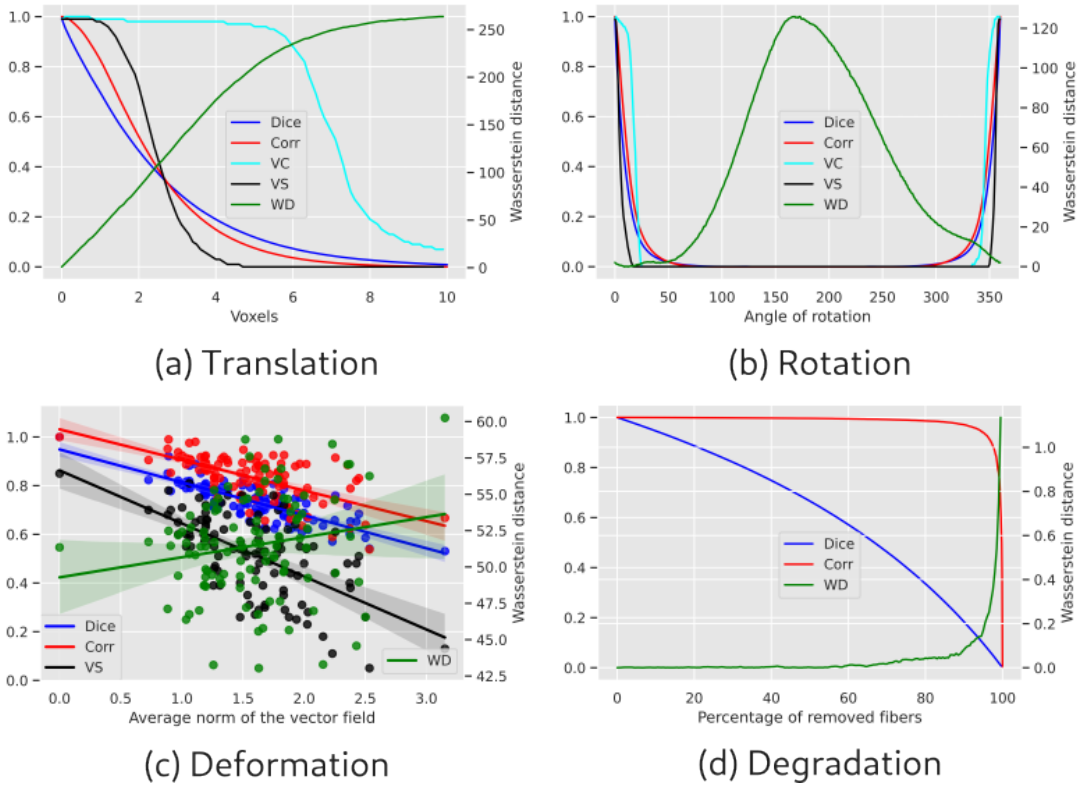

Figure 3.1 – Results for the simulated data. In each scenario, dark blue represents the Dice score, red corresponds to the correlation measure, light blue signifies the VS percentage, black indicates the VS percentage, and green represents the Wasserstein distance. In the deformation scenario, each data point represents a unique deformation, and the lines represent linear regressions applied to the data points for each measurement.

For the second experiment on real data, the evaluation metrics are presented in Table 3.1, and Figure 3.2 displays the resulting tractograms on which measurements were conducted.

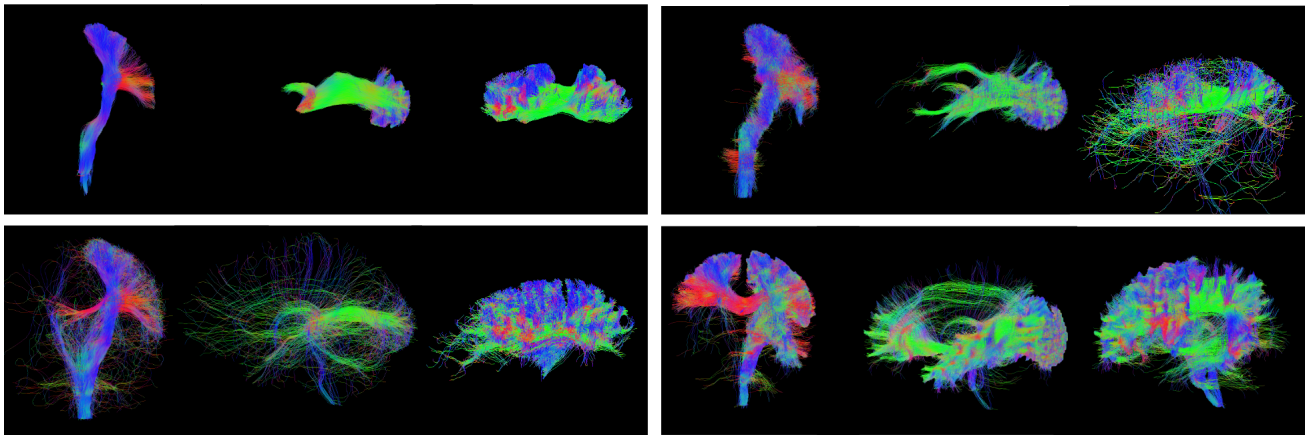

Figure 3.2 – Resulting tractograms for each algorithm. From left to right and top to bottom : the ground truth, Mrtrix IFOD2, Trekker and Dipy PFT. And from left to right in each case : the CST, the OR and the SLF

	Dice	Dens. corr.	WD	VS (%)
CST	0.23/0.18/0.53	0.47/0.36/0.54	37/74/72	42/43/78
OR	0.26/0.22/0.08	0.43/0.34/0.37	48/24/99	45/33/33
SLF	0.29/0.15/0.04	0.55/0.20/0.38	27/16/74	50/38/24

Table 3.1 – Results for real data experiment. Red text denotes results for IFOD2, blue for Trekker, black for Dipy PFT.

3.5 Conclusions and discussions

The cross correlation results for rotation and translation show that, for these transformations, the Dice score and the density correlation do not give complementary information. For translation, VC appears in each combination with the lowest coefficient, meaning that for this type of transformation, streamlines based measures can bring complementary information to image based measures. In the rotation case, the Wasserstein distance is the least correlated with the others, thus, that gives more information on tractogram quality in complement to other measures. The R^2 of the linear regressions for deformation experiment show that these measures have difficulties to evaluate properly deformations in

tractograms. However, this result should be taken with caution since, in this experiment, we tried to reflect local deformations with an average global information which may not be enough to capture the deformations variations. Designing more local evaluation of the deformation magnitude would be beneficial. Finally, for the degradation, all coefficients are relatively low, in particular the density correlation and the Dice score that are almost uncorrelated showing their complementarity.

For real data, results show that, globally, VC, Dice and the correlation follow the same trend. The Wasserstein distance seems to give slightly different information. A more in-depth real data study will bring more information on that aspect.

As shown above, the Wasserstein distance can, in certain cases, be used to deliver information that the other measures cannot. However, we would like to point out some of the actual limits of this distance and therefore some future works that could improve this measure. First, the measure computes a distance between all points of the two tractograms instead of matching fibers, which is not topologically right. A way to transport fibers from a tractogram to another should be examined. Second, special attention must be given to the quantity of mass transported. Indeed, balanced (the same amount of mass on both sides) and unbalanced (different amounts of mass) optimal transport are two different problems, which require different solutions. In this work, balanced optimal transport is forced by normalising the tractograms densities. This can lead to unexpected situations, e.g. with the degradation experiment, where, for a high percentage of degradation, we force an entire tractogram to be transported onto a few fibers.

In conclusion, we have proposed, in this work, a comparative analysis, both on synthetic data (translation, rotation, deformation, degradation) and in real circumstance, of the behavior of a few typically used tractograms evaluation measures: the Dice score, the density correlation, the percentage of valid connections and valid streamlines. We then proposed a new measure, based on optimal transport and compared its behavior against the other measures. We show that, in most cases, it can be useful to use multiple measures in conjunction since they do not correlate and thus bring different kinds of information. We also show that, although still being in development, our new Wasserstein measure can be used to compare tractograms, bringing additional information.

Chapter 4

A Riemannian framework for incorporating white matter bundle priors in ODF-based tractography algorithms.

Authors of the article: Thomas Durantel, Gabriel Girard, Emmanuel Caruyer, Olivier Commowick and Julie Coloigner

A preprint of this work is available at https://hal.science/hal-04246380. In addition, it will be submitted in the coming weeks to the journal Human Brain mapping (HBM).

4.1 Introduction

Diffusion magnetic resonance imaging (dMRI) is an MRI modality that allows to measure the thermal agitation of the water molecule in the brain [E. Stejskal and Tanner, 1965]. This agitation being constrained by the tissues micro-structures, typically the nervous system axons, dMRI enables the voxelwise estimation of the orientations of the white matter fibers [Dell'Acqua and Tournier, 2017; D. Jones, 2010]. By randomly choosing seeds from within the brain white matter, then following, from one voxel to the next, the local fiber orientations, one can achieve to estimate the brain connectivity and characterize the physical connections that mediate information transfer between cortical regions [D. Jones, 2010]. This process is called fibers tracking, or fiber tractography, and the resulting set of white matter trajectories is called tractograms [Mori and Van Zijl, 2002]. The ability of those approaches to delineate the white matter fiber pathways offers unprecedented insight into the structural connections of the human brain and enormous potential for

the study of human brain anatomy, development and function [Jeurissen et al., 2019a]. Moreover, tractography has been proven particularly useful to neurosurgeons for the planning of surgery, especially to preserve important white matter pathways during resections [Mancini et al., 2019].

A multitude of new tracking algorithms has been proposed to improve the quality of the tractograms [Girard et al., 2020b; Schilling et al., 2021b]. The first methods were deterministic methods, where only the principal diffusion orientation of the diffusion tensor was used in each voxel [P. Basser et al., 2000b]. However, studies have shown the difficulties that these methods have to represent complex brain regions, like crossing or fanning fibers [Gao et al., 2013b]. In response, new diffusion model, like the orientation distribution function (ODF) which encodes continuously all the diffusion orientations within a voxel and thus can characterize the complex fiber structure, have been developed [Descoteaux et al., 2008; J. Tournier et al., 2007]. Modern methods have then sought to estimate the fiber dispersion estimation using probabilistic methods [T. Behrens et al., 2007; Jeurissen et al., 2019a; J. Tournier et al., 2019].

Among them, existing local tractography approaches estimate the local fiber orientation at each voxel independently by simultaneously fitting the local model and propagating in the most consistent direction, such as Kalman filtering method [Gössl et al., 2002], particle filtering method [Pontabry et al., 2013; Stamm, Commowick, Barillot, and Perez, 2013], random walks methods [Descoteaux et al., 2008 and graph theory method [Sotiropoulos et al., 2010a]. Other approaches have proposed more global approach which computes multiple fibers pathways and select the best ones based on the diffusion characteristics, like using Bayesian model [Jbabdi, Woolrich, et al., 2007] or the Hough transform [Aganj et al., 2011] and machine learning more recently [Poulin et al., 2019]. However, despite the improvement of the dMRI acquisition, the modeling and the tracking, white matter fibers tractography still can't overcome some limitations [Jbabdi and Johansen-Berg, 2011a; K. H. Maier-Hein et al., 2017] which prevents those methods to be usable in the clinical context. Maier-Hein et al (2017). have shown that most modern algorithms can recover up to 90% of the ground truth white matter bundles, but these are poorly recovered in terms of spatial extent [K. H. Maier-Hein et al., 2017]. Moreover, those tractograms also contained large amounts of invalid bundles [K. H. Maier-Hein et al., 2017]. Overall, the iFOD2 [J. Tournier et al., 2010] and PTT [D. Aydogan and Shi, 2021] algorithms had good performances in recent international challenges [K. H. Maier-Hein et al., 2017; Rafael-Patino et al., 2021b].

To overpass the poor spatial extent of white matter bundles, one proposed solution is to increase the numbers of the total generated streamlines leading to an over representation of easy tracks and an under-representation of difficult tracks, inducing a density bias [Rheault et al., 2017]. For example, the local tractography methods aim to recover a global connectivity by inferring from locals directional information that causes the algorithm to follow, in complex regions, the easiest path available and sometimes the non-realistic decisions [K. H. Maier-Hein et al., 2017]. Various studies have suggested that advanced diffusion microstructure modeling [Daducci et al., 2016; R. Smith et al., 2015], streamline filtering techniques [Daducci, Canales-Rodriguez, et al., 2015] or advances in machine-learning-driven tractography [Neher et al., 2015] could make improvement on the false positive rate.

Other approaches have proposed to compensate the lack of global information by adding them in the form of anatomical priors whose purpose would be to guide the algorithm in complex regions. As for segmentation and label fusion approach, recent methods are based on the use of an anatomical atlas such as the TRACULA method [Yendiki et al., 2011], with promising results combining deterministic tractography and anatomical prior. Then, diffusion priors during the tracking process were proposed in [Cook et al., 2008; Rheault et al., 2019; Yap et al., 2011], improving the delineation of white matter bundles. In [Rheault et al., 2019], a bundle-specific tractography (BST) method incorporates anatomical and orientational priors based on a template, to improve the reconstruction of long fibers and increase of reproducibility, sensitivity and specificity. On the other hand, in [Wasserthal et al., 2018b], another well-known approach based on a machine learning method was proposed to automatically segment, with high precision, the overall shape of a bundle, being a potentially great source of prior.

Based on these promising results, we developed a method of anatomical prior creation and combination, which is usable with any tractography algorithm based on orientation distribution function (ODF) [Descoteaux et al., 2007b]. Our method use pre-segmented fiber bundles by [Wasserthal et al., 2018b], to agglomerate global information from several different brains and capture the orientational variability in complex brain region. In this work, prior are computed on this anatomical atlas and expressed in the form of voxel-wise TOD [Dhollander et al., 2014] and then combined with the orientation distribution function (ODF) [Descoteaux et al., 2007b] data using a Riemannian framework [Goh et al., 2011]. We decided to incorporate those priors in two state-of-the-art algorithms using traditional ODF data, MRtrix iFOD2 [J. Tournier et al., 2010] and Trekker PTT

[D. Aydogan and Shi, 2021]. We then evaluated those methods on the diffusion-simulated connectivity (DiSCo) dataset [Rafael-Patino et al., 2021a] and on the Human Connectome project (HCP) [1] data to show the increase quality of the tractogram and more specifically on the spatial extent of the reconstructed bundles.

4.2 Method

Our method can be separated into 3 distinct parts: i) the construction of an anatomical atlas from segmented fibers, considered as gold standard, ii) the extraction and estimation of the TOD anatomical priors, from the atlas and iii) the combination between the priors and the subject data. The entire framework is illustrated in Figure 4.1.

4.2.1 Atlasing

The first step of our framework is the creation of a reference fiber atlas from a set of high-resolution diffusion images (see Figure 4.1.a). In this paper, we chose high-resolution diffusion images from the Human Connectome Project (HCP) young adult study [A. L. Alexander et al., 2007], which were acquired at high spatial resolution and b-values with 90 directions and thus contains high quality information on the fibers orientations.

The proposed atlasing method follows a modified version of Guimond et al (2000). [Guimond et al., 2000] which was adapted for diffusion data, to compute an atlas of Tensor images from a set of control subjects. This approach is based on a procedure which compute iteratively the atlas by registering the tensor images of HCP images onto a current reference. After each iteration, it performs an average of all the previous unbiased atlases to compute the next one at the following iteration. The main modifications from the original Guimond et al. (2000) method [Guimond et al., 2000] is to use diffeomorphisms encoded as Stable Vector Fields (SVF) and the log-Euclidean framework [Arsigny et al., 2006b] to compute the average transformations and the approach was adapted to diffusion data. The entire procedure is detailed in Suarez et al., 2012.

For each HCP data, 72 bundles were obtained by Wasserthal et al. (2018), using the TractSeg algorithm [Wasserthal et al., 2018b] which perform fiber tracking and fiber filtering, first by regions of interest (ROIs), then by an expert. The overall process used to segment these bundles is detailed in [Wasserthal et al., 2018b] and the data is available

1. https://www.humanconnectome.org/

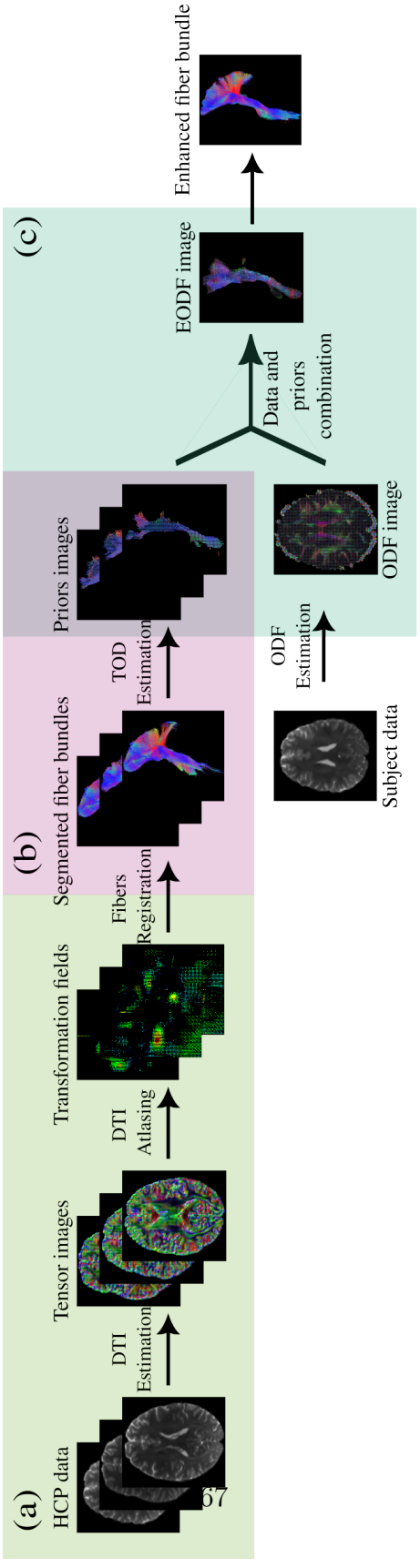

Figure 4.1 – Overall method pipeline. (a) Atlas creation. (b) TOD estimation. (c) Data and prior combination.

online [Wasserthal Jakob, 2018].

The transformation field obtained by the atlasing method from each individual space to the atlas space is then applied to 72 segmented fiber bundles of interest of each subject in order to all align them to the fiber atlas.

4.2.2 Track orientation distribution imaging

Once aligned to a common space, the bundles of interest are combined in order to represent the general shape of bundles. In order to capture complex orientation, a local fiber orientation prior was estimated using the track orientation distribution (TOD) [Dhollander et al., 2014], in each voxel. The tractogram is represented as a voxel-wise probability distribution function (PDF) in the image domain, rather than a set of individual tracks (samples from this distribution). The TOD, thus, captures the expected fiber directions [Dhollander et al., 2014].

Our TOD imaging method operates as follows : first, all the fibers directions of the voxel are extracted, then clustered using a k-means algorithm to define the main directions within the voxel and to correct for the density bias. This way, up to 4 principal directions can be extracted, allowing us to correct for the density bias as well as to characterize complex crossing regions. Then, the TOD in each voxel is represented using a set of modified spherical harmonics (SH) basis functions (see [Descoteaux et al., 2007b]) and constructed by projecting one spherical point spread function (PSF) per extracted main direction along the z direction.

The PSF, along the z direction at position ϵ, can be easily obtained in SH basis:

$$\delta_{z(\epsilon)}(\theta, \phi) = \sum_{l=0}^{\infty} \sum_{m=-l}^{l} c_l^m Y_l^m(\theta, \phi), \tag{4.1}$$

where $0 \leq \theta \leq \pi$ and $-\pi \leq \phi \leq \pi$ are the spherical coordinates, Y_l^m the spherical harmonic of degree l and order m and c_l^m, the coefficients, given as:

$$c_l^m = \int_{-\pi}^{\pi} \int_0^{\pi} \delta_{z(\epsilon)}(\theta, \phi) Y_l^m(\theta, \phi) d\theta d\phi \tag{4.2}$$

We found that resolving the equation 4.2 with the PSF pointing towards the direction $\theta = \frac{\pi}{2}$ and then rotating them to match the direction extracted from the atlas greatly simplifies the calculations. In Geng et al., 2009, authors showed a simple method to rotate functions expressed in SH basis. Since 4 different directions can be represented in a voxel,

the final step of the prior extraction is to average the projected PSF. The averaging of distributions defined on the sphere is performed through a Riemannian framework [Goh et al., 2011]. To do that, we define $\psi(\theta, \phi) = \sqrt{\delta_{z(\epsilon)}(\theta, \phi)}$, the square-root density function of the PDF $\delta(\theta, \phi)$. The square-root is used to ensure that the logarithm maps are available in closed form. Thus, $\delta(\theta, \phi)$ has to be strictly positive. For this reason, in order to find the right PSF, several different distributions were tested (i.e. a Dirac distribution, a Watson distribution and a Gaussian distribution) and then were expressed on the SH basis. We found out that a 2D Gaussian distribution on the unit sphere, is the only one whose number of negative values do not diverge with the degree l.

Then, in order to calculate the average distribution, we used the weighted Karcher mean, $\overline{\psi}$, of a set of n points $\{\psi_i\}_{i=0}^n$ in a Riemannian manifold defined by:

$$\overline{\psi} = \text{argmin} \frac{1}{2} \sum_{i=0}^{n} \omega_i \text{dist}(\psi, \psi_i)^2 \tag{4.3}$$

with $\omega_i \leq 0$ and $\sum_{i=0}^{n} \omega_i = 1$

As described in [Goh et al., 2011], the unique solution is $\overline{\psi}$, such as:

$$\sum_{i=0}^{n} \omega_i \log_{\overline{\psi}}(\psi_i) = 0 \tag{4.4}$$

where $\log_{\overline{\psi}}$ is the logarithm map from $\overline{\psi}$ to ψ_i, given by:

$$\log_{\overline{\psi}}(\psi_i) = \frac{\psi_i - \langle \psi_i, \overline{\psi} \rangle \overline{\psi}}{\sqrt{1 - \langle \psi_i, \overline{\psi} \rangle}} \cos^{-1} \langle \psi_i, \overline{\psi} \rangle \tag{4.5}$$

with $\langle ., . \rangle$, the normal dot product.

At the end of this step, using the equation 4.5 and $\omega_i = 1/n, \forall i \in \{1, ..., n\}$, we obtained $\overline{\psi}$, which is the square-root of the prior for each voxel. An example of the prior with the SH coefficients, truncated at a degree of $l = 8$, of the PSF described previously are shown in Figure 4.4. The prior creation process in order to average all extracted directions has to be calculated only once.

4.2.3 Riemannian framework

As displayed in Figure 4.1, the ODF image of the individual diffusion dataset is calculated to estimate the next direction. During tractography, in order to inform the ODF

with the anatomical prior, as previously explained in the previous section, a weighted Karcher mean is computed between the ODF and the prior using equation 4.4, to obtain the enhanced-odf (EODF). However, this method involves calculating, at each step of the tracking, the dot product between distribution on the sphere, that implies an integral over the sphere which would complicate the process. To simplify the computations, Goh et al. (2009) proposed to discretize the PDF and to work with the square root of histograms [Goh et al., 2011]. In this case, the dot product become summations.

Since the overall purpose of our method is only to guide the tractography algorithms and not to reflect the structure of the priors, the weighting factor ω_i must be well studied. We want to be able to distinguish between the simple linear region, where not much guidance is needed, especially in easier-to-track bundles with only one fiber direction, and the complex regions with crossing fibers, where the use of the prior is more needed. In order to address this specification, we choose to use 2 measures to weight the prior: the generalised fractional anisotropy (GFA), for the prior and the Akaike information criterion (AIC) [Akaike, 1998] for the data.

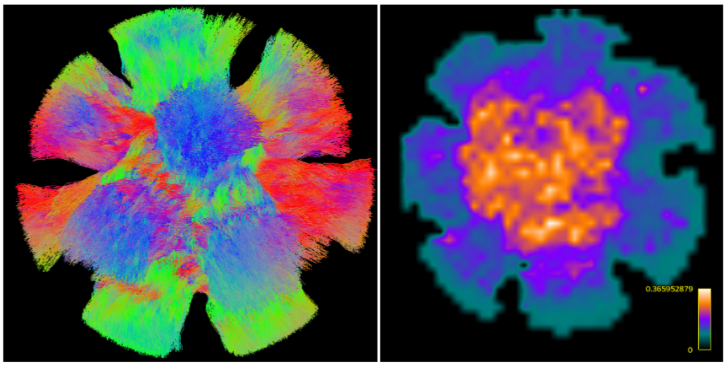

Figure 4.2 – Left: DiSCo dataset pathways. Right: Prior weighting map example for the DiSCo dataset. Higher value denotes higher usage of the prior and thus more complex regions.

The GFA, is given by:

$$GFA = \sqrt{\frac{1 - c_0^2}{\sum_{i=0}^{N} c_i^2}} \tag{4.6}$$

where the c_i are the SH coefficients. The GFA is a measure of the anisotropy within the considered voxel, that is, in the case of the prior, this value can reflect the complexity of a region.

The AIC, is described by;

$$AIC = 2k - 2\ln(L) \tag{4.7}$$

where k is the numbers of parameters in the model and L the maximized likelihood. The AIC is a measurement of the estimation quality of a model.

Empirically, to well differentiate linear and complex regions, we defined the prior weight given by:

$$\omega_{prior} = \alpha(1 - GFA) + \beta\exp(\frac{AIC_{min} - AIC}{2}) \tag{4.8}$$

where α represents the amount of information extracted from the priors, via the GFA, and β the amount of information extracted from the data, via the AIC. Those parameters needs to be adapted to the data. For the scenario presented in this work, we choose $\alpha = 0.35$ and $\beta = 0.65$ (see Figure 4.3).

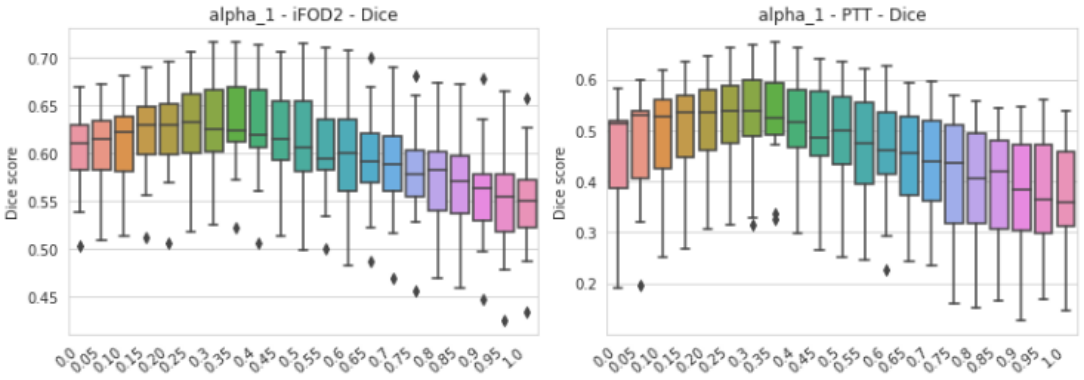

Figure 4.3 – Evolution of the Dice score versus α (from the Equation 4.8) for the tracking of the CST and for the iFOD and PTT algorithms. The method performs most effectively with an *alpha* value of 0.35.

An example of a weighting map for the DiSCo dataset can be seen on Figure 4.2 with higher ω_{prior} in crossing fiber areas.

The result of this averaging process is then an EODF, expressed in SH basis, usable in any ODF-based tractography algorithm. Figure 4.4 shows examples of data and priors combination, as well as the effect of weighting on the results. The first row represents a voxel where the ODF and the prior have the same direction, corresponding to an easy-to-track regions with one-way crossing. On the other hand, in the second and third rows, the orientation of the ODF and the prior are different. In this case, according to the value of ω_{prior}, the EODF is almost equal to the ODF or a mixture of the prior and ODF.

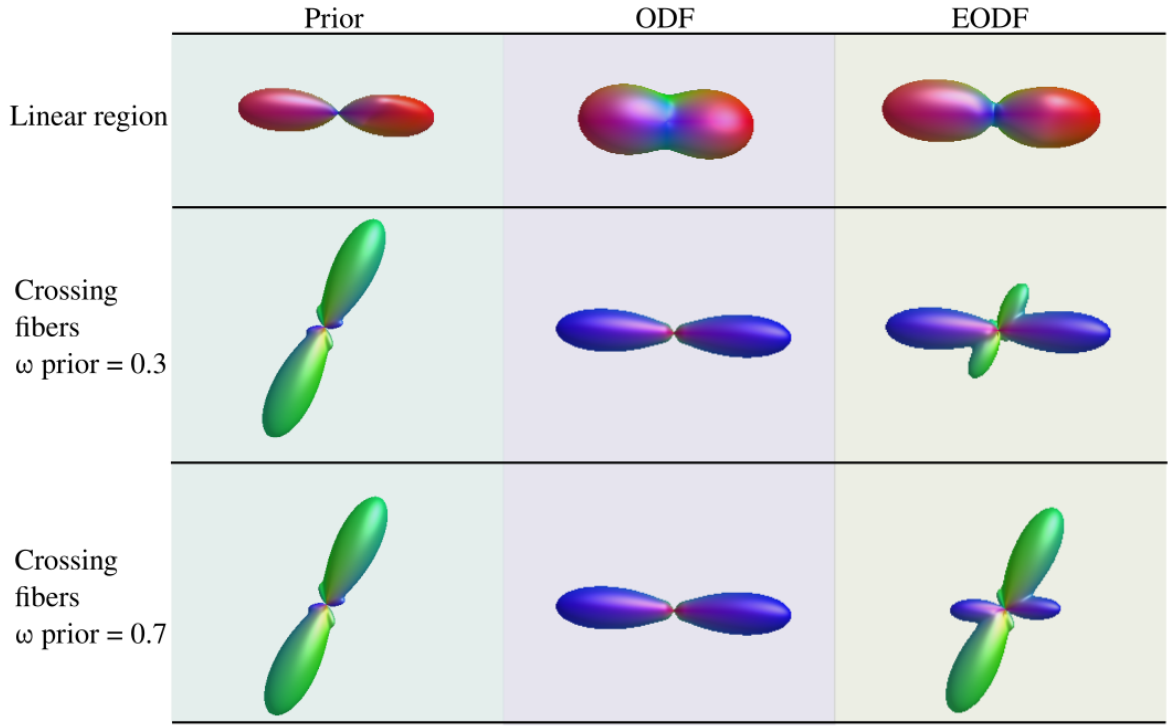

Figure 4.4 – Examples of data and prior combination. On the first row: prior and data are aligned. The EODF main orientations are unchanged. On the second and third rows: Prior and data are crossing. The corresponding EODF peak is more or less attenuated using the weight of the prior.

4.3 Experiments

In order to validate our method using priors, we conducted our first experiments on the DiSCo challenge dataset [Rafael-Patino et al., 2021b]. Then, we tested our algorithms on HCP data. For each experiment, we implemented our prior approach on two state-of-the-art algorithms, MRtrix iFOD2 [J. Tournier et al., 2010] and Trekker PTT [D. Aydogan and Shi, 2021]. Thus, on the two dataset, 4 tractography reconstruction were performed, both with and without using priors. For iFOD2, we used a step size of 0.2 voxel and a maximum angle between successive steps of 20 degrees. For PTT, we used the default parameters.

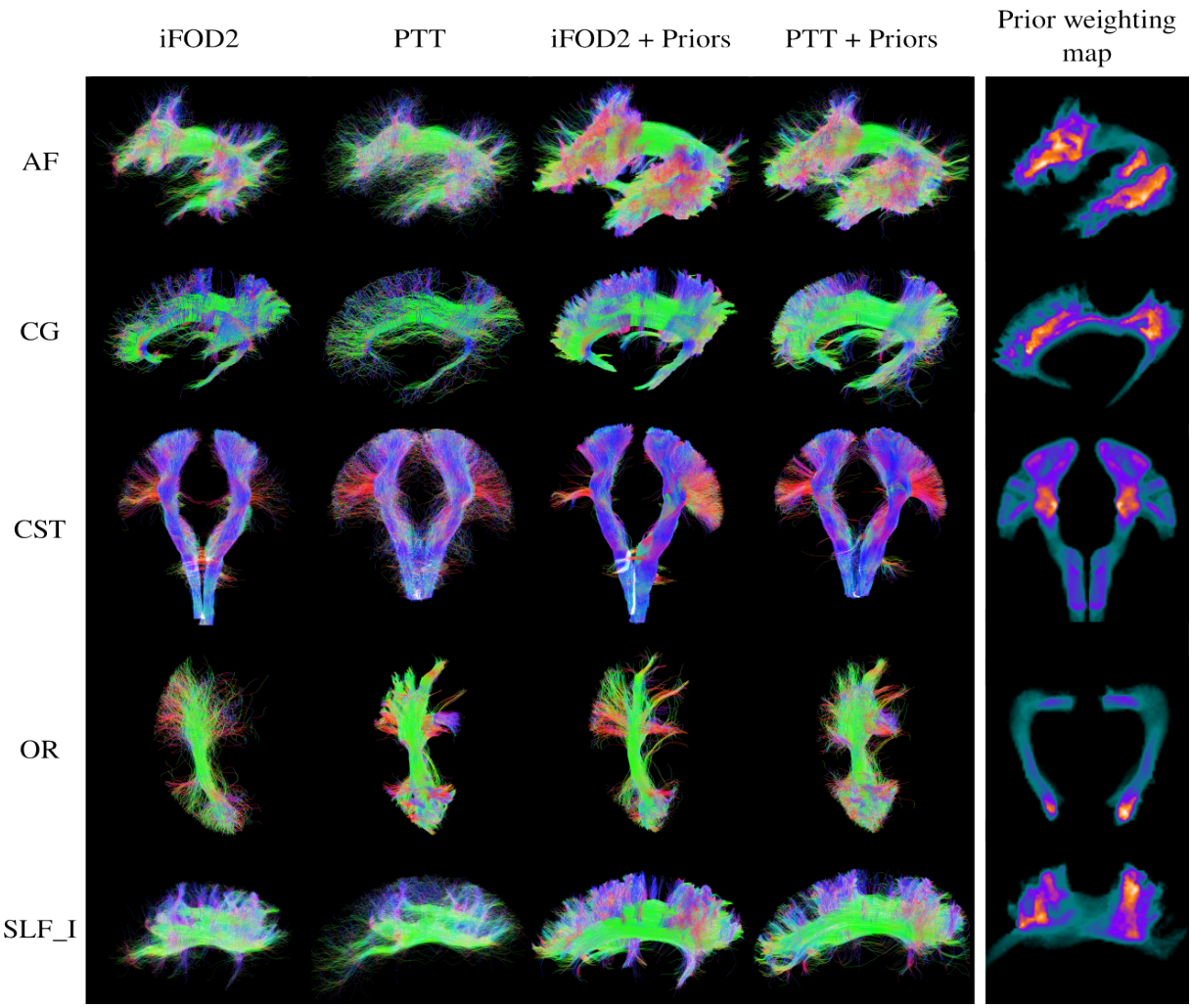

Figure 4.5 – Visual comparison of the resulting tractograms, with and without prior. From left to right, in column : iFOD2, PTT, iFOD2 with priors and PTT with priors. Last column on the right: Prior weighting map, where brighter pixel denotes a higher usage of the prior. From top to bottom : The Arcuate fascicle (AF), the Cingulum (CG), the Corticospinal tract (CST), the Optic radiation (OR) and the Superior longitudinal fascicle I (SLF I).

4.3.1 Simulated data

The aim of this experiment is to test the ability of our novel method to improve the connectivity estimation and the effect of noise. In this context, we do not have access to several datasets to build an anatomical atlas, instead, we computed the TOD: (i) using the ground-truth fiber pathways as anatomical priors and (ii) using fiber tracked on high

quality data as anatomical priors.

Data

We performed two different variants of this experiment: in the first one, priors are estimated on ground-truth fibers, not available on in vivo data; and the second experiment is used to demonstrate the benefit of our method, without having a ground-truth but priors build on high resolution data.

(i) Fiber pathways ground-truth: The DiSCo dMRI images have a grid of $40 \times 40 \times 40$ with voxel size of 1 mm^2 and are acquired with 4 different b-shell of 1000, 2000, 3000 and 1300 s/mm^2, 90 directions per b-shell and 4 b0. In order to obtain synthetic data with the same quality as those in clinical context, we used degraded data with a grid of $20 \times 20 \times 20$ voxels and only using the 3000 s/mm^2 b-shell with 60 directions. The prior is computed with the original data. In addition, to study the effect of noise, we added Rician noise on the dMRI. The resulting images have an average SNR of 0dB, 10dB, 20dB, 30dB, 40dB and 50dB. The individual ODF were computed using the method described in [Aganj et al., 2010] and represented in a spherical harmonic basis truncated at the 8^{th} order. Then, EODF were calculated using the method described in this paper.

(ii) multi-shell ODF: In this second set of experiment, we computed the priors on fibers tracked with the multi-shell multi-tissue constrained spherical deconvolution (CSD) fiber ODFs. The idea is to simulate a clinical context by computing the ODF on clinical dMRI data and combined with anatomical priors calculated on high resolution data. The anatomical prior are calculated on $40 \times 40 \times 40$ voxels DiSCo dMRI at SNR 20. From those images, fiber ODF were computed using the MRtrix implementation of the multi-shell multi-tissue constrained spherical (msmt-CSD) method described in [Jeurissen, Tournier, et al., 2014] using default parameters and using 8^{th} order SH basis. Then, fibers were tracked using the MRtrix iFOD2 algorithm with a step size of 0.2 voxel and default parameters. Only the streamlines that reach the endings ROIs were kept. Finally, the TODs were extracted from those fibers using the method detailed in the previous section. After prior estimation on high resolution data, we estimated the ODF of a subject data with $20 \times 20 \times 20$ grid and SNR= 20. Then, EODFs were obtained by combining the TOD with the clinical data fiber ODF.

Metrics

To quantify the results, we computed the Pearson correlation coefficient (r) between the ground truth connectivity matrices of the three DiSCo dataset and the resulting tractograms connectivity matrix. These matrices are computed by counting the numbers of streamlines that reach both start and end ROIs for each DiSCo fibers bundles.

4.3.2 HCP data

Data

To test our method on in vivo high quality data, we used the HCP young adult data, acquired with 90 gradients distributed on 3 shells of b=1000, 2000, and 3000 s/mm^2 with 6 b= 0 acquisitions and a final resolution of 1.25mm^3. Among them, the 105 pre-segmented HCP images were used, as described in 4.2.1, to build fiber atlases of the Arcuate fascicle (AF), the Cingulum left (CG), the Corticospinal tract (CST), the Optic radiation (OR) and the Superior longitudinal fascicle I (SLF I) to study the influence of the addition of prior on bundles of different degrees of complexity and in different region of the brain. A cross validation was performed on the 105 subjects in which 100 subjects are used to build the atlas and the 5 remaining to perform the tractography algorithm. This process is repeated 8 times, giving us a total of 40 subjects to test the method on. For each image belonging to training set, ODFs were computed on the shell b= 3000 s/mm^2 using the method described in Aganj et al., 2010 and represented in a spherical harmonic basis truncated at the 8^{th} order. Then, the TOD images for each bundle were registered on the subject space. Those priors were incorporating during the tracking process for each subject. The tractography algorithms were tested on the 5 remaining subjects.

In order to compare our method with state of the art anatomical priors methods, we used the BST algorithm ([Rheault et al., 2019], using the default parameters, to compute enhanced ODF for the CST and the AF bundles. We then tracked those bundles with the iFOD2 and PTT algorithms using the same parameters as before.

Metrics

To quantify the overall shape quality of the tractograms, we computed the generalized Dice score Crum et al., 2006b between the segmentation of fibers obtained with tractography algorithm and the reference fibers. In order to measure the improvement on

the numbers of streamlines reaching both ROI endpoints, we computed the percentage of streamlines that correctly connects the beginning and the end regions of bundles over the total number of streamlines in the reference bundle (noted valid streamlines VS). It is worth noting that this measure does not mean anything in absolute, being biased by the numbers of streamlines in the reference tracks. However, since the same numbers of streamlines is generated for each bundle, it allows us to compare the overall bundles shape and quality with and without the addition of priors.

4.4 Results

4.4.1 DiSCo challenge dataset

Figure 4.6 displays the correlation with the ground-truth connectivity of the two experiments, for the three DiSCo dataset. First, on Figure 4.6.a, we observed that lower the noise is, better are the correlation improvement for the experiment using the fiber pathways as ground-truth. Next, both algorithms performed better with the addition of priors for all level of noise and the three datasets. We can also notice that the improvement decreases when the quality of the data increases. In average, the correlation increases of 0.23 for an SNR of 10 dB but only 0.11 for an SNR of 50 dB. Moreover, the mean correlation improvement is of 0.19 and 0.17 for the iFOD2 and PTT algorithms, respectively. At last, the average maximum reached is $r = 0.83$ for PTT and $r = 0.82$ for iFOD2. There are no major differences between the three dataset. For the second experiment using high resolution DW-MRI data, we showed an average correlation improvement of 0.15 for the PTT algorithm and 0.17 for the iFOD2 algorithm, in figure 4.6.b. Incorporating anatomical priors calculating on high resolution data during the tracking process of low resolution data increases the Pearson correlation coefficient with the ground-truth connectivity matrix.

4.4.2 HCP data

Figure 4.5 displays the segmentation of AF, CG, CST, OR and SLF I obtained with iFOD2 and PTT, with and without prior. The results for the Valid streamlines and the Dice score are presented in Figure 4.7. For the VS score, the addition of priors appears to always increase, on average, the numbers of streamlines that connect both end regions. However, enhanced tractography seems to also increase the variability of the results, as

we found a mean variance across all bundles of 7.19% without the prior and 19.84% with. We also noticed that incorporating the priors in the PTT algorithm improve more the VS than with the iFOD2 algorithm. Indeed, the average gain for iFOD2 is of 25.08% and 31.37% for PTT. The same observation can be made for the dice measurement, but as opposed to the Valid streamlines measurement, the variability seems to be decreased with the addition of prior. We notice that incorporating the anatomical priors improve the spatial coverage and that a higher fraction of streamline reach the endpoints of the bundle.

The Figure 4.8 present the Dice score and the number of valid streamlines for the AF and CST bundles, tracked with iFOD2 and PTT without the addition of priors, with prior computed with our method and with prior computed with the BST method [Rheault et al., 2019]. It shows that, on average, our method demonstrates superior performance compared to the BST algorithm, both in terms of spatial overlap and the number of valid streamlines.

4.5 Discussions

In this work, we proposed a novel method for creating and incorporating anatomical priors to any ODF-based tractography algorithms. We showed that incorporating anatomical priors on two state-of-the-art tractography algorithms improve the overall quality of tractograms when priors are extracted from a ground truth, but also from high quality tractograms. Indeed, first, on the DiSCo dataset, the proposed prior-based tractography methods obtained better correlation scores between the reconstructed bundles and the ground truth for every level of noise than the standards probabilistic algorithms, but this improvement decreases with the increasing SNR. Thus, the addition of priors to ODF images improve the quality of tractograms in presence of noise. However, due to the actual form of the extracted TOD it may not be useful on high SNR data. More particularly, in the DISCO experiment, we tried to mimic real clinical context with low spacial resolution data and an SNR of 20. In this case, our results showed a better correlation for two methods incorporating priors between the estimated fiber and the ground-truth, reducing false positive fibers. This could allow us to consider using this method on clinical data of average quality, informed by prior extracted on high quality data. On the HCP data, the same results were obtained with an increase of the fraction of valid streamlines numbers when anatomical priors were incorporating during tracking process. In the same time,

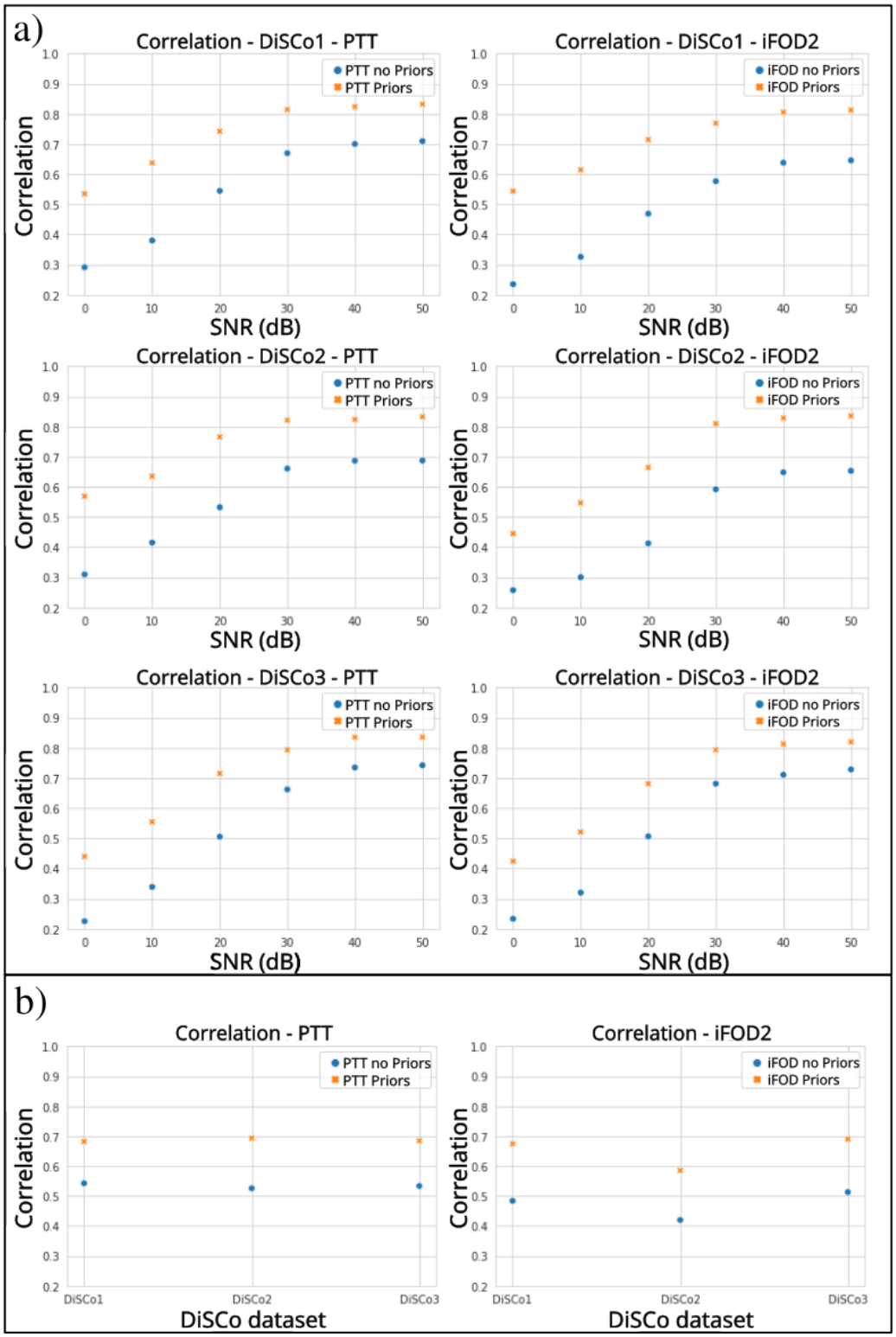

Figure 4.6 – Pearson correlation for the DiSCo experiments: (a) Fiber pathways ground-truth experiment with respect to SNR (b) Multi-Shell ODF experiment for the 3 DiSCo dataset. First column for PTT and second for iFOD2. In all cases, blue points denotes measure without prior and the oranges ones, with prior.

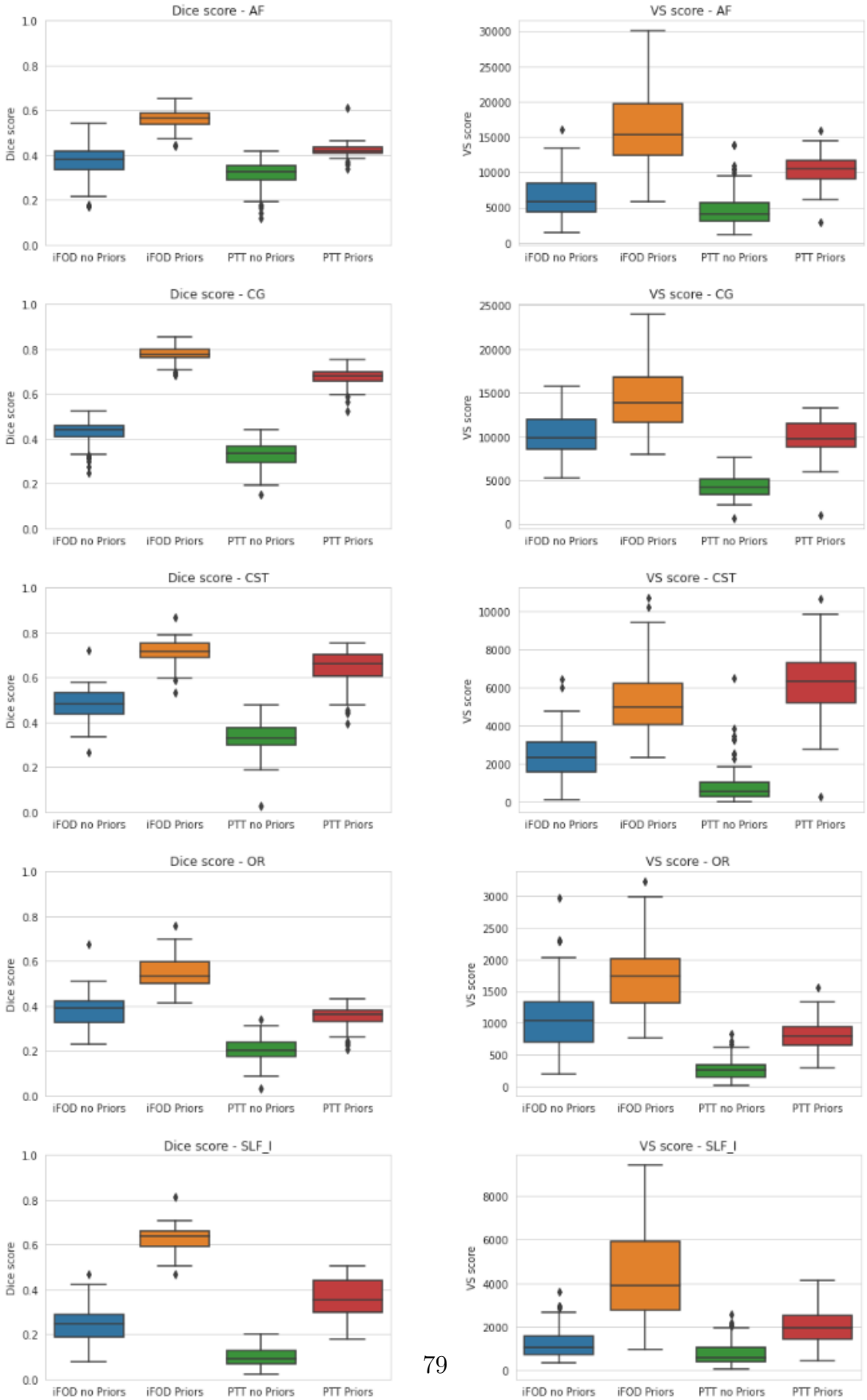

Figure 4.7 – On the left, Dice score result for the HCP experiment. On the right, VS number result for the HCP experiment. From top to bottom : AF, CG, CST, OR, SLF I

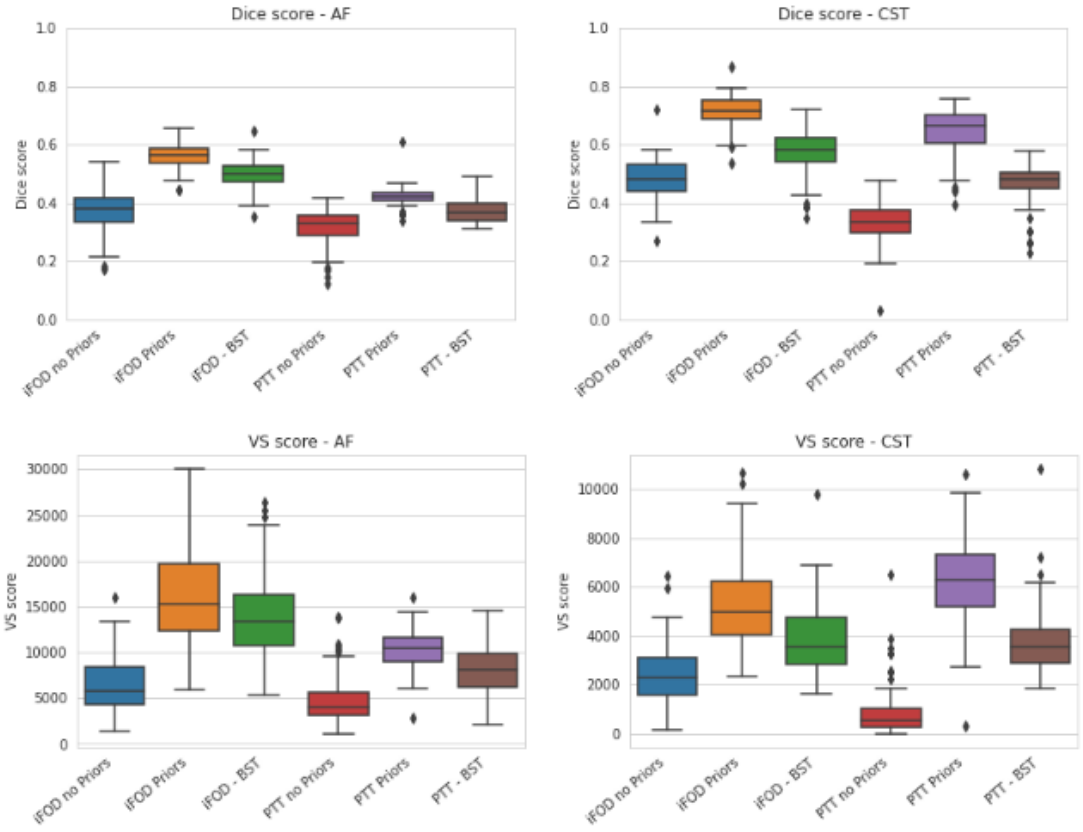

Figure 4.8 – Comparison with the BST algorithm

due to the increase of the dice score when adding prior, the overall shape of the bundle seems to be also modified. We also reported an increase in variability across subjects of the tractography with priors compared with the ones without priors.

The effect of the priors seems to be more effective in complex fibers configurations, like fanning and crossing fibers or in large curvature radius. Indeed, our method is able to a better delineation and estimation of precise details. For the CST, it is well known that the upper part, that fans into the cortex, is hard to estimate. Without prior, the iFOD2 and PTT algorithms only manage to estimate a portion of the CST. While, with the addition of anatomical prior, they achieve a more complete reconstruction of the fanning portion. Another example is the OR bundle, where the Meyer's loop, with its highly curving fibers, is still a tractography open challenge [Bertani et al., 2018]. When guided by EODF, both tested algorithms show results that, while containing spurious streamlines, allow a better recovery of the anterior extent of the Meyer's loop. This result can be easily explained by the fact that in regions with crossing fibers, more information is taken from the prior. See the right column in Fig. 4.5 where the brightest regions correspond to the most complex fibers micro structure regions and denotes a higher usage of the prior.

It is important to note that the results presented in this paper use iFOD2 and PTT algorithms as proof of concept, but the main idea behind this work is to develop a method to improve the spatial coverage and the numbers of streamline reaching the endpoints of the bundle of any ODF-based tractography algorithm. In fact, future works should study the contribution of prior addition with other algorithm but also generalize this method to other diffusion model.

In [Rheault et al., 2019], authors generated sharp TOD by projecting Dirac in the SH basis. However, our experiences have shown that this also generate a number of negative values which increase with the truncated SH basis order, due to the Gibbs phenomenon. Thus, to overpass this problem and remove the negative values, they use apodized delta function [Raffelt, Tournier, et al., 2012] proposed in [Dhollander et al., 2014], but at the cost of a loss of angular resolution. Using this PSF, we would have to truncated at a higher order the TOD SH basis to obtain the same angular resolution that we have with the 8^{th} order of the Gaussian PSF [Dhollander et al., 2014]. So we decided to keep the Gaussian PDF and the ODF estimated without CSD, at the expense of less sharp ODF peaks, our interest here being to compare the tracking connectivity with and without prior. In the same way, in [Rheault et al., 2019], priors and data are combined by an element-wise multiplication between the two sets of SH coefficients, followed by a normalization.

However, our approach (i.e. using a Riemannian framework), allows us a better control over the weighting between the TOD and ODF and minimizes the potential angular smoothing. It also enables, for future works, more complex operation on TOD, such as interpolation between different set of priors or even TOD filtering to remove unnecessary information, in order to improve the prior quality, at the cost of more approximation during the TOD estimation and an increased complexity.

Other works that studies the idea of guiding tractography algorithms, like [Yendiki et al., 2011, Cook et al., 2008, Yap et al., 2011 or Rheault et al., 2019], use non-linear registration and atlasing techniques during the atlas, or template, creation process, preferring to do an average of the references images. This could smooth the variability across the atlas and could also be the source of errors that would be accumulated in the final atlas and would, in the end, inject a bias inherent to the atlas in the tractography process. In our approach, using a modified Guimond method [Guimond et al., 2000], the references image are, at each step, iteratively registered with a non-rigid transformation onto the current space that become the reference space in the next step ant it is only the average of the transformation that is computed at the end of each step. With this approach, all the variability information is accumulated in the atlas and the errors are not included in the final atlas. Thus, no bias is introduced in the tractography.

Also, using pre-segmented fibers to build the atlas may not be appropriate in order to study the global connectivity of the brain, as this approach only allows the enhanced tracking to be performed within a unique bundle. But, although not showed here, our method also allows, by concatenating the individual bundles priors, the construction of full brain atlases, and thus enable guidance of whole brain tracking. Therefore, it could be used for clinical studies where priors would be constructed from high resolution dMRI data in order to guide tractography algorithm on poor, clinical, resolution data.

Finally, our method has proved to be able to increase the quality of the estimated fibers, in term of spatial extant and number of valid connection when utilized on healthy subjects. These promising results could already enable advances in an academic context for the study of the healthy brain. In a more clinical context, if used on patients suffering from pathologies that only slightly or moderately modify the white matter, such as psychiatric pathologies, this method could also bring improvements in fiber estimation, perhaps through a more in-depth study of α and β parameters. Research along these lines should be pursued in future work. However, when working on patient suffering from severe brain alteration, such as strokes, this method could produce a tractogram solely guided by the

prior in the affected region, thus removing the specific microstructural modification and therefore may not be the most appropriate approach. In such scenarios, a solution might be to import other types of information into the priors. Either in the way the data and priors are weighted, using for example Apparent fiber density [Raffelt, Tournier, et al., 2012] of the data to potentially detect these brain modifications and thus prevent the fibers from being tracked solely on the priors, or directly in the estimation of the priors using other imaging modalities, such as myelin-sensitive relaxometry in order to obtain priors images describing these brain regions in greater detail.

4.6 Conclusion and prospects

In this chapter, we developed a method of anatomical prior creation and combination, which is usable with any ODF-based tractography algorithm. The priors are computed on fiber atlases and expresses in the form of TOD, in order to characterize the brain variability and multiple fiber directions. Then, our prior is incorporated to guide the ODF-based tractography algorithm. Based on our results on DISCO and HCP data, incorporating our anatomical priors improve the fibers reconstruction, in terms of spatial extent and valid streamlines, especially in crossing fiber regions. Furthermore, we have shown that our method outperforms previous methods using anatomical priors in the tracking of the CST and the AF. Moreover, our approach could also greatly enhance the tractography in the context of clinical data, by incorporating priors estimated on high quality data, which could help for the study of neurological diseases.

Chapter 5

White matter microstructure changes along the fiber in treatment resistant depression

5.1 Introduction

Depression, also known as Major Depressive Disorder (MDD), is a prevalent condition that significantly impairs one's ability to engage in social and psychological aspects of life, resulting in a notable reduction in overall well-being. In 2008, the World Health Organization (WHO) identified it as the third leading contributor to the global disease burden and has predicted that it will ascend to the top position by 2030 [Bains and Abdijadid, 2020]. Despite its high prevalence, depression is often underdiagnosed, especially in low- and middle-income countries. Studies report varying rates of underdiagnosis, ranging from 8.5% to over 50% [Faisal-Cury et al., 2022]. In terms of neurobiology, depression is marked by a profound and enduring disruption of emotions and mood [Freedman et al., 2013]. This disruption is often accompanied by other disturbances such as cognitive impairment, sleep problems, fatigue, and changes in appetite [Drevets, 2001]. Consequently, delving into the neural underpinnings of depression and exploring its various manifestations will enhance the ability to diagnose and treat individual patients suffering from depression more effectively

Furthermore, MDD stands as a global primary contributor to disability, primarily because of its propensity for recurrence and resistance to treatment [« Global, regional, and national burden of 12 mental disorders in 204 countries and territories, 1990–2019: a systematic analysis for the Global Burden of Disease Study 2019 », 2022; Herrman et al., 2022]. The Sequenced Treatment Alternatives to Relieve Depression (STAR*D) trial illustrates this challenge, revealing that 30% of patients continued to experience depression even after undergoing four rounds of antidepressant (ATD) trials [Rush et al.,

2006]. Notably, the likelihood of achieving remission saw a significant decline following the second ATD trial. Over the past two decades, there has been a growing focus on conducting research into biomarkers that could potentially aid in identifying individuals at risk of Treatment Resistant Depression (TRD) and provide guidance for therapeutic approaches [Kennis et al., 2019; Wager and Woo, 2017].

Among the risk factors favoring TRD, it has been suggested that it may be associated with a decrease in gray matter volume in various cortical brain regions and a compromised structural integrity in white matter [Grehl et al., 2023]. Additionally, in comparison with patients in remission, those with TRD exhibit notable changes in functional connectivity within the affective network, the salience network, and the cognitive control network [Sun et al., 2022]. These alterations in connectivity patterns may potentially contribute to the neurobiological distinctions that set TRD apart from non-TRD cases. Finally, research has indicated that it may be associated with particular microstructural white matter abnormalities, such as those found in the sub-callosal cingulate cortex (SCC) [Serafini et al., 2015], as well as in the prefrontal cortex (PFC).

While diffusion MRI and white matter tractography have enabled major advances in the study of cerebral fibers, the diffusion models have provided new metrics for characterizing white matter microstructure. The classical approaches, which rely on DTI [P. J. Basser et al., 1994a], involve metrics like fractional anisotropy (FA), radial diffusivity (RD), and mean diffusivity (MD) [P. J. Basser and Pierpaoli, 1996]. These metrics have been widely employed to study white matter in various conditions, both normal and pathological. However, their interpretation proved difficult due to their susceptibility to being influenced by several confounding factors. These include parameters such as axon diameter, axon spacing, membrane permeability, myelination and particularly complex fiber structures [Beaulieu, 2002; Wheeler-Kingshott and Cercignani, 2009]. As explained in Chapter 2, the advent of advanced multi-shell MRI sequence [D. S. Tuch et al., 2002] has resulted in more sophisticated techniques for enhanced characterization of intricate white matter regions that were previously challenging to describe. Such multi-fiber models, like the ODF [J.-D. Tournier et al., 2004], the CHARMED model [Assaf and Basser, 2005] or the NODDI model [H. Zhang et al., 2012b], have enabled the extraction of novel parameters from both intra- and extracellular compartments. They have also allowed the estimation of microstructure metrics, such as axon diameter distributions, offering a more comprehensive understanding of complex white matter structures. Futhermore, new frameworks like the fixel-based analysis [Raffelt, Tournier, et al., 2012], allow the

mapping of fiber-specific measures using apparent fiber density (AFD), which reflects the underlying fiber density.

In parallel, a novel framework called tractometry or tract profiling has emerged, enabling a more comprehensive evaluation of white matter microstructure. The tractometry offers the advantage of increased sensitivity to the microstructural characteristics of fiber pathways by mapping a range of diffusion metrics across white matter bundles [Colby et al., 2012; Yeatman et al., 2012]. Rather than summarizing the entire pathway using a single scalar value, tract profiling enables statistical analysis to highlight group differences at specific locations along the pathway [Cousineau et al., 2017; Jones et al., 2005]. It also provides the capacity for conducting principal component analysis to delve into the complementary aspects of each metric, increasing their interpratibility [Chamberland et al., 2019]. This approach has proved effective in a range of research applications, including studies of normal brain development [Geeraert et al., 2017]. Additionally, it has demonstrated its utility in the study of various pathologies, including Parkinson's disease [Cousineau et al., 2017], Multiple Sclerosis [Beaudoin et al., 2021] or depression [Metin and Gökçay, 2021].

In this chapter, we propose to analyse group differences between a cohort of patients affected by treatment-resistant depression and an other non resistant to treatment using a tractometry approach. We employed metrics based on (ODF) to characterize the diffusion microstructure along fiber bundles connecting regions affected by pathology in TRD. To enhance our analysis, we conducted statistical assessments coupled with a Principal Component Analysis. This allowed us to mitigate redundancy among sensitivities and refine the discriminative power of our analysis. In addition, we also propose to study the influence of the addition of anatomical priors on the potential group differences, using the method described in the previous chapter.

5.2 Methods

5.2.1 The LONGIDEP cohort

Participants

A total of 179 individuals with depression were selected from standard care facilities at the psychiatric university hospital of Rennes between November 2014 and February 2023 and included in an observational prospective cohort investigation. The study was approved

	Resistant group (n = 40)			Non-Resistant group (n = 41)		
	Mean	SD	Range	Mean	SD	Range
Sociodemographic variables						
Age (years)	58,9	11,6	18 - 87	49,1	11,2	20 - 82
Gender (M/F)	10 / 30			14 / 27		
Duration of illness (years)	20,7	16,9	0 - 60	14,9	9,4	0 - 37
Number of episodes	4,25	2,23	1 - 10	5,75	4,3	0 - 30
Duration of episode (weeks)	35,5	35,4	0 - 288	48,5	39,9	1 - 200
Number of suicidal attempts	3,8	2,5	1 - 10	2,7	1,64	1 - 10
Clinical variables						
MADRS	26	4,4	15 - 38	27,48	4,35	17 - 43
STAI-YA	56,1	10,2	28 - 74	59,25	9,075	37 - 78
SHAPS	4,76	3	0 - 14	6,1	3,5	0 - 14
AES	41,9	7,1	29 - 60	45,2	8,6	24 - 69
YMRS	2,1	1,7	0 - 15	1,5	1,2	0 - 6

Table 5.1 – Demographic and clinical data for R and NR groups.

by an ethic committee and is registered in www.clinicaltrial.gov (NCT02286024), written informed consents were obtained from all subjects. The study was proposed to patients suffering from a Mood Depressive Episode (MDE) under DSM-5 criteria with or without personal history of MDD.

Patients with depression participated in a comprehensive assessment, which encompassed clinical interviews, examinations, standard neuropsychological evaluations, and MRI scans. Demographic information, comorbidities, medication details, and clinical parameters were documented for each participant. We evaluated the medication burden for each patient by employing a well-established method, which considered both the number of medication classes prescribed to patients and the respective dosages.

At 6 months follow-up 81 patients underwent a second structured clinical interview. This resulting cohort was separated into 2 groups (resistant or non-resistant to treatment) based on their Montgomery and Åsberg Depression Rating Scale (MADRS)[Montgomery and Asberg, 1979] score evolution over the 6 months. A decrease of at least -50% of the MADRS score was required for a patient to be considered as nonresistant. Ultimately, the resistant group (R) was composed of 40 patients and 41 for the Non-Resistant group (NR) (see Table 5.1 for the details).

Clinical assessment

Patients were assessed by two structured clinical interviews by a trained psychiatrist, one at $M0$ and another 6 months later. Anxious comorbidities were retrieved using the Mini-International Neuropsychiatric Interview Lecrubier et al., 1997]. Depression severity was assessed using MADRS. Manic symptoms were retrieved using the Young Mania Rating Scale (YMRS) [Young et al., 1978]. Additionally, the Widlöcher Depressive Retardation Scale (WDRS) [Widlöcher, 1983] was used to estimate psycho- motor retardation. State anxiety was measured using State Trait Anxiety Inventory A (STAI-YA) [Spielberger et al., 1970]. Then, the anhedonia and apathy scores were assessed by Snaith Hamilton Pleasure Scale (SHAPS) [Snaith et al., 1995] and Apathy Evaluation Scale (AES) [Marin et al., 1991], respectively.

MRI acquisition

All patients were scanned on a 3 T whole body Siemens MR scanner (Magnetom Verio, Siemens Healthcare, Erlangen, Germany) with a 32-channel head coil. The 3D T1-weighted image was acquired covering the whole brain (176 sagittal slices) with TR = 1.9 s, TE = 2.26 ms, flip angle = 9°, in-plane resolution = 2 mm × 2 mm, FOV = 256 mm × 256 mm and thickness/gap = 1.0/0 mm.

DWI data were gathered on 60 slices using an interleaved slice acquisition, slice thickness of $2mm$, no gap, in-plane resolution = 1 mm × 1 mm and in a 256 mm × 256 mm field of view. The acquisition matrix was 128 × 128, the reconstruction matrix was 128 × 128, using 30 directions and a b-value of 1000 s/mm^2. TR/TE = $11,000$/99 ms, flip angle was 90°, pixel bandwidth was 1698 Hz, and the imaging frequency was 128 MHz.

5.2.2 Image processing

Diffusion images preprocessing

Preprocessing of diffusion images was mainly performed using the open source medical image processing toolbox Anima (https://github.com/Inria-Visages/Anima-Public/wiki). Correction for eddy current-induced image distortion in diffusion images was carried out using a block-matching distortion correction method, which ensured a symmetrical transformation in the opposite direction [Hedouin et al., 2017]. Next, a rigid realignment process was perfomed to correct for subject motion and establish voxel-to-voxel correspon-

dence across gradients. Following that, denoising was carried out using blockwise non-local means filtering [Coupé et al., (2008)]. Skull extraction was then achieved through an atlas registration approach. Specifically, the structural image for each patient underwent a transformation to align with the atlas image, employing both linear and non-linear block-matching algorithms [Commowick et al., 2012a; Ourselin et al., 2000]. Afterward, the intracranial brain mask of the atlas was transformed in the opposite direction, achieved by applying the inverse of two calculated transformation matrices, and was subsequently combined with the patient's original structural brain image. The ODF were ultimately estimated using the constrained spherical deconvolution method [Tournier, 2014].

Tractography

Two sets of tractograms were then generated, both using the iFOD2 algorithm with a step size of 0.2 voxels and a maximum angle between two consecutive segments of 20°. For each patients, 1000000 streamlines were tracked using a whole-brain seeding approach. The first set of tractogram was processed directly from the ODF extracted from the patients DW images. For the second one, anatomical priors, extracted from an high-quality fibers atlas, were combined to the ODF data before performing the tractography (see the previous chapter for more details about the method). These whole-brain tractograms were then filtered using the terminating points ROI masks, segmented thanks to the TractSeg algorithm [Wasserthal, 2018], to retrieve the fiber bundles of interest. Based on previous studies focusing on apathy and LLD [Kim, 2021; Wen, 2014; Le Heron, 2018], only 29 bundles of interest were selected: The Corpus callosum (Rostrum (CC 1), Genu (CC 2), Posterior midbody (CC 5), Isthmus (CC 6) and Splenium (CC 7)), the Cingulum (CG), the Superior longitudinal fascicle (in 3 parts: SLF I, SLF II, SLF III), the Inferior longitudinal fascicle (ILF), the Corticospinal tract (CST), the Uncinate fascicle (UF), the Fronto-pontine tract (FPT), the Anterior Thalamic Radiation (ATR), the Superior Thalamic Radiation (STR), the Thalamo-premotor (T PREM) and the Striato-premotor (ST PREM).

Diffusion microstructure metrics

Next, several diffusion microstructure metrics were extracted from the ODF:

The Generalized Fractional Anisotropy (GFA) witch is a extension of the FA

and is defined by:

$$GFA = \sqrt{\frac{n\sum_{i=1}^{n}(\Psi(u_i) - \langle\Psi\rangle)^2}{(n-1)\sum_{i=1}^{n}\Psi(u_i)^2}} \tag{5.1}$$

where Ψ is the ODF and $\langle\Psi\rangle = \frac{1}{n}\sum_{i=1}^{n}\Psi(u_i)$ is the mean of the ODF. GFA provides the same information as the FA but offering the advantage of being able to take into account more intricate diffusion profiles and can provides information about the "sharpness" of the ODF lobes.

The Apparent Fibre Density (AFD) is an estimation of the fiber density for a given orientation. It is based on the assumption the total radial diffusion weighted (DW) signal is approximately proportional to the density of the fibres (i.e. the space occupied by the fibers). And since the ODF amplitude is also proportional to the radial DW signal for the given direction, it offers a proportional assessment of the volume within the axon that is filled by fibers oriented in the specified direction [Raffelt, Tournier, et al., 2012]. In this work, we computed the average of the AFD within each voxel as the sum of each AFD for each ODF lobes directions, followed by a normalization.

The fibers dispersion (DISP) within the voxel is the ratio between the ODF lobe integral and maximal peak amplitude.

The Number of fiber orientation (NuFo) refers to the number of distinct fiber orientations within each voxel. It provides information about the complexity of white matter organization. This mesaure is estimated by counting the number of local maxima of the ODF profile in each voxel and then filtering them to remove the local maxima due to noise and isotropic tissue [Dell'Acqua et al., 2013].

The Peak length (PL) is similar to the AFD but only the peak length which is the most similar to the direction of the bundle at that voxel is analysed. This metric is thus bundle-specific.

Note that for the AFD, DISP and PL metrics, ODFs need to be normalized across all subjects in order to be able to compare them with each other.

5.2.3 Tractometry analysis

In order to be able to find significant group differences, the projection of the 5 microstructure metrics on the tract profiling was performed for each bundle and each subjects using tractometry methods [Cousineau et al., 2017; Chandio et al., 2020]. We then carried out a comparative statistical analysis on these tract profiles.

Extraction of center line

Tractometry method assume that all streamlines and metric map are registered in a common space. It proceed, for each fibers bundles of each subject independently, as follow [Chandio et al., 2020]: First, the outlier are discarded based on their low density and and their shape distance from other streamlines within the fascicle. All streamlines are then resampled into an equal number of segments and inverted so they all share the same begin and end points. Next the bundles are clustered using the QuickBundles algorithm [Garyfallidis et al., 2012], resulting a centroid line, representing the overall shape of the bundle, with 30 points per cluster. Following this, the bundles are divided into the same numbers of segment as in the centroid line by computing the Euclidean distances between each point along every streamline within the bundle and all points of the clustered bundles. Then, each segment is assigned to the closest segment centroid. Finally, the five diffusion metrics are mapped onto the central line, creating a tract profile that illustrates how these metrics change along the fiber pathways. This profile enables the comparison of multiple groups, aiming to uncover any potential noteworthy variations.

Statistics along the fibers

All the analysis described in this section were performed once for two tractograms estimated by the iFOD2 algorithm with and without the addition of prior.

First, we ran an analysis correlation analysis among the five microstructure metrics with the objective of removing the correlation coefficients exceeding 0.9 to ensure the reliability of the subsequent analysis. Then we conducted a point-wise two-samples Student's t-test between the tract profiles of the resistant and non-resistant groups for each 29 bundles and each 5 metrics (GFA, AFD, NuFo, Disp, PL). The results were corrected for multiple comparison with a nonparametric permutation method [Nichols and Holmes, 2002]. In this approach, the dataset underwent 10,000 permutations by randomizing subject labels to compute metric differences between shuffled groups. This process constructed a distribution of differences under the null hypothesis, yielding insights into the family-wise error rate (FWE)-corrected cluster size. Clusters equal to or larger than this threshold exceeded the multiple comparison threshold, eliminating the need for additional p-value adjustments. Next, In order to mitigate potential redundancy while simultaneously delving into the distinct complementary aspects of each measure, a principal component analysis (PCA) was carried out individually for each bundle profile. PCA di-

minishes data dimensionality by extracting principal components that capture significant characteristics inherent in the data [Jolliffe and Cadima, 2016]. Without the addition of prior, only were kept the first principal component (PC), which explain 90% of the variance present in the data set, highlighting their importance in capturing the underlying information in the data. With the prior, we have kept the first two PC, which explain 96% of the total variance. We then conducted a second two-samples Student's t-test between the PCs of the two groups for each bundles. For the both Student tests, the influence of the age, the gender and the medication load of the patients were removed by performing a linear regression before the analysis.

5.3 Results

5.3.1 Tracts profiling

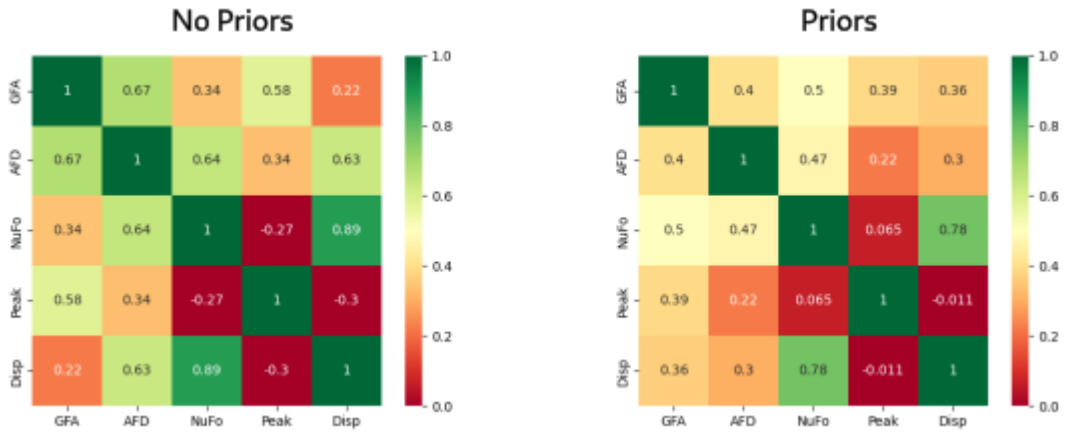

Figure 5.1 – Average correlation between the 5 metrics

As described in the previous section, for both tractograms obtained with and without 'Prior' (i.e. with the addition of anatomical priors), the 5 metrics were projected on the central line of each bundle. The Figure 5.1 displays the correlation analysis result averaged over all the bundles and the Figure 5.2 presents an example of a tract profile, averaged over all the subjects, on the Splenium (CC 7). First of all, we can note a decrease in the correlation between the metrics with the addition of priors. The correlation matrix highlights strong correlation between the AFD and the GFA ($r = 0,67$) or between Nufo

and DISP ($r = 0,89$) in the 'No Priors' measures versus, respectively, $r = 0,4$ and $r = 0,78$ for the 'Priors' group. However, the correlation between the GFA and the NuFo increase ($r = 0,34$ versus $r = 0,5$). These results are also confirmed by the similarity between the various microstructural 'No Priors' profiles (in red on the Figure 5.2). In the same way as with correlation matrices, these similarities decrease with the addition of priors. As they are less correlated, the 'Priors' profiles (in blue) can therefore provide us with information on how these microstructural metrics evolve along the fibers. For example, as they approach the two ends of the Splenium, both NuFo and DISP values increase and the GFA value decrease, indicating a rise in the number of fiber crossings in these areas. This is meaningful because it reflects the role of the splenium in establishing connections between various segments of the two occipital lobes.

5.3.2 R and NR groups differences

In order to study the potential differences between the R and NR groups, we first compared the microstructural metrics of the 2 groups along the 29 bundles. The Figure 5.3 shows one of these comparison for the Splenium. The results indicated, in average, a very slight increase of the AFD No Priors in the R for the Splenium, an increase of the GFA Priors, the AFD Priors and the NuFo Priors for the Thalamo-premotor and a decrease of the Peak Length no Priors and Priors in the the Superior longitudinal fascicle III. However, the Student tests showed that none of these results were significant.

5.3.3 Principal component analysis

The Figure 5.4 displays the contribution of each metrics to the PC of the two PC analysis (i.e. 'Priors' and 'No Priors'). For the 'No Priors', the first PC explain 91% of the variance in the diffusion measures. It is composed of metrics mainly sensitive to fiber crossings with DISP, NuFo, GFA contributing 76%, 22% and 2% respectively. For the 'Prior', the first PC represents 76% of the variance in the data and is composed of AFD (67%), DISP (19%) and NuFO (14%). The second PC explain 20% of the variance with contribution from DISP (51%), AFD (27%) and NuFO (21%). The two PCs can therefore be roughly considered as a measure of fiber density for PC1 and complexity for PC2.

The PCA analysis highlighted significant differences in 6 different fiber bundles, the CC_7, the SLF III right, the T_PREM left, T_PREM right, the ST_PREM left and the ST_PREM right (see Figure 5.5 and 5.6).

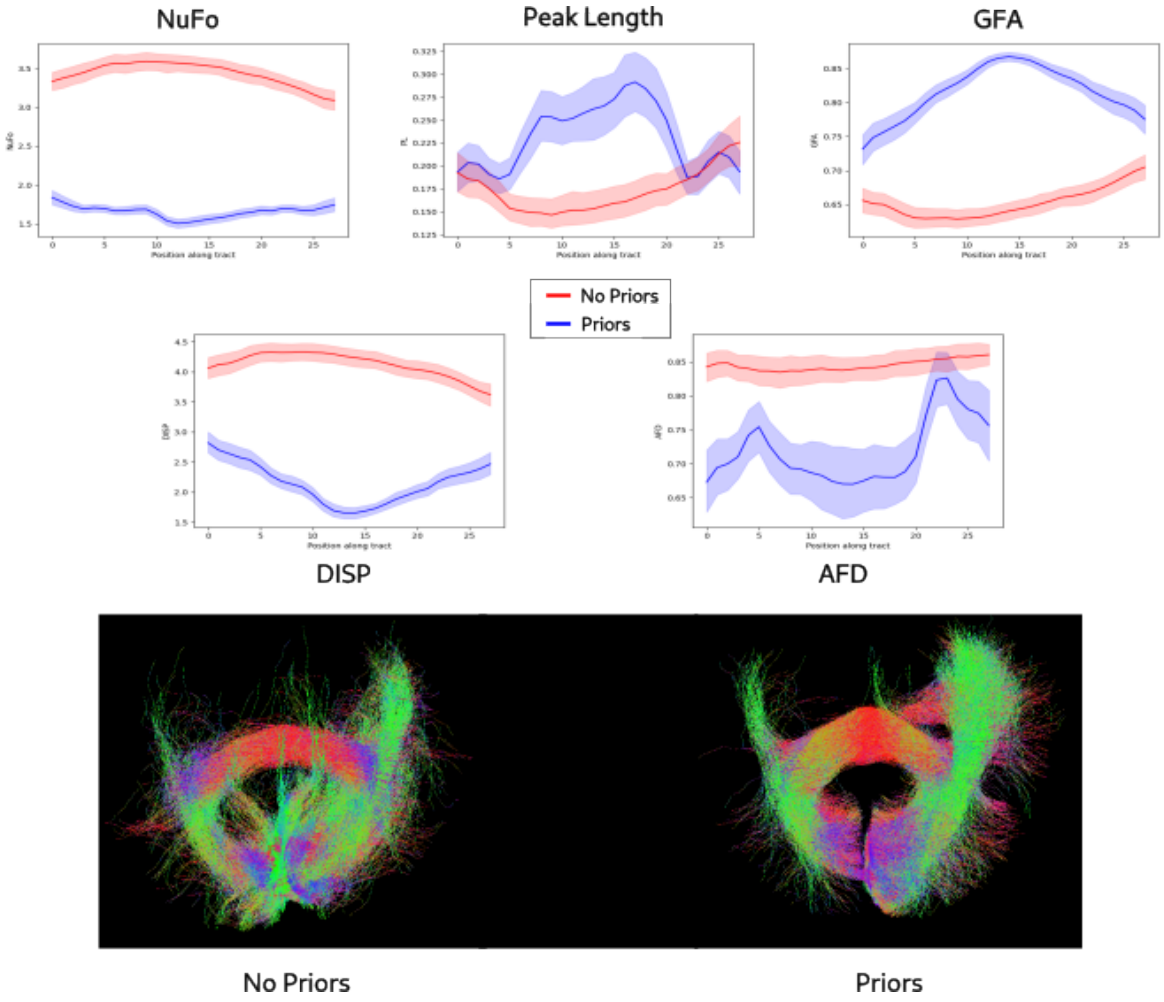

Figure 5.2 – On the top, average of the 5 metrics profiles, projected on the Splenium (CC 7). At the bottom, overview of the segmented tractograms of the Splenium, estimated with and whithout anatomical priors.

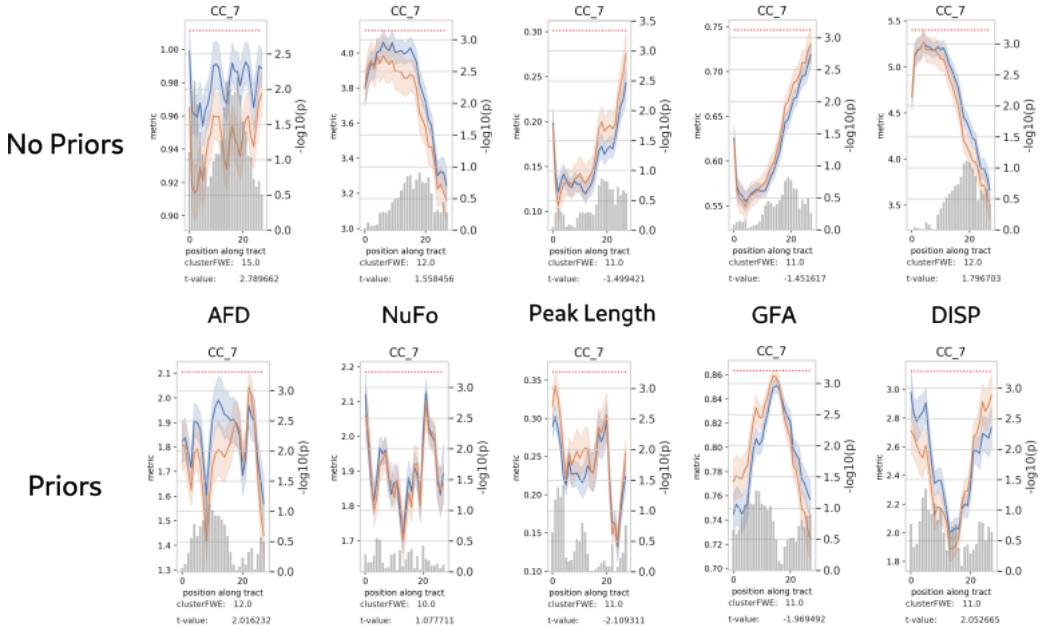

Figure 5.3 – Comparison between the NR (in orange) and R (in blue) groups on the Splenium (CC 7) After removing the influence of age, gender and medication load. For each group, the line represents the average and standard deviation of the microstructural metric.

5.4 Discussion

This is the first study analyzing microstructural metrics along the fibers in TRD estimated by a ODF-based tractography algorithms exploring white matter bundle priors. One of the objectives of this study was to assess how ODF-based microstructural metrics evolve along fibers that are directly estimated from diffusion data in comparison to fibers estimated using anatomical priors, in the context of low-quality DWI data. First, the visual overview of the two splenium bundles presented in the bottom of the Figure 5.2 shows that the addition of priors tends to remove the spurious fibers present in the occipital forceps. Furthermore, it removes the fibers discontinuity occurring at the junction between the forceps and the occipital lobes. The metric profiles displayed at the top of Figure 5.2 also illustrate the enhanced fiber estimation achieved with the incorporation of anatomical priors. When ODFs are derived from low-quality data, they tend to exhibit a roughly spherical shape with nearly identical amplitudes in all directions. This presents a challenge for the tracking algorithm as it struggles to determine preferred directions relative to others in these regions. As displayed in Figure 5.2, this issue is evident in the Disp and NuFo profiles for the estimation with no priors, which exhibit a high number of directions

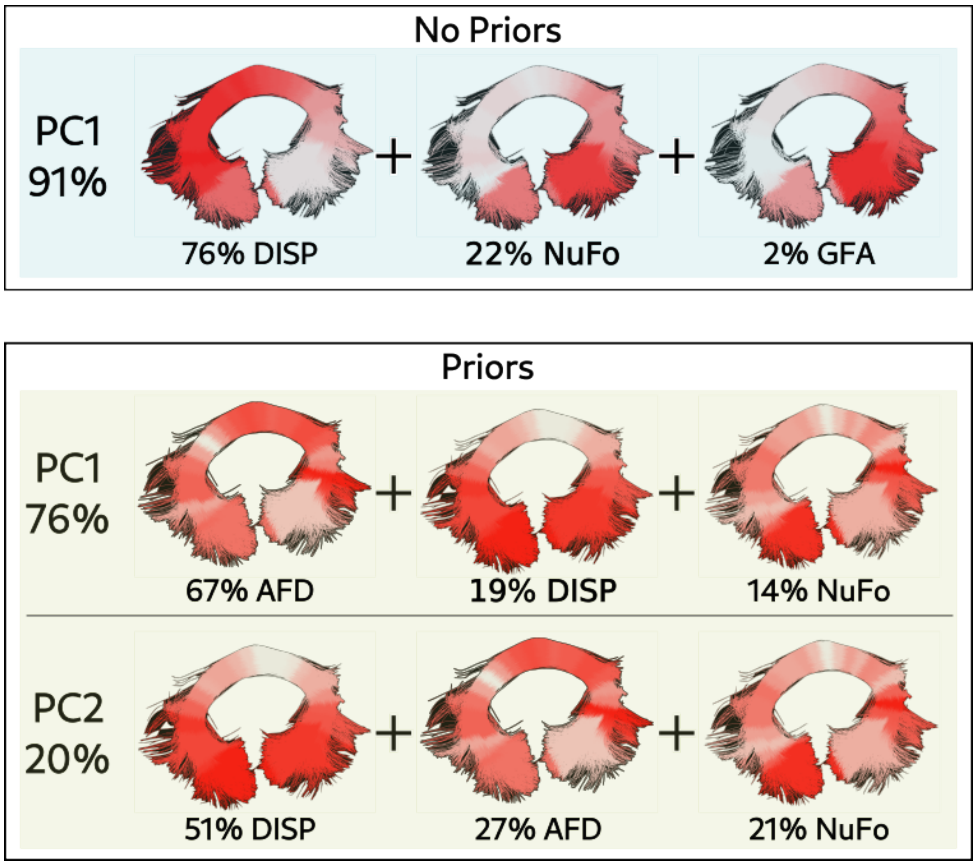

Figure 5.4 – Overview of the composition of the principal components.

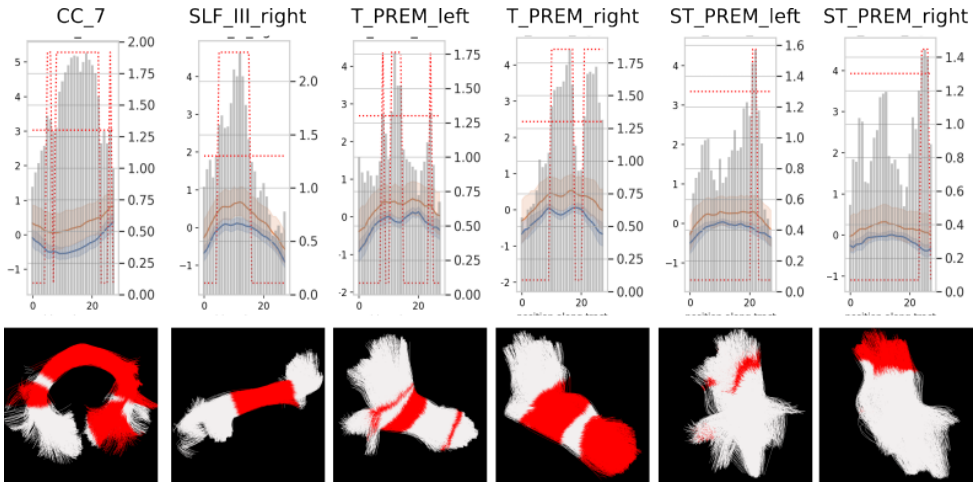

Figure 5.5 – The first row shows the comparison of the PC1 between the NR (in orange) and R (in blue) groups for the No Priors tractograms. For each group, the line represents the average and standard deviation of the PC1, and the gray bar shows the $-log10(p\text{-}values)$. A difference is considered as significant (in red dots) when the p-value is greater than the alpha value (5%) along a minimum cluster size which is estimated individually with the permutation test for each fiber. The second row displays, in red, the regions where significant difference have been detected

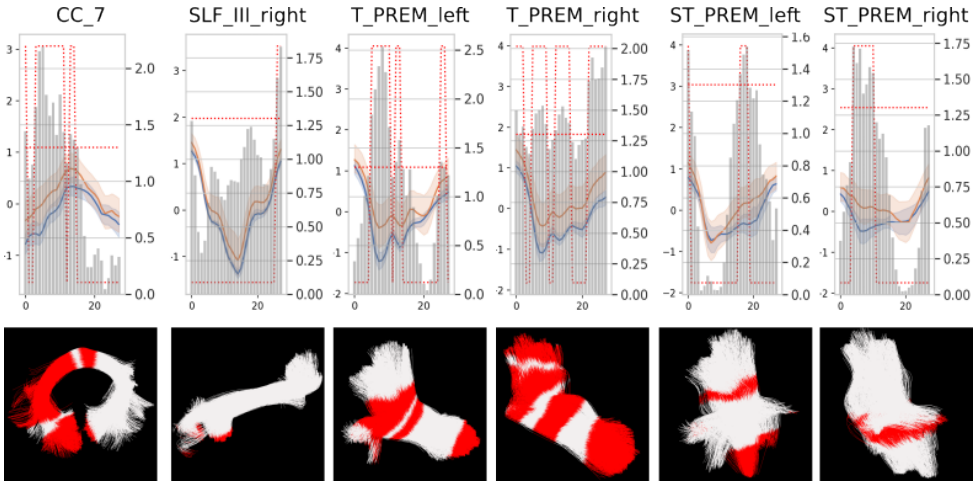

Figure 5.6 – The first row shows the comparison of the PC1 between the NR (in orange) and R (in blue) groups for the Priors tractograms. For each group, the line represents the average and standard deviation of the PC1, and the gray bar shows the $-log10(p\text{-}values)$. A difference is considered as significant (in red dots) when the p-value is greater than the alpha value (5%) along a minimum cluster size which is estimated individually with the permutation test for each fiber. The second row displays, in red, the regions where significant difference have been detected

throughout the fiber, as well as in the GFA profile for no prior, which indicates low GFA, signifying isotropic diffusion across all segments of the bundle. Conversely, following the combination of both data and priors, the distinct lobes of the priors' ODF amplify the amplitudes of the enhanced ODF (i.e. the result of the combination of both data and priors), particularly in directions corresponding to the fibers present in the priors. From the perspective of the tracking algorithm, this leads to a reduction in the number of potential directions, as specific directions become more prominent than others. This effect is apparent in the Prior Disp and NuFo profiles (Figure 5.2), where there is a reduced number of directions in the central part of the Splenium, with an increase in the number of directions as the analysis approaches the occipital lobes, as expected. The Priors GFA profile mirrors these trends, indicating lower diffusion anisotropy in the extremity of the bundle.

The Peak length profiles exhibit a similar pattern. Just as with the number of orientations, the microstructural profile with no priors reveals consistently low peak lengths along the entire length of the bundles. In the Priors scenario, owing to the normalization of the Enhanced ODF, peak lengths are greater in the anisotropic regions due to the reduced diversity of orientations. As we move towards the extremities, where fibers diverge to connect different regions of the occipital lobes, the number of orientations increases, leading to a decrease in peak length.

Finally, in this study AFD refers to the average density of fibers for each fiber orientation within the voxel, as described in more detail in [Raffelt, Tournier, et al., 2012]. The continuously high AFD values in the No Priors profile can be attributed to the presence of numerous spurious fibers within this bundle. Every false fiber contributes to the total AFD, even in regions with isotropic diffusion. Conversely, the enhancement in fiber estimation with the incorporation of priors leads to a reduction in the number of false fibers. As a result, the AFD averaging is no longer skewed by false contributions, allowing for a more direct interpretation of its evolution along the bundle. In [Raffelt, Tournier, et al., 2012], the authors suggest that AFD can be seen as a measure of the intra-axonal volume fraction of axons aligned along the corresponding orientation. In our study, AFD therefore represents the average fraction of intra-axonal axon volume in the voxel. Within the forceps, diffusion is restricted in only a few directions, resulting in a low AFD. As we move towards the occipital lobes, the number of distinct directional restrictions increases, leading to a higher AFD. Ultimately, as the fibers diverge to connect different regions of the occipital lobes, fiber density decreases once again.

Figure 5.1 and the overall profile shape illustrated in Figure 5.2 provide valuable insights into the significant improvements brought about by the integration of anatomical priors. This enhancement in fiber direction estimation, achieved through the addition of anatomical priors, leads to a notable reduction in the correlation among different microstructural metrics. This decorrelation process enhances the informativeness of these metrics and augments their sensitivity, thereby enabling us to discern and interpret more nuanced aspects of their evolution along the fiber bundles. Consequently, the incorporation of anatomical priors not only refines our understanding of these metrics but also amplifies their utility in capturing and elucidating intricate patterns of change along the neural pathways.

The presence of observed heterogeneity inspired us to undertake a Principal Component Analysis (PCA) with the goal of consolidating the interconnected metrics into primary modes of variation. PCA is often challenged by the complexity of interpreting the resulting components, but in our study, the principal components demonstrated loadings on variables that shared similarities in their responsiveness to various tissue properties. This common sensitivity among variables facilitated a more coherent and insightful interpretation of the resulting components. As displayed in 5.4 the first principal component alone can explain 91% of the data in the absence of prior, and is primarily composed of measures that are highly sensitive to dispersion. However, the inclusion of priors allows for the differentiation of two groups of metrics. The metrics that contribute the most to PC1 are AFD, whereas for PC2, Disp is the dominant contributor, followed by AFD. Consequently, PC1 can be interpreted as a component primarily sensitive to the restriction of diffusion signal, while PC2 is a component primarily sensitive to the dispersion of fibers. The incorporation of prior seems to estimate less correlated microstructural metrics.

Another objective of this study was to conduct a tractometry analysis to uncover potential differences between patients with TRD and those without treatment resistance. Previous studies investigate tract profiling in various brain diseases [Yeatman et al., 2012; Cousineau et al., 2017; Sarica et al., 2017]. While previous research has explored DTI-derived biomarkers related to major depressive disorder or TRD [Serafini et al., 2015; Coloigner et al., 2019; Sun et al., 2022; Grehl et al., 2023; Meshkat et al., 2022] this is the first tractometry study in TRD.

In this study, we opted for tractometry and tract profiling because, within this context, they offer several advantages over the standard voxel-based analysis [Yeatman et al., 2012]. Firstly, diffusion measure values exhibit significant variation within a tract, but

the tract profiles remain consistent across subjects. Consequently, tract profiles contain a wealth of information beyond what mean diffusion measures can provide. Secondly, variations in diffusion measures may occur at particular locations within the bundle, rather than uniformly along the entire tract. Consequently, the use of tract profiles enables the detection of these specific locations. Lastly, tract profiles enable the comparison of white matter properties between groups, facilitating the identification of distinctive differences related to the clinical conditions of these groups.

Both the PCA analyses of the No Priors and Priors bundles revealed a significant reduction in measures of restriction and dispersion within the splenium of the CC among patients with TRD in comparison to those without TRD. This result is in accordance with other studies which reported a FA decrease in late-life depression [Yang et al., 2007], as well as in the Splenium of adult patients with Major Depressive Disorder (MDD) and melancholic features [Korgaonkar et al., 2011]. The corpus callosum plays a crucial role in facilitating communication between the two cerebral hemispheres, including the integration of high-level cognitive functions, language, and sensory perception. Morover, the white matter located near the corpus callosum encompasses the callosal fibers, which establish connections between the striatum, thalamus, and inter-hemispheric regions. Reduced anisotropy in these tracts has been linked to a diminished response to antidepressant treatment [Alexopoulos et al., 2008.These findings suggest a potential association between TRD and the disruption of white matter integrity in this specific brain region.

Additionally, our study revealed significant differences within the white matter of the Striato-premotor region. Previous studies have already observed differences between TRD and non-TRD individuals in striatal circuits through the use of functional MRI techniques [Sun et al., 2022]. Pleasure deficits, one of the key symptoms in TRD [de Kwaasteniet et al., 2014], reflect disruptions in reward circuits, and the striatum is an important structure in the reward network that regulates reward, motivation, and affective functions in the body [Cox and Witten, 2019]. This convergence of findings in both structural and functional domains emphasizes the potential significance of the Striatum in the context of TRD, suggesting that it may play a key role in the neurobiological mechanisms underlying this condition.

Finally, our study suffers from a few limitations that should be addressed in future work. First, we only utilized ODF-derived measures to characterize underlying tissue microstructure. Although our findings suggest the suitability of these measures for highlighting certain biomarkers in diffusion data, the omission of measures derived from DTI

may potentially limit sensitivity [Chamberland et al., 2019]. Additionally, incorporating other macrostructural measures such as bundle volume or mean length [Lebel et al., 2019; Girard et al., 2014; Geeraert et al., 2017] could offer complementary features that enhance the description of potential biomarkers. The inclusion of rotationally invariant spherical harmonic features [Mirzaalian et al., 2015; Caruyer and Verma, 2015; Zucchelli et al., 2018] is another avenue worth exploring, as it directly represents diffusion signals without relying on various microstructural models.

Secondly, while our results indicate that the addition of priors enhances metric sensitivity and improves interpretability, it's essential to acknowledge that these priors were estimated from a population of healthy subjects (as discussed in Chapter 2). This approach may inadvertently diminish the emphasis on disease-related differences.

Lastly, using a single centerline for certain fibers with diverse orientations may not be entirely accurate. Recent studies have proposed alternative approaches, such as considering the entire segmentation of fiber bundles as the shape, rather than relying solely on their centerlines, which may offer improved accuracy and efficiency [Cury et al., 2022; Glozman et al., 2018].

5.5 Conclusions

In conclusion, this study compared microstructural metrics of white matter fibers estimated directly from diffusion data with those estimated using anatomical priors. The addition of priors improved fiber estimation by removing spurious fibers and enhancing the fibers orientation, resulting in more focused profiles and peak lengths. Apparent Fiber Density (AFD) provided a clearer insight into white matter density when priors were used.

Furthermore, incorporating anatomical priors improved the de-correlation of microstructural metrics, enhancing their sensitivity and interpretability. Principal Component Analysis (PCA) revealed two dominant components: PC1, primarily related to diffusion signal restriction, and PC2, mainly influenced by fiber dispersion.

Our study also investigated differences between patients with and without Treatment-Resistant Depression (TRD) using tractometry. We observed decreased measures of restriction and dispersion in the Splenium of the corpus callosum among TRD patients, consistent with previous findings in depression. Additionally, differences in white matter within the Striato-premotor region were noted, aligning with prior functional MRI studies indicating variations in striatal circuits among TRD individuals.

Conclusion

5.6 Contributions

White matter tractography presents substantial potential as a method for investigating the pathways of nerve fibers within the brain. Its non-invasive ability to depict the microstructural organization of axons makes it a valuable resource for both academic research and clinical diagnosis. Nevertheless, despite its high promise, tractography methods face several limitations. In fact, the majority of tractograms tend to include more erroneous fiber pathways than accurate ones. As a result, this manuscript has introduced contributions aimed at improving the accuracy of tractogram estimation. All the proposed methods have been incorporated into our team code Anima. This open-source software is accessible online, along with its associated documentation [1].

The multitude of existing tractography methods introduces significant variability in the reconstruction of fiber bundles. This variability poses challenges for clinicians in accurately interpreting results and complicates the assessment and comparison of tractography algorithms. To tackle this issue, we have introduced a comprehensive analysis of frequently employed metrics. Our study, conducted on synthetic data and real-world scenarios, demonstrated the usefulness of employing multiple measures simultaneously, as they exhibit non-correlated attributes and therefore offer distinct types of information. Additionally, we have proposed a novel evaluation measure for tractograms, based on optimal transport, which enables the characterization of both topographical similarities and the degree of overlap between two tractograms.

Another well-known limitation of tractography algorithms concerns their poor anatomical accuracy. Sources of error can arise at any stage of the tracking process, including image acquisition, voxel-wise local reconstruction, and tracking streamlines from voxel to voxel. Another source of error arises from the inference of local fiber orientation solely from the diffusion displacement profile, often resulting in anatomically unrealistic outcomes in complex fiber configurations. To expand the foundation of tractography algorithms beyond relying solely on water diffusion displacement, we have introduced a method for

1. https://github.com/Inria-Visages/Anima-Public

generating and integrating anatomical priors. This approach serves to provide guidance for tracking and can be seamlessly employed alongside any ODF-based tractography algorithm. These priors are computed based on fiber atlases and are expressed in the form of TOD, enabling the characterization of brain variability and the representation of multiple fiber directions. Subsequently, the prior information is integrated into the ODF-based tractography algorithm through a Riemannian framework, aiding in the guidance of the tracking process. Our study, conducted using both synthetic and high-quality real-world data, demonstrates that this approach can enhance fiber reconstruction, particularly in terms of spatial coverage and the generation of valid streamlines, especially in regions with crossing fibers.

While promising results were achieved with high-quality data, the primary purpose of integrating anatomical priors into tractography algorithms was to improve fiber estimation, particularly in low-quality data scenarios. Consequently, we applied the previously described method to clinical data obtained from patients with treatment-resistant depression (TRD). Depression, being the third leading global cause of illness, often recurs in 40% of cases, primarily due to treatment resistance. Identifying biomarkers associated with this condition is crucial to assist clinicians in treatment selection. In this context, we conducted a comparative analysis to distinguish patients with TRD from those without resistance using tractometry methods. By incorporating anatomical priors to enhance the quality of fiber estimation and employing ODF-based metrics to characterize diffusion microstructure along fiber bundles, this analysis revealed that the inclusion of anatomical priors during the tracking process heightened the sensitivity and interpretability of diffusion metrics. Furthermore, the combined use of priors and Principal Component Analysis disclosed alterations in white matter consistent with prior findings in depression.

5.7 Perspectives

While all the contributions presented in this manuscript were conducted using ODF models, it's worth noting that these models, despite their benefits for tractography, particularly in the context of local probabilistic methods, have limitations. They don't provide precise quantitative measurements related to diffusion magnitude and anisotropy, which indirectly reflect microstructural organization. Consequently, they lack anatomical interpretability, unlike tensor models, for example. However, alternatives like multi-compartment models (MCM) exist, with the primary aim of modeling the brain's mi-

crostructure through several compartments [Pasternak et al., 2009; H. Zhang et al., 2012a]. Each compartment represents specific diffusion properties within different brain structures, such as cerebrospinal fluid (CSF) and axons, enabling the representation of complex fiber structures and detailed descriptions of brain microstructure. Therefore, a natural extension of the proposed method could involve developing MCM-based priors, which not only offer directional information but also incorporate microstructural details

Another area for improvement could be to study the PSF used to construct the TOD images. Our approach uses 2D Gaussians expressed in a spherical harmonic basis. Although this approach allows us to estimate TODs that are naturally positive at any SH order, it could degrade the results obtained by producing lobes that are too wide to be effectively used by tractography algorithms. An alternative would be to use, as in the BST method [Rheault et al., 2019], apodized delta functions which produce much sharper lobes and are therefore able to provide much more precise directional information.

Moreover, our approach has primarily focused on diffusion MRI. However, it's worth considering the exploration of other imaging modalities for creating priors. For example, the utilization of myelin-sensitive T1 mapping, as documented in prior research [Schurr et al., 2018], has shown promise in optimizing tractography. Thus, the integration of multimodal MRI microstructural information presents an intriguing avenue to mitigate the generation of spurious fibers and enhance the accuracy of tractography. In this context, the exploration of estimating priors from the rich information provided by this multimodal MRI microstructural data becomes a noteworthy consideration.

The previous point highlights new challenges that would necessitate a novel approach for resolution. Integrating multi-modal imaging information would entail the creation of multiple atlases to extract the required data for constructing a multi-modal prior. Consequently, there would be a need to calculate distances between these atlases to facilitate their alignment, even when they represent different modalities of information. This could serve as a catalyst for future research aimed at implementing multi-atlas techniques [Iglesias and Sabuncu, 2014] within the prior creation process. In addition to the ability to amalgamate atlases from various imaging modalities, this approach, by selecting and merging the most suitable atlases from a database for each individual patient, would enhance the precision of prior estimations, thus allowing for a more accurate capture of anatomical variations.

Finally, from a clinical perspective, our method has proven to be a valuable tool in characterizing pathological biomarkers in patients suffering from treatment-resistant de-

pression. These encouraging findings not only underscore the potential of our approach but also serve as a catalyst for further exploration in this domain. Future investigations should delve into whether the inclusion of anatomical priors can bolster fiber estimation, particularly in situations where the white matter has sustained severe damage. If such enhancements prove inadequate, an exploration of alternative information sources or different diffusion measures to compute these weights should be on the research agenda. This would provide a more comprehensive understanding of how anatomical priors can be optimized for diverse clinical scenarios.

PUBLICATIONS

A Convolutional Wasserstein Distance for Tractography Evaluation: Complementarity Study to State-of-the-Art Measures.
Durantel, T., Coloigner, J. and Commowick, O.
19th International Symposium on Biomedical Imaging, Kolkata, India, 2022.

Anatomical priors informed tractography. Evaluation on the DiSCo synthetic dataset.
Durantel, T., Coloigner, J., Caruyer, E., Girard, G., and Commowick, O.
International Society for Magnetic Resonance in Medicine, Toronto, Canada, 2023.

A Riemannian framework for incorporating white matter bundle priors in ODF-based tractography algorithms.
Durantel, T., Coloigner, J., Caruyer, E., Girard, G., and Commowick, O.
A preprint of this work is available at https://hal.science/hal-04246380. In addition, it will be submitted in the coming weeks to the journal Human Brain mapping (HBM).

BIBLIOGRAPHY

Aganj, I., Lenglet, C., Jahanshad, N., Yacoub, E., Harel, N., Thompson, P. M., & Sapiro, G., (2011), A hough transform global probabilistic approach to multiple-subject diffusion mri tractography, *Medical image analysis*, *15 4*, 414–425.

Aganj, I., Lenglet, C., Sapiro, G., Yacoub, E., Ugurbil, K., & Harel, N., (2010), Reconstruction of the orientation distribution function in single- and multiple-shell q-ball imaging within constant solid angle, *Magnetic Resonance in Medicine*, *64 2*, 554–566, https://doi.org/https://doi.org/10.1002/mrm.22365

Akaike, H., (1998), Information theory and an extension of the maximum likelihood principle. *In Selected papers of hirotugu akaike* (pp. 199–213), Springer.

Alexander, A. L., Lee, J., Lazar, M., & Field, A., (2007), Diffusion tensor imaging of the brain, *Neurotherapeutics*, *4 3*, 316–329.

Alexander, A. L., Hasan, K. M., Lazar, M., Tsuruda, J. S., & Parker, D. L., (2001), Analysis of partial volume effects in diffusion-tensor mri, *Magnetic Resonance in Medicine*, *45*, https://api.semanticscholar.org/CorpusID:378209

Alexander, D. C., (2008), A general framework for experiment design in diffusion mri and its application in measuring direct tissue-microstructure features, *Magnetic Resonance in Medicine*, *60*, https://api.semanticscholar.org/CorpusID:6890975

Alexopoulos, G. S., (2019), Mechanisms and treatment of late-life depression, *Translational Psychiatry*, *9*, https://api.semanticscholar.org/CorpusID:199435880

Alexopoulos, G. S., Kiosses, D. N., Heo, M., Murphy, C. F., Shanmugham, B. R., & Gunning-Dixon, F. M., (2005), Executive dysfunction and the course of geriatric depression, *Biological Psychiatry*, *58*, 204–210, https://api.semanticscholar.org/CorpusID:39377620

Alexopoulos, G. S., Murphy, C. F., Gunning-Dixon, F. M., Latoussakis, V., Kanellopoulos, D., Klimstra, S. A., Lim, K. O., & Hoptman, M. J., (2008), Microstructural white matter abnormalities and remission of geriatric depression., *The American journal of psychiatry*, *165 2*, 238–44, https://api.semanticscholar.org/CorpusID:18507871

Al-Harbi, K. S., (2012), Treatment-resistant depression: therapeutic trends, challenges, and future directions, *Patient preference and adherence*, *6*, 369–388, https://api.semanticscholar.org/CorpusID:17627229

Arsigny, V., et al., (2006a), A Log-Euclidean framework for statistics on diffeomorphisms, *MICCAI*, *4190*, 924–931.

Arsigny, V., Commowick, O., Pennec, X., & Ayache, N., (2006b), A log-euclidean framework for statistics on diffeomorphisms, *International Conference on Medical Image Computing and Computer-Assisted Intervention*, 924–931.

Assaf, Y., & Basser, P. J., (2005), Composite hindered and restricted model of diffusion (charmed) mr imaging of the human brain, *NeuroImage*, *27*, 48–58, https://api.semanticscholar.org/CorpusID:1306417

Assaf, Y., & Pasternak, O., (2007), Diffusion tensor imaging (dti)-based white matter mapping in brain research: a review, *Journal of Molecular Neuroscience*, *34*, 51–61, https://api.semanticscholar.org/CorpusID:3354176

Aydogan, D., & Shi, Y., (2021), Parallel transport tractography, *IEEE Transactions on Medical Imaging*, *40 2*, 635–647, https://doi.org/10.1109/TMI.2020.3034038

Aydogan, D. B., Jacobs, R. E., Dulawa, S. C., Thompson, S. L., Francois, M. C., Toga, A. W., Dong, H.-w., Knowles, J. A., & Shi, Y., (2018), When tractography meets tracer injections: a systematic study of trends and variation sources of diffusion-based connectivity, *Brain Structure and Function*, *223*, 2841–2858, https://api.semanticscholar.org/CorpusID:4890852

Aydogan, D. B., & Shi, Y., (2018), Tracking and validation techniques for topographically organized tractography, *NeuroImage*, *181*, 64–84, https://doi.org/https://doi.org/10.1016/j.neuroimage.2018.06.071

Aydogan, D. B., & Shi, Y., (2020), Parallel transport tractography, *IEEE Transactions on Medical Imaging*, *40*, 635–647, https://api.semanticscholar.org/CorpusID:225083950

Aydogan, D. B., & Shi, Y., (2021), Parallel transport tractography, *IEEE Transactions on Medical Imaging*, *40 2*, 635–647, https://doi.org/10.1109/TMI.2020.3034038

Bains, N., & Abdijadid, S., (2020), Major depressive disorder, https://api.semanticscholar.org/CorpusID:79747872

Basser, P. J., Mattiello, J., & LeBihan, D., (1994a), Estimation of the effective self-diffusion tensor from the nmr spin echo., *Journal of magnetic resonance. Series B*, *103 3*, 247–54, https://api.semanticscholar.org/CorpusID:35400872

Basser, P. J., Mattiello, J., & LeBihan, D., (1994b), Mr diffusion tensor spectroscopy and imaging., *Biophysical journal*, *66 1*, 259–67, https://api.semanticscholar.org/CorpusID:8747275

Basser, P. J., Pajevic, S., Pierpaoli, C., Duda, J. T., & Aldroubi, A., (2000), In vivo fiber tractography using dt-mri data, *Magnetic Resonance in Medicine*, *44*, https://api.semanticscholar.org/CorpusID:240063

Basser, P. J., & Pierpaoli, C., (1996), Microstructural and physiological features of tissues elucidated by quantitative-diffusion-tensor mri., *Journal of magnetic resonance. Series B*, *111 3*, 209–19, https://api.semanticscholar.org/CorpusID:8799461

Basser, P., et al., (2000a), In vivo fiber tractography using DT-MRI data, *Magn Reson Med.*, *44*, 625–32, https://doi.org/10.1002/1522-2594(200010)44:4<625::aid-mrm17>3.0.co;2-o

Basser, P., et al., (2000b), In vivo fiber tractography using DT-MRI data, *Magn Reson Med.*, *44*, 625–32, https://doi.org/10.1002/1522-2594(200010)44:4<625::aid-mrm17>3.0.co;2-o

Beaudoin, A.-M., Rheault, F., Theaud, G., Laberge, F., Whittingstall, K., Lamontagne, A., & Descoteaux, M., (2021), Modern technology in multi-shell diffusion mri reveals diffuse white matter changes in young adults with relapsing-remitting multiple sclerosis, *Frontiers in Neuroscience*, *15*, https://api.semanticscholar.org/CorpusID:236971525

Beaulieu, C., (2002), The basis of anisotropic water diffusion in the nervous system – a technical review, *NMR in Biomedicine*, *15*, https://api.semanticscholar.org/CorpusID:9187994

Behrens, T., Berg, H. J., Jbabdi, S., Rushworth, M., & Woolrich, M., (2007), Probabilistic diffusion tractography with multiple fibre orientations: what can we gain?, *NeuroImage*, *34 1*, 144–155, https://doi.org/https://doi.org/10.1016/j.neuroimage.2006.09.018

Behrens, T. E. J., Johansen-Berg, H., Jbabdi, S., Rushworth, M. F. S., & Woolrich, M. W., (2007), Probabilistic diffusion tractography with multiple fibre orientations: what can we gain?, *NeuroImage*, *34*, 144–155, https://api.semanticscholar.org/CorpusID:16455152

Behrens, T. E. J., Woolrich, M. W., Jenkinson, M., Johansen-Berg, H., Nunes, R. G., Clare, S., Matthews, P. M., Brady, J., & Smith, S., (2003), Characterization and

propagation of uncertainty in diffusion-weighted mr imaging, *Magnetic Resonance in Medicine*, *50*, https://api.semanticscholar.org/CorpusID:39297954

Bertani, G., Bertulli, L., Scola, E., Di Cristofori, A., Zavanone, M., Triulzi, F., Rampini, P., & Carrabba, G., (2018), Optic radiation diffusion tensor imaging tractography: an alternative and simple technique for the accurate detection of meyer's loop, *World Neurosurgery*, *117*, e42–e56, https://doi.org/https://doi.org/10.1016/j.wneu.2018.05.131

Bihan, D. L., Breton, E., Lallemand, D., Grenier, P. A., Cabanis, E. A., & Laval-jeantet, M., (1986), Mr imaging of intravoxel incoherent motions: application to diffusion and perfusion in neurologic disorders., *Radiology*, *161 2*, 401–7, https://api.semanticscholar.org/CorpusID:14420005

Bloch, F., Hansen, W. W., & Packard, M. E., (1946), The nuclear induction experiment, *Physical Review*, *70*, 474–485, https://api.semanticscholar.org/CorpusID:120753684

Bonneel, N., & Coeurjolly, D., (2019), Spot: sliced partial optimal transport, *ACM Trans. Graph.*, *38 4*, https://doi.org/10.1145/3306346.3323021

Bracewell, R. N., Buneman, O. P., Hao, H., & Villasenor, J. D., (1986), Fast two-dimensional hartley transform, *Proceedings of the IEEE*, *74*, 1282–1283, https://api.semanticscholar.org/CorpusID:43836118

Brown, R., (1828), Xxvii. a brief account of microscopical observations made in the months of june, july and august 1827, on the particles contained in the pollen of plants; and on the general existence of active molecules in organic and inorganic bodies, *The Philosophical Magazine*, *4 21*, 161–173, https://doi.org/10.1080/14786442808674769

Brusini, I., Jörgens, D., Smedby, Ö., & Moreno, R., (2019), Voxel-wise clustering of tractography data for building atlases of local fiber geometry, *Computational Diffusion MRI*, https://api.semanticscholar.org/CorpusID:182833798

Caiafa, C. F., & Pestilli, F., (2017), Multidimensional encoding of brain connectomes, *Scientific Reports*, *7*, https://api.semanticscholar.org/CorpusID:21234692

Callaghan, P. T., Eccles, C. D., & Xia, Y., (1988), Rapid communication: nmr microscopy of dynamic displacements: k-space and q-space imaging, *Journal of Physics E: Scientific Instruments*, https://api.semanticscholar.org/CorpusID:117473833

Campbell, J. S. W., Siddiqi, K., Rymar, V. V., Sadikot, A. F., & Pike, G. B., (2005), Flow-based fiber tracking with diffusion tensor and q-ball data: validation and

comparison to principal diffusion direction techniques, *NeuroImage*, *27*, 725–736, https://api.semanticscholar.org/CorpusID:17565831

Caruyer, E., & Verma, R., (2015), On facilitating the use of hardi in population studies by creating rotation-invariant markers, *Medical image analysis*, *20 1*, 87–96, https://api.semanticscholar.org/CorpusID:8750963

Catani, M., Howard, R. J., Pajevic, S., & Jones, D. K., (2002), Virtual in vivo interactive dissection of white matter fasciculi in the human brain, *NeuroImage*, *17*, 77–94, https://api.semanticscholar.org/CorpusID:12129663

Chamberland, M., Raven, E. P., Genc, S., Duffy, K., Descoteaux, M., Parker, G. D., Tax, C. M. W., & Jones, D. K., (2019), Dimensionality reduction of diffusion mri measures for improved tractometry of the human brain, *Neuroimage*, *200*, 89–100, https://api.semanticscholar.org/CorpusID:92810767

Chandio, B. Q., Risacher, S. L., Pestilli, F., Bullock, D., Yeh, F.-C., Koudoro, S., Rokem, A. S., Harezlak, J., & Garyfallidis, E., (2020), Bundle analytics, a computational framework for investigating the shapes and profiles of brain pathways across populations, *Scientific Reports*, *10*, https://api.semanticscholar.org/CorpusID:222345135

Chang, L.-C., Jones, D. K., & Pierpaoli, C., (2005), Restore: robust estimation of tensors by outlier rejection, *Magnetic Resonance in Medicine*, *53*, https://api.semanticscholar.org/CorpusID:6108499

Cohen-Adad, J., Descoteaux, M., & Wald, L. L., (2011), Quality assessment of high angular resolution diffusion imaging data using bootstrap on q-ball reconstruction, *Journal of Magnetic Resonance Imaging*, *33*, https://api.semanticscholar.org/CorpusID:1219464

Colby, J. B., Soderberg, L., Lebel, C. A., Dinov, I. D., Thompson, P. M., & Sowell, E. R., (2012), Along-tract statistics allow for enhanced tractography analysis, *NeuroImage*, *59*, 3227–3242, https://api.semanticscholar.org/CorpusID:33576723

Collins, B., Nechita, I., & Życzkowski, K., (2010), Random graph states, maximal flow and fuss–catalan distributions, *Journal of Physics A: Mathematical and Theoretical*, *43*, 275303, https://api.semanticscholar.org/CorpusID:115158150

Coloigner, J., Batail, J.-M., Commowick, O., Corouge, I., Robert, G., Barillot, C., & Drapier, D., (2019), White matter abnormalities in depression: a categorical and phenotypic diffusion mri study, *NeuroImage : Clinical*, *22*, https://api.semanticscholar.org/CorpusID:72332300

Cook, P., Zhang, H., Awate, S., & Gee, J., (2008), Atlas-guided probabilistic diffusion-tensor fiber tractography, *2008 5th IEEE International Symposium on Biomedical Imaging: From Nano to Macro*, 951–954.

Côté, M.-A., et al., (2013a), Tractometer: towards validation of tractography pipelines [Special Issue on the 2012 Conference MICCAI], *Medical Image Analysis*, *17 7*, 844–857, https://doi.org/https://doi.org/10.1016/j.media.2013.03.009

Côté, M.-A., Girard, G., Boré, A., Garyfallidis, E., Houde, J.-C., & Descoteaux, M., (2013b), Tractometer: towards validation of tractography pipelines, *Medical image analysis*, *17 7*, 844–57, https://api.semanticscholar.org/CorpusID:15933496

Courant, R., & Hilbert, D., (1953), *Methods of mathematical physics*, Interscience Publishers, https://books.google.fr/books?id=6gVRAAAAMAAJ

Cousineau, M., Jodoin, P.-M., Garyfallidis, E., Côté, M.-A., Morency, F. C., Rozanski, V. E., Grand'maison, M., Bedell, B. J., & Descoteaux, M., (2017), A test-retest study on parkinson's ppmi dataset yields statistically significant white matter fascicles, *NeuroImage : Clinical*, *16*, 222–233, https://api.semanticscholar.org/CorpusID:13644331

Cox, J., & Witten, I. B., (2019), Striatal circuits for reward learning and decision-making, *Nature Reviews Neuroscience*, 1–13, https://api.semanticscholar.org/CorpusID:174810439

Crum, W., et al., (2006a), Generalized overlap measures for evaluation and validation in medical image analysis, *IEEE Transactions on Medical Imaging*, *25 11*, 1451–1461, https://doi.org/10.1109/TMI.2006.880587

Crum, W., Camara, O., & Hill, D., (2006b), Generalized overlap measures for evaluation and validation in medical image analysis, *IEEE transactions on medical imaging*, *25 11*, 1451–1461.

Cury, C., Batail, J.-M., & Coloigner, J., (2022), Shape-based features of white matter fiber-tracts associated with outcome in major depression disorder, *International Conference on Medical Image Computing and Computer-Assisted Intervention*, https://api.semanticscholar.org/CorpusID:252369364

Cuturi, M., (2013), Sinkhorn distances: lightspeed computation of optimal transport, *Advances in Neural Information Processing Systems*, *26*, https://proceedings.neurips.cc/paper/2013/file/af21d0c97db2e27e13572cbf59eb343d-Paper.pdf

Daducci, A., Canales-Rodriguez, E., Zhang, H., Dyrby, T., Alexander, D., & Thiran, J., (2015), Accelerated microstructure imaging via convex optimization (amico) from diffusion mri data, *Neuroimage*, *105*, 32–44.

Daducci, A., Dal Palu, A., Descoteaux, M., & Thiran, J., (2016), Microstructure informed tractography: pitfalls and open challenges, *Frontiers in neuroscience*, *10*, 247.

Daducci, A., Palù, A. D., Lemkaddem, A., & Thiran, J.-P., (2015), Commit: convex optimization modeling for microstructure informed tractography, *IEEE Transactions on Medical Imaging*, *34*, 246–257, https://api.semanticscholar.org/CorpusID:2552225

de Diego-Adeliño, J., Pires, P., Gómez-Anson, B., Serra-Blasco, M., Vives-Gilabert, Y., Puigdemont, D., Martín-Blanco, A., Alvarez, E., Pérez, V., & Portella, M. J., (2013), Microstructural white-matter abnormalities associated with treatment resistance, severity and duration of illness in major depression, *Psychological Medicine*, *44*, 1171–1182, https://api.semanticscholar.org/CorpusID:39845722

de Kwaasteniet, B. P., Pinto, C., Ruhe, E., van Wingen, G. A., Booij, J., & Denys, D. A., (2014), Striatal dopamine d2/3 receptor availability in treatment resistant depression, *PLoS ONE*, *9*, https://api.semanticscholar.org/CorpusID:1092210

Dell'Acqua, F., & Tournier, J., (2017), Reconstructing fiber orientations with diffusion mri, *NMR Biomed*.

Dell'Acqua, F., Simmons, A., Williams, S. C. R., & Catani, M., (2013), Can spherical deconvolution provide more information than fiber orientations? hindrance modulated orientational anisotropy, a true-tract specific index to characterize white matter diffusion, *Human Brain Mapping*, *34*, https://api.semanticscholar.org/CorpusID:16184276

Descoteaux, M., et al., (2007a), Regularized, fast, and robust analytical q-ball imaging, *Magn Reson Med.*, *58*, 497–510, https://doi.org/10.1002/mrm.21277

Descoteaux, M., (2015), High angular resolution diffusion imaging (hardi). *In Wiley encyclopedia of electrical and electronics engineering* (pp. 1–25), John Wiley Sons, Ltd, https://doi.org/https://doi.org/10.1002/047134608X.W8258

Descoteaux, M., Angelino, E., Fitzgibbons, S., & Deriche, R., (2007b), Regularized, fast, and robust analytical q-ball imaging, *Magnetic Resonance in Medicine*, *583*, 497–510, https://doi.org/https://doi.org/10.1002/mrm.21277

Descoteaux, M., Deriche, R., Knosche, T., & Anwander, A., (2008), Deterministic and probabilistic tractography based on complex fibre orientation distributions, *IEEE transactions on medical imaging*, *28 2*, 269–286.

Descoteaux, M., (2008), High angular resolution diffusion mri : from local estimation to segmentation and tractography, https://api.semanticscholar.org/CorpusID:117966190

Descoteaux, M., Angelino, E., Fitzgibbons, S., & Deriche, R., (2007c), Regularized, fast, and robust analytical q-ball imaging, *Magnetic Resonance in Medicine*, *58*, https://api.semanticscholar.org/CorpusID:2516335

Descoteaux, M., Deriche, R., Knösche, T. R., & Anwander, A., (2009), Deterministic and probabilistic tractography based on complex fibre orientation distributions, *IEEE Transactions on Medical Imaging*, *28*, 269–286, https://api.semanticscholar.org/CorpusID:12797339

Dhollander, T., Emsell, L., Van Hecke, W., Maes, F., Sunaert, S., & Suetens, P., (2014), Track orientation density imaging (todi) and track orientation distribution (tod) based tractography, *NeuroImage*, *94*, 312–336.

Diniz, B. S., Butters, M. A., Albert, S. M., Dew, M. A., & Reynolds, C. F., (2013), Late-life depression and risk of vascular dementia and alzheimer's disease: systematic review and meta-analysis of community-based cohort studies, *British Journal of Psychiatry*, *202*, 329–335, https://api.semanticscholar.org/CorpusID:5024414

Dong, X., Zhang, Z., & Srivastava, A., (2017), Bayesian tractography using geometric shape priors, *Frontiers in Neuroscience*, *11*, https://api.semanticscholar.org/CorpusID:24850247

Drevets, W. C., (2001), Neuroimaging and neuropathological studies of depression: implications for the cognitive-emotional features of mood disorders, *Current Opinion in Neurobiology*, *11*, 240–249, https://api.semanticscholar.org/CorpusID:36416079

Einstein, A. B., (1905), On the motion of small particles suspended in liquids at rest required by the molecular-kinetic theory of heat, https://api.semanticscholar.org/CorpusID:13642744

Faisal-Cury, A., Ziebold, C., de Oliveira Rodrigues, D. M., & Matijasevich, A., (2022), Depression underdiagnosis: prevalence and associated factors. a population-based study., *Journal of psychiatric research*, *151*, 157–165, https://api.semanticscholar.org/CorpusID:248450768

Fick, D. A., (1855), V. on liquid diffusion, *The London, Edinburgh, and Dublin Philosophical Magazine and Journal of Science*, *10 63*, 30–39, https://doi.org/10.1080/14786445508641925

Figalli, A., (2010), The optimal partial transport problem, *Arch Rational Mech Anal*, *195*, 533–560, https://doi.org/https://doi.org/10.1007/s00205-008-0212-7

Fillard, P., Descoteaux, M., Goh, A., Gouttard, S., Jeurissen, B., Malcolm, J. G., Ramírez-Manzanares, A., Reisert, M., Sakaie, K. E., Tensaouti, F., Yo, T.-S., Mangin, J. F., & Poupon, C., (2011), Quantitative evaluation of 10 tractography algorithms on a realistic diffusion mr phantom, *NeuroImage*, *56*, 220–234, https://api.semanticscholar.org/CorpusID:16405036

Fillard, P., Poupon, C., & Mangin, J. F., (2009), A novel global tractography algorithm based on an adaptive spin glass model, *Medical image computing and computer-assisted intervention : MICCAI ... International Conference on Medical Image Computing and Computer-Assisted Intervention*, *12 Pt 1*, 927–34, https://api.semanticscholar.org/CorpusID:19027190

Finger, S., (1994), Origins of neuroscience: a history of explorations into brain function., https://api.semanticscholar.org/CorpusID:81994797

Freedman, R., Lewis, D. A., Michels, R., Pine, D. S., Schultz, S. K., Tamminga, C. A., Gabbard, G. O., Gau, S. S.-F., Javitt, D. C., Oquendo, M. A., Shrout, P. E., Vieta, E., & Yager, J., (2013), The initial field trials of dsm-5: new blooms and old thorns., *The American journal of psychiatry*, *170 1*, 1–5, https://api.semanticscholar.org/CorpusID:34537713

Friedman, E., (1994), Cspt circuitry in affective disorders., *Biological psychiatry*, *36 3*, 208–9, https://api.semanticscholar.org/CorpusID:35089076

Friman, O., Farnebäck, G., & Westin, C.-F., (2006), A bayesian approach for stochastic white matter tractography, *IEEE Transactions on Medical Imaging*, *25*, 965–978, https://api.semanticscholar.org/CorpusID:2273989

Gao, Y., et al., (2013a), Validation of DTI tractography-based measures of primary motor area connectivity in the squirrel monkey brain, *PloS one*, *8*, https://doi.org/10.1371/journal.pone.0075065

Gao, Y., Choe, A. S., Stepniewska, I., Li, X., Avison, M. J., & Anderson, A. W., (2013b), Validation of dti tractography-based measures of primary motor area connectivity in the squirrel monkey brain, *PloS one*, *8 10*, e75065.

Garyfallidis, E., Brett, M., Correia, M. M., Williams, G. B., & Nimmo-Smith, I., (2012), Quickbundles, a method for tractography simplification, *Frontiers in Neuroscience*, *6*, https://api.semanticscholar.org/CorpusID:8151548

Garyfallidis, E., Côté, M.-A., Rheault, F., Sidhu, J., Hau, J., Petit, L., Fortin, D., Cunanne, S., & Descoteaux, M., (2017), Recognition of white matter bundles using local and global streamline-based registration and clustering, *NeuroImage*, *170*, 283–295, https://api.semanticscholar.org/CorpusID:4404688

Geeraert, B. L., Lebel, M. R., Mah, A., Deoni, S. C. L., Alsop, D. C., Varma, G., & Lebel, C. A., (2017), A comparison of inhomogeneous magnetization transfer, myelin volume fraction, and diffusion tensor imaging measures in healthy children, *NeuroImage*, *182*, 343–350, https://api.semanticscholar.org/CorpusID:31250991

Geng, X., Ross, T., Zhan, W., Gu, H., Chao, Y., Lin, C., Christensen, G., Schuff, N., & Yang, Y., (2009), Diffusion mri registration using orientation distribution functions., *IPMI*, *9*, 626–637.

Girard, G., et al., (2020a), On the cortical connectivity in the macaque brain: a comparison of diffusion tractography and histological tracing data, *NeuroImage*, *221*, 117201, https://doi.org/https://doi.org/10.1016/j.neuroimage.2020.117201

Girard, G., Caminiti, R., Battaglia-Mayer, A., St-Onge, E., Ambrosen, K. S., Eskildsen, S. F., Krug, K., Dyrby, T. B., Descoteaux, M., Thiran, J., & Innocenti, G. M., (2020b), On the cortical connectivity in the macaque brain: a comparison of diffusion tractography and histological tracing data, *NeuroImage*, *221*, 117201, https://doi.org/https://doi.org/10.1016/j.neuroimage.2020.117201

Girard, G., (2016), *Tractographie de la matière blanche orientée par apriori anatomiques et microstructurels* [Doctoral dissertation, Université de Sherbrooke, Université de Nice Sophia Antipolis].

Girard, G., Whittingstall, K., Deriche, R., & Descoteaux, M., (2014), Towards quantitative connectivity analysis: reducing tractography biases, *NeuroImage*, *98*, 266–278, https://api.semanticscholar.org/CorpusID:17681066

Global, regional, and national burden of 12 mental disorders in 204 countries and territories, 1990–2019: a systematic analysis for the global burden of disease study 2019, (2022), *The Lancet. Psychiatry*, *9*, 137–150, https://api.semanticscholar.org/CorpusID:245876054

Glozman, T., Bruckert, L., Pestilli, F., Yecies, D. W., Guibas, L. J., & Yeom, K. W., (2018), Framework for shape analysis of white matter fiber bundles, *NeuroImage*, *167*, 466–477, https://api.semanticscholar.org/CorpusID:3914335

Goh, A., Lenglet, C., Thompson, P., & Vidal, R., (2011), A nonparametric riemannian framework for processing high angular resolution diffusion images and its applications to odf-based morphometry, *NeuroImage*, *56 3*, 1181–1201.

Gössl, C., Fahrmeir, L., Pütz, B., Auer, L. M., & Auer, D. P., (2002), Fiber tracking from dti using linear state space models: detectability of the pyramidal tract, *NeuroImage*, *16 2*, 378–388.

Grehl, M. M., Hameed, S. K., & Murrough, J. W., (2023), Brain features of treatment-resistant depression: a review of structural and functional connectivity magnetic resonance imaging studies., *The Psychiatric clinics of North America*, *46 2*, 391–401, https://api.semanticscholar.org/CorpusID:257763910

Groeneweg-Koolhoven, I., Comijs, H. C., Naarding, P., de Waal, M. W. M., & van der Mast, R. C., (2016), Apathy in older persons with depression: course and predictors, *Journal of Geriatric Psychiatry and Neurology*, *29*, 178–186, https://api.semanticscholar.org/CorpusID:206570843

Guimond, A., Meunier, J., & Thirion, J., (2000), Average brain models: a convergence study, *Computer vision and image understanding*, *77 2*, 192–210.

Guo, W., Liu, F., Chen, J., Xu, X.-j., Wu, R.-r., Ma, C.-q., Gao, K., Tan, C., Sun, X.-l., Xiao, C.-q., Chen, H.-f., & Zhao, J., (2012), Altered white matter integrity of forebrain in treatment-resistant depression: a diffusion tensor imaging study with tract-based spatial statistics, *Progress in Neuro-Psychopharmacology and Biological Psychiatry*, *38*, 201–206, https://api.semanticscholar.org/CorpusID:41441690

Gupta, V., Thomopoulos, S. I., Rashid, F. M., & Thompson, P. M., (2017), Fibernet: an ensemble deep learning framework for clustering white matter fibers, *bioRxiv*, https://api.semanticscholar.org/CorpusID:40994309

Hagmann, P., Kurant, M., Gigandet, X., Thiran, P., Wedeen, V. J., Meuli, R. A., & Thiran, J.-P., (2007), Mapping human whole-brain structural networks with diffusion mri, *PLoS ONE*, *2*, https://api.semanticscholar.org/CorpusID:3177575

Hahn, E. L., (1950), Nuclear induction due to free larmor precession, *Physical Review*, *77*, 297–298, https://api.semanticscholar.org/CorpusID:92995835

Hansen, P. C., (1994), Regularization tools: a matlab package for analysis and solution of discrete ill-posed problems, *Numerical Algorithms*, *6*, 1–35, https://api.semanticscholar.org/CorpusID:2873360

Hasan, K. M., Parker, D. L., & Alexander, A. L., (2001), Comparison of gradient encoding schemes for diffusion-tensor mri, *Journal of Magnetic Resonance Imaging*, *13*, https://api.semanticscholar.org/CorpusID:25311834

Healy, D. M., Hendriks, H., & Kim, P. T., (1998), Spherical deconvolution, *Journal of Multivariate Analysis*, *67*, 1–22, https://api.semanticscholar.org/CorpusID:16886122

Herrman, H., Patel, V., Kieling, C., Berk, M., Buchweitz, C., Cuijpers, P., Furukawa, T. A., Kessler, R. C., Kohrt, B. A., Maj, M., McGorry, P. D., Reynolds, C. F., Weissman, M. M., Chibanda, D., Dowrick, C., Howard, L. M., Hoven, C. W., Knapp, M., Mayberg, H. S., ... Wolpert, M., (2022), Time for united action on depression: a lancet–world psychiatric association commission, *The Lancet*, *399*, 957–1022, https://api.semanticscholar.org/CorpusID:246830234

Hosey, T. P., Williams, G. B., & Ansorge, R. E., (2005), Inference of multiple fiber orientations in high angular resolution diffusion imaging, *Magnetic Resonance in Medicine*, *54*, https://api.semanticscholar.org/CorpusID:1912561

Iglesias, J. E., & Sabuncu, M. R., (2014), Multi-atlas segmentation of biomedical images: a survey, *Medical image analysis*, *24 1*, 205–219, https://api.semanticscholar.org/CorpusID:3644401

Iturria-medina, Y., Sotero, R. C., Canales-Rodríguez, E. J., Alemán-Gómez, Y., & Melie-García, L., (2008), Studying the human brain anatomical network via diffusion-weighted mri and graph theory, *NeuroImage*, *40*, 1064–1076, https://api.semanticscholar.org/CorpusID:3593098

Jbabdi, S., & Johansen-Berg, H., (2011a), Tractography: where do we go from here?, *Brain connectivity*, *1 3*, 169–183.

Jbabdi, S., Woolrich, M. W., Andersson, J. L., & Behrens, T., (2007), A bayesian framework for global tractography, *Neuroimage*, *371*, 116–129.

Jbabdi, S., Bellec, P., Toro, R., Daunizeau, J., Pélégrini-Issac, M., & Benali, H., (2007), Accurate anisotropic fast marching for diffusion-based geodesic tractography, *International Journal of Biomedical Imaging*, *2008*, https://api.semanticscholar.org/CorpusID:2298930

Jbabdi, S., & Johansen-Berg, H., (2011b), Tractography: where do we go from here?, *Brain connectivity*, *1 3*, 169–83, https://api.semanticscholar.org/CorpusID:13899117

Jeurissen, B., Descoteaux, M., Mori, S., & Leemans, A., (2019a), Diffusion mri fiber tractography of the brain, *NMR in Biomedicine*, *32 4*, e3785.

Jeurissen, B., Leemans, A., Jones, D., Tournier, J., & Sijbers, J., (2011), Probabilistic fiber tracking using the residual bootstrap with constrained spherical deconvolution, *Human brain mapping*, *32 3*, 461–479.

Jeurissen, B., Tournier, J., Dhollander, T., Connelly, A., & Sijbers, J., (2014), Multi-tissue constrained spherical deconvolution for improved analysis of multi-shell diffusion mri data, *NeuroImage*, *103*, 411–426.

Jeurissen, B., (2012), *Improved analysis of brain connectivity using high angular resolution diffusion mri* [Doctoral dissertation, University of Antwerp].

Jeurissen, B., Descoteaux, M., Mori, S., & Leemans, A., (2019b), Diffusion mri fiber tractography of the brain, *NMR in Biomedicine*, *32*, https://api.semanticscholar.org/CorpusID:8463236

Jeurissen, B., Leemans, A., Jones, D. K., Tournier, J.-D., & Sijbers, J., (2011), Probabilistic fiber tracking using the residual bootstrap with constrained spherical deconvolution, *Human Brain Mapping*, *32*, https://api.semanticscholar.org/CorpusID:20852380

Jeurissen, B., Tournier, J.-D., Dhollander, T., Connelly, A., & Sijbers, J., (2014), Multi-tissue constrained spherical deconvolution for improved analysis of multi-shell diffusion mri data, *NeuroImage*, *103*, 411–426, https://api.semanticscholar.org/CorpusID:4722162

Johansen-Berg, H., & Behrens, T. E. J., (2014), Diffusion mri : from quantitative measurement to in vivo neuroanatomy, https://api.semanticscholar.org/CorpusID:108302378

Johansen-Berg, H., & Rushworth, M. F. S., (2009), Using diffusion imaging to study human connectional anatomy., *Annual review of neuroscience*, *32*, 75–94, https://api.semanticscholar.org/CorpusID:8177064

Jolliffe, I. T., & Cadima, J., (2016), Principal component analysis: a review and recent developments, *Philosophical Transactions of the Royal Society A: Mathematical, Physical and Engineering Sciences*, *374*, https://api.semanticscholar.org/CorpusID:20101754

Jones, D. K., (2008a), Tractography gone wild: probabilistic fibre tracking using the wild bootstrap with diffusion tensor MRI, *IEEE Transactions on Medical Imaging*, *27 9*, 1268–1274, https://doi.org/10.1109/TMI.2008.922191

Jones, D. K., (2003), Determining and visualizing uncertainty in estimates of fiber orientation from diffusion tensor mri, *Magnetic Resonance in Medicine*, *49*, https://api.semanticscholar.org/CorpusID:7416841

Jones, D. K., (2008b), Tractography gone wild: probabilistic fibre tracking using the wild bootstrap with diffusion tensor mri, *IEEE Transactions on Medical Imaging*, *27*, 1268–1274, https://api.semanticscholar.org/CorpusID:26035446

Jones, D. K., Horsfield, M. A., & Simmons, A., (1999), Optimal strategies for measuring diffusion in anisotropic systems by magnetic resonance imaging, *Magnetic Resonance in Medicine: An Official Journal of the International Society for Magnetic Resonance in Medicine*, *42 3*, 515–525.

Jones, D. K., PhD, (2010), *Diffusion MRI: Theory, Methods, and Applications*, Oxford University Press, https://doi.org/10.1093/med/9780195369779.001.0001

Jones, D. K., & Pierpaoli, C., (2005), Confidence mapping in diffusion tensor magnetic resonance imaging tractography using a bootstrap approach, *Magnetic Resonance in Medicine*, *53*, https://api.semanticscholar.org/CorpusID:5683748

Jones, D. K., Travis, A. R., Eden, G., Pierpaoli, C., & Basser, P. J., (2005), Pasta: pointwise assessment of streamline tractography attributes, *Magnetic Resonance in Medicine*, *53*, https://api.semanticscholar.org/CorpusID:14771916

Jones, D., (2010), *Diffusion mri: theory, methods, and applications*, Oxford University Press.

Jörgens, D., Descoteaux, M., & Moreno, R., (2021), Challenges for tractogram filtering, *Mathematics and Visualization*, https://api.semanticscholar.org/CorpusID:234278447

Kaden, E., Knösche, T. R., & Anwander, A., (2007), Parametric spherical deconvolution: inferring anatomical connectivity using diffusion mr imaging, *NeuroImage*, *37*, 474–488, https://api.semanticscholar.org/CorpusID:3210797

Kennis, M., Gerritsen, L., van Dalen, M., Williams, A. D., Cuijpers, P., & Bockting, C. L. H., (2019), Prospective biomarkers of major depressive disorder: a systematic review and meta-analysis, *Molecular Psychiatry*, *25*, 321–338, https://api.semanticscholar.org/CorpusID:208171859

Khatami, M., Schmidt-Wilcke, T., Sundgren, P. C., Abbasloo, A., Scholkopf, B., & Schultz, T., (2017), Bundlemap: anatomically localized classification, regression, and hypothesis testing in diffusion mri, *Pattern Recognit.*, *63*, 593–600, https://api.semanticscholar.org/CorpusID:29003058

Koay, C. G., Chang, L.-C., Carew, J. D., Pierpaoli, C., & Basser, P. J., (2006), A unifying theoretical and algorithmic framework for least squares methods of estimation in diffusion tensor imaging., *Journal of magnetic resonance*, *182 1*, 115–25, https://api.semanticscholar.org/CorpusID:6486567

Korgaonkar, M. S., Grieve, S. M., Koslow, S. H., Gabrieli, J. D. E., Gordon, E., & Williams, L. M., (2011), Loss of white matter integrity in major depressive disorder: evidence using tract-based spatial statistical analysis of diffusion tensor imaging, *Human Brain Mapping*, *32*, https://api.semanticscholar.org/CorpusID:21104606

Kreher, B. W., Mader, I., & Kiselev, V. G., (2008), Gibbs tracking: a novel approach for the reconstruction of neuronal pathways, *Magnetic Resonance in Medicine*, *60*, https://api.semanticscholar.org/CorpusID:18526357

Kreis, R., Ernst, T., & Ross, B. D., (1993), Absolute quantitation of water and metabolites in the human brain. ii. metabolite concentrations, *Journal of Magnetic Resonance, Series B*, *102*, 9–19, https://api.semanticscholar.org/CorpusID:97873748

Kronlage, M., Pitarokoili, K., Schwarz, D., Godel, T., Heiland, S., Yoon, M.-S., Bendszus, M., & Bäumer, P., (2017), Diffusion tensor imaging in chronic inflammatory demyelinating polyneuropathy: diagnostic accuracy and correlation with electrophysiology, *Investigative Radiology*, *52*, 701–707, https://api.semanticscholar.org/CorpusID:21204808

Lam, P. D. N., Belhomme, G., Ferrall, J., Patterson, B., Styner, M., & Prieto, J. C., (2018), Trafic: fiber tract classification using deep learning, *Medical Imaging*, https://api.semanticscholar.org/CorpusID:3763068

Landman, B. A., Farrell, J. A. D., Jones, C. K., Smith, S. A., Prince, J. L., & Mori, S., (2007), Effects of diffusion weighting schemes on the reproducibility of dti-derived fractional anisotropy, mean diffusivity, and principal eigenvector measurements at 1.5t, *NeuroImage*, *36*, 1123–1138, https://api.semanticscholar.org/CorpusID:9239168

Lazar, M., Weinstein, D., Tsuruda, J., Hasan, K., Arfanakis, K., Meyerand, M., Badie, B., Rowley, H., Haughton, V., Field, A., et al., (2003), White matter tractography using diffusion tensor deflection, *Human brain mapping*, *18 4*, 306–321.

Lazar, M., Weinstein, D. M., Tsuruda, J. S., Hasan, K. M., Arfanakis, K., Meyerand, M. E., Badie, B., Rowley, H. A., Haughton, V., Field, A. S., & Alexander, A. L., (2003), White matter tractography using diffusion tensor deflection, *Human Brain Mapping*, *18*, https://api.semanticscholar.org/CorpusID:1696861

Lebel, C. A., Treit, S., & Beaulieu, C., (2019), A review of diffusion mri of typical white matter development from early childhood to young adulthood, *NMR in Biomedicine*, *32*, https://api.semanticscholar.org/CorpusID:24739220

Lenglet, C., Deriche, R., & Faugeras, O. D., (2004), Inferring white matter geometry from di.usion tensor mri: application to connectivity mapping, *European Conference on Computer Vision*, https://api.semanticscholar.org/CorpusID:16478008

Lentner, C., (1981), Units of measurement, body fluids, composition of the body, nutrition, https://api.semanticscholar.org/CorpusID:92684882

Lythgoe, M. F., Busza, A. L., Calamante, F., Sotak, C. H., King, M. D., Bingham, A. C., Williams, S. R., & Gadian, D. G., (1997), Effects of diffusion anisotropy on lesion delineation in a rat model of cerebral ischemia, *Magnetic Resonance in Medicine*, *38*, https://api.semanticscholar.org/CorpusID:22937479

Maffei, C., Girard, G., Schilling, K., Adluru, N., Aydogan, D. B., Hamamci, A., Yeh, F.-C., Mancini, M., Wu, Y., Sarica, A., Teillac, A., Baete, S., Karimi, D., Lin, Y.-C., Boada, F., Richard, N., Hiba, B., Quattrone, A., Hong, Y., & Yendik, A., (2020), The irontract challenge: validation and optimal tractography methods for the hcp diffusion acquisition scheme.

Maier-Hein, K., et al., (2017a), The challenge of mapping the human connectome based on diffusion tractography, *Nat Commun 8*, *1349*, https://doi.org/10.1038/s41467-017-01285-x

Maier-Hein, K. H., Neher, P., Houde, J., Côté, M., Garyfallidis, E., Zhong, J., Chamberland, M., Yeh, F., Lin, Y., Ji, Q., et al., (2017), The challenge of mapping the human connectome based on diffusion tractography, *Nature communications*, *8 1*, 1–13.

Maier-Hein, K., Neher, P., Houde, J.-C., Côté, M.-A., Garyfallidis, E., Zhong, J., Chamberland, M., Yeh, F.-C., Lin, Y.-C., Ji, Q., Reddick, W. E., Glass, J. O., Chen, D. Q., Feng, Y., Gao, C., Wu, Y., Ma, J., Renjie, H., Li, Q., ... Descoteaux, M., (2017b), The challenge of mapping the human connectome based on diffusion tractography, *Nature Communications*, *8*, https://api.semanticscholar.org/CorpusID:205551582

Mallat, S., (1989), A theory for multiresolution signal decomposition: the wavelet representation, *IEEE Trans. Pattern Anal. Mach. Intell.*, *11*, 674–693, https://api.semanticscholar.org/CorpusID:2356353

Mancini, M., Vos, S. B., Vakharia, V. N., O'Keeffe, A. G., Trimmel, K., Barkhof, F., Dorfer, C., Soman, S., Winston, G. P., Wu, C., et al., (2019), Automated fiber tract reconstruction for surgery planning: extensive validation in language-related white matter tracts, *NeuroImage: Clinical*, *23*, 101883.

Mangin, J. F., Fillard, P., Cointepas, Y., Bihan, D. L., Frouin, V., & Poupon, C., (2013), Toward global tractography, *NeuroImage*, *80*, 290–296, https://api.semanticscholar.org/CorpusID:12634823

Mehrotra, S., (1992), On the implementation of a primal-dual interior point method, *SIAM J. Optim.*, *2*, 575–601, https://api.semanticscholar.org/CorpusID:7845529

Merlet, S., Philippe, A.-C., Deriche, R., & Descoteaux, M., (2012), Tractography via the ensemble average propagator in diffusion mri, *Medical image computing and computer-assisted intervention : MICCAI ... International Conference on Medical Image Computing and Computer-Assisted Intervention*, *15 Pt 2*, 339–46, https://api.semanticscholar.org/CorpusID:215813485

Meshkat, S., Alnefeesi, Y., Jawad, M. Y., Vincenzo, J. D. D., Rodrigues, N. B., Ceban, F., Lui, L. M. W., McIntyre, R. S., & Rosenblat, J. D., (2022), Brain-derived neurotrophic factor (bdnf) as a biomarker of treatment response in patients with treatment resistant depression (trd): a systematic review & meta-analysis, *Psychiatry Research*, *317*, https://api.semanticscholar.org/CorpusID:252402970

Metin, M., & Gökçay, D., (2021), Diffusion tensor imaging group analysis using tract profiling and directional statistics, *Frontiers in Neuroscience*, *15*, https://api.semanticscholar.org/CorpusID:232291524

Mirzaalian, H., de Pierrefeu, A., Savadjiev, P., Pasternak, O., Bouix, S., Kubicki, M., Westin, C.-F., Shenton, M. E., & Rathi, Y., (2015), Harmonizing diffusion mri data across multiple sites and scanners, *Medical image computing and computer-assisted intervention : MICCAI ... International Conference on Medical Image Computing and Computer-Assisted Intervention*, *9349*, 12–19, https://api.semanticscholar.org/CorpusID:9301233

Mori, S., et al., (2002), Fiber tracking: principles and strategies – a technical review, *NMR in Biomedicine*, *15 7-8*, 468–480, https://doi.org/https://doi.org/10.1002/nbm.781

Mori, S., & Van Zijl, P., (2002), Fiber tracking: principles and strategies–a technical review, *NMR in Biomedicine: An International Journal Devoted to the Development and Application of Magnetic Resonance In Vivo*, *15 7-8*, 468–480.

Mori, S., Crain, B., Chacko, V. P., & van Zijl, P. C. M., (1999), Three-dimensional tracking of axonal projections in the brain by magnetic resonance imaging, *Annals of Neurology*, *45*, https://api.semanticscholar.org/CorpusID:334903

Neher, P., Gotz, M., Norajitra, T., Weber, C., & Maier-Hein, K., (2015), A machine learning based approach to fiber tractography using classifier voting, *International Conference on Medical Image Computing and Computer-Assisted Intervention*, 45–52.

Nichols, T. E., & Holmes, A., (2002), Nonparametric permutation tests for functional neuroimaging: a primer with examples, *Human Brain Mapping*, *15*, https://api.semanticscholar.org/CorpusID:1428586

O'Donnell, L. J., & Westin, C.-F., (2011), An introduction to diffusion tensor image analysis., *Neurosurgery clinics of North America*, *22 2*, 185–96, viii, https://api.semanticscholar.org/CorpusID:27425023

Oguz, I., Boucharin, A., Lu, W., Vachet, C., Budin, F., Shi, Y., & Styner, M., (2012), A minimum cost approach to connectivity from orientation distribution functions via efficient multi-directional graph propagation, https://api.semanticscholar.org/CorpusID:31180754

Organization, W. H., (2017), *Depression and other common mental disorders: global health estimates* (Technical documents).

Parker, G. J. M., Haroon, H. A., & Wheeler-Kingshott, C. A. M., (2003), A framework for a streamline-based probabilistic index of connectivity (pico) using a structural interpretation of mri diffusion measurements, *Journal of Magnetic Resonance Imaging*, *18*, https://api.semanticscholar.org/CorpusID:2297263

Parker, G. J. M., Stephan, K. E., Barker, G. J., Rowe, J. B., MacManus, D. G., Wheeler-Kingshott, C. A. M., Ciccarelli, O., Passingham, R. E., Spinks, R. L., Lemon, R. N., & Turner, R., (2002), Initial demonstration of in vivo tracing of axonal projections in the macaque brain and comparison with the human brain using diffusion tensor imaging and fast marching tractography, *NeuroImage*, *15*, 797–809, https://api.semanticscholar.org/CorpusID:13926071

Pasternak, O., Sochen, N. A., Gur, Y., Intrator, N., & Assaf, Y., (2009), Free water elimination and mapping from diffusion mri, *Magnetic Resonance in Medicine*, *62*, https://api.semanticscholar.org/CorpusID:13940138

Pestilli, F., Yeatman, J. D., Rokem, A. S., Kay, K. N., & Wandell, B. A., (2014), Evaluation and statistical inference for living connectomes, *Nature methods*, *11*, 1058–1063, https://api.semanticscholar.org/CorpusID:14414107

Petit, L., Rheault, F., Descoteaux, M., & Tzourio-mazoyer, N., (2021), Half of the streamlines built in a whole human brain tractogram is anatomically uninterpretable., *F1000Research*, *10*, https://api.semanticscholar.org/CorpusID:240518600

Pichon, E., Westin, C.-F., & Tannenbaum, A. R., (2005), A hamilton-jacobi-bellman approach to high angular resolution diffusion tractography, *Medical image computing and computer-assisted intervention : MICCAI ... International Conference on Medical Image Computing and Computer-Assisted Intervention*, *8 Pt 1*, 180–7, https://api.semanticscholar.org/CorpusID:11521341

Pontabry, J., Rousseau, F., Oubel, E., Studholme, C., Koob, M., & Dietemann, J., (2013), Probabilistic tractography using q-ball imaging and particle filtering: application to adult and in-utero fetal brain studies, *Medical image analysis*, *17 3*, 297–310.

Pontabry, J., & Rousseau, F., (2011), Probabilistic tractography using q-ball modeling and particle filtering, *Medical image computing and computer-assisted intervention : MICCAI ... International Conference on Medical Image Computing and Computer-Assisted Intervention*, *14 Pt 2*, 209–16, https://api.semanticscholar.org/CorpusID:16493979

Poulin, P., Jörgens, D., Jodoin, P., & Descoteaux, M., (2019), Tractography and machine learning: current state and open challenges, *Magnetic resonance imaging*, *64*, 37–48.

Poupon, C., (1999), Detection des faisceaux de fibres de la substance blanche pour l'etude de la connectivite anatomique cerebrale, https://api.semanticscholar.org/CorpusID:171689546

Pujol, S., Wells, W., Pierpaoli, C., Brun, C. C., Gee, J. C., Cheng, G., Vemuri, B. C., Commowick, O., Prima, S., Stamm, A., Goubran, M., Khan, A. R., Peters, T. M., Neher, P., Maier-Hein, K., Shi, Y., Tristán-Vega, A., Veni, G., Whitaker, R. T., ... Kikinis, R., (2015), The dti challenge: toward standardized evaluation of diffusion tensor imaging tractography for neurosurgery, *Journal of Neuroimaging*, *25*, https://api.semanticscholar.org/CorpusID:1737596

Purcell, E. M., Torrey, H. C., & Pound, R. V., (1946), Resonance absorption by nuclear magnetic moments in a solid, *Physical Review*, *69*, 37–38, https://api.semanticscholar.org/CorpusID:120462648

Radon, J., (1917), Über die Bestimmung von Funktionen durch ihre Integralwerte längs gewisser Mannigfaltigkeiten, *Akad. Wiss.*, *69*, 262–277.

Rafael-Patino, J., Girard, G., Truffet, R., Pizzolato, M., Caruyer, E., & Thiran, J., (2021a), The diffusion-simulated connectivity (disco) dataset, *Data in Brief*, *38*, 107429.

Rafael-Patino, J., Girard, G., Truffet, R., Pizzolato, M., Caruyer, E., & Thiran, J., (2021b), The diffusion-simulated connectivity (disco) dataset, *Data in Brief*, *38*, 107429, https://doi.org/https://doi.org/10.1016/j.dib.2021.107429

Raffelt, D., Tournier, J., Crozier, S., Connelly, A., & Salvado, O., (2012), Reorientation of fiber orientation distributions using apodized point spread functions, *Magnetic Resonance in Medicine*, *673*, 844–855.

Raffelt, D., Tournier, J.-D., Rose, S. E., Ridgway, G. R., Henderson, R. D., Crozier, S., Salvado, O., & Connelly, A., (2012), Apparent fibre density: a novel measure for the analysis of diffusion-weighted magnetic resonance images, *NeuroImage*, *59*, 3976–3994, https://api.semanticscholar.org/CorpusID:335054

Reisert, M., Mader, I., Anastasopoulos, C., Weigel, M., Schnell, S., & Kiselev, V. G., (2011), Global fiber reconstruction becomes practical, *NeuroImage*, *54*, 955–962, https://api.semanticscholar.org/CorpusID:27723448

Rheault, F., Houde, J., & Descoteaux, M., (2017), Visualization, interaction and tractometry: dealing with millions of streamlines from diffusion mri tractography, *Frontiers in neuroinformatics*, *11*, 42.

Rheault, F., St-Onge, E., Sidhu, J., Maier-Hein, K., Tzourio-Mazoyer, N., Petit, L., & Descoteaux, M., (2019), Bundle-specific tractography with incorporated anatomical and orientational priors, *NeuroImage*, *186*, 382–398.

Rheault, F., Poulin, P., Caron, A. V., St-Onge, E., & Descoteaux, M., (2020), Common misconceptions, hidden biases and modern challenges of dmri tractography, *Journal of Neural Engineering*, *17*, https://api.semanticscholar.org/CorpusID:210194725

Roine, T., Jeurissen, B., Perrone, D. J., Aelterman, J., Leemans, A., Philips, W., & Sijbers, J., (2014), Isotropic non-white matter partial volume effects in constrained spherical deconvolution, *Frontiers in Neuroinformatics*, *8*, https://api.semanticscholar.org/CorpusID:6250010

Rush, A. J., Trivedi, M. H., Wisniewski, S. R., Nierenberg, A. A., Stewart, J. W., Warden, D., Niederehe, G., Thase, M. E., Lavori, P. W., Lebowitz, B., McGrath, P. J., Rosenbaum, J. F., Sackeim, H. A., Kupfer, D. J., Luther, J., & Fava, M., (2006),

Acute and longer-term outcomes in depressed outpatients requiring one or several treatment steps: a star*d report., *The American journal of psychiatry*, *163 11*, 1905–17, https://api.semanticscholar.org/CorpusID:36121981

Sarica, A., Cerasa, A., Valentino, P., Yeatman, J. D., Trotta, M., Barone, S., Granata, A., Nisticó, R., Perrotta, P., Pucci, F., & Quattrone, A., (2017), The corticospinal tract profile in amyotrophic lateral sclerosis, *Human Brain Mapping*, *38*, https://api.semanticscholar.org/CorpusID:1447703

Savadjiev, P., Campbell, J. S. W., Pike, G. B., & Siddiqi, K., (2006), 3d curve inference for diffusion mri regularization and fibre tractography, *Medical image analysis*, *10 5*, 799–813, https://api.semanticscholar.org/CorpusID:8676610

Scherrer, B., & Warfield, S., (2012), Parametric representation of multiple white matter fascicles from cube and sphere diffusion mri, *PloS one*, *7*, e48232, https://doi.org/10.1371/journal.pone.0048232

Schiavi, S., Ocampo-Pineda, M., Barakovic, M., Petit, L., Descoteaux, M., Thiran, J.-P., & Daducci, A., (2020), A new method for accurate in vivo mapping of human brain connections using microstructural and anatomical information, *Science Advances*, *6*, https://api.semanticscholar.org/CorpusID:220939372

Schilling, K. G., et al., (2021a), Tractography dissection variability: what happens when 42 groups dissect 14 white matter bundles on the same dataset?, *NeuroImage*, *243*, 118502, https://doi.org/https://doi.org/10.1016/j.neuroimage.2021.118502

Schilling, K. G., et al., (2021b), Tractography dissection variability: what happens when 42 groups dissect 14 white matter bundles on the same dataset?, *NeuroImage*, *243*, 118502, https://doi.org/https://doi.org/10.1016/j.neuroimage.2021.118502

Schreiber, J., Riffert, T. W., Anwander, A., & Knösche, T. R., (2014), Plausibility tracking: a method to evaluate anatomical connectivity and microstructural properties along fiber pathways, *NeuroImage*, *90*, 163–178, https://api.semanticscholar.org/CorpusID:13406318

Schurr, R., Duan, Y., Norcia, A. M., Ogawa, S., Yeatman, J. D., & Mezer, A. A., (2018), Tractography optimization using quantitative t1 mapping in the human optic radiation, *NeuroImage*, *181*, 645–658, https://api.semanticscholar.org/CorpusID:49413674

Sepasian, N., (2011), Multi-valued geodesic tractography for diffusion weighted imaging, https://api.semanticscholar.org/CorpusID:94678207

Serafini, G., Pompili, M., Borgwardt, S. J., Giuffra, E., Howes, O. D., Girardi, P., & Amore, M., (2015), The role of white matter abnormalities in treatment-resistant depression: a systematic review., *Current pharmaceutical design*, *21 10*, 1337–46, https://api.semanticscholar.org/CorpusID:36172675

Seunarine, K. K., Cook, P. A., Hall, M. G., Embleton, K. V., Parker, G. J. M., & Alexander, D. C., (2007), Exploiting peak anisotropy for tracking through complex structures, *2007 IEEE 11th International Conference on Computer Vision*, 1–8, https://api.semanticscholar.org/CorpusID:2058931

Smith, R. E., et al., (2012), Anatomically-constrained tractography: improved diffusion MRI streamlines tractography through effective use of anatomical information, *NeuroImage*, *62 3*, 1924–1938, https://doi.org/https://doi.org/10.1016/j.neuroimage.2012.06.005

Smith, R., Tournier, J., Calamante, F., & Connelly, A., (2015), Sift2: enabling dense quantitative assessment of brain white matter connectivity using streamlines tractography, *NeuroImage*, *119*, 338–351, https://doi.org/https://doi.org/10.1016/j.neuroimage.2015.06.092

Smith, R. E., Connelly, A., & Calamante, F., (2020), Diffusion mri fiber tractography, https://api.semanticscholar.org/CorpusID:235068230

Smith, R. E., Tournier, J.-D., Calamante, F., & Connelly, A., (2013), Sift: spherical-deconvolution informed filtering of tractograms, *NeuroImage*, *67*, 298–312, https://api.semanticscholar.org/CorpusID:6282046

Smith, R. E., Tournier, J.-D., Calamante, F., & Connelly, A., (2015), Sift2: enabling dense quantitative assessment of brain white matter connectivity using streamlines tractography, *NeuroImage*, *119*, 338–351, https://api.semanticscholar.org/CorpusID:19656480

Smith, S. M., Jenkinson, M., Johansen-Berg, H., Rueckert, D., Nichols, T. E., Mackay, C. E., Watkins, K. E., Ciccarelli, O., Cader, M. Z., Matthews, P. M., & Behrens, T. E. J., (2006), Tract-based spatial statistics: voxelwise analysis of multi-subject diffusion data, *NeuroImage*, *31*, 1487–1505, https://api.semanticscholar.org/CorpusID:7133484

Solomon, J., et al., (2015), Convolutional wasserstein distances: efficient optimal transportation on geometric domains, *ACM Trans. Graph.*, *34 4*, https://doi.org/10.1145/2766963

Sotiropoulos, S. N., Bai, L., Morgan, P. S., Constantinescu, C. S., & Tench, C. R., (2010a), Brain tractography using q-ball imaging and graph theory: improved connectivities through fibre crossings via a model-based approach, *Neuroimage*, *49 3*, 2444–2456.

Sotiropoulos, S. N., Bai, L., Morgan, P. S., Constantinescu, C. S., & Tench, C. R., (2010b), Brain tractography using q-ball imaging and graph theory: improved connectivities through fibre crossings via a model-based approach, *NeuroImage*, *49*, 2444–2456, https://api.semanticscholar.org/CorpusID:31461350

Stamm, A., et al., (2013), Adaptive multi-modal particle filtering for probabilistic white matter tractography, *Information Processing in Medical Imaging.*, 594–606, https://doi.org/0.1007/978-3-642-38868-2_50

Stamm, A., Commowick, O., Barillot, C., & Perez, P., (2013), Adaptive multi-modal particle filtering for probabilistic white matter tractography, *International Conference on Information Processing in Medical Imaging*, 594–606.

Stamm, A., Commowick, O., Barillot, C., & Pérez, P., (2013a), Adaptive multi-modal particle filtering for probabilistic white matter tractography, *Information Processing in Medical Imaging: 23rd International Conference, IPMI 2013, Asilomar, CA, USA, June 28–July 3, 2013. Proceedings 23*, 594–606.

Stamm, A., Commowick, O., Barillot, C., & Pérez, P., (2013b), Adaptive multi-modal particle filtering for probabilistic white matter tractography, *Information processing in medical imaging : proceedings of the ... conference*, *23*, 594–606, https://api.semanticscholar.org/CorpusID:14779613

Starck, J.-L., Donoho, D. L., & Candès, E. J., (2003), Astronomical image representation by the curvelet transform, *Astronomy & Astrophysics*, *398*, 785–800, https://api.semanticscholar.org/CorpusID:14532201

Steffens, D. C., Fahed, M., Manning, K. J., & Wang, L., (2022), The neurobiology of apathy in depression and neurocognitive impairment in older adults: a review of epidemiological, clinical, neuropsychological and biological research, *Translational Psychiatry*, *12*, https://api.semanticscholar.org/CorpusID:255175999

Stejskal, E. O., & Tanner, J. E., (1965), Spin diffusion measurements : spin echoes in the presence of a time-dependent field gradient, *Journal of Chemical Physics*, *42*, 288–292, https://api.semanticscholar.org/CorpusID:8566948

Stejskal, E., & Tanner, J., (1965), Spin diffusion measurements: spin echoes in the presence of a time-dependent field gradient, *The journal of chemical physics*, *42 1*, 288–292.

Suarez, R., Commowick, O., Prabhu, S., & Warfield, S., (2012), Automated delineation of white matter fiber tracts with a multiple region-of-interest approach, *Neuroimage*, *59 4*, 3690–3700.

Sun, J.-f., Ma, Y., Guo, C.-l., Du, Z.-d., Chen, L.-m., Wang, Z., Li, X., Xu, K., Luo, Y., Hong, Y., Yu, X., Xiao, X., Fang, J., & Lu, J., (2022), Distinct patterns of functional brain network integration between treatment-resistant depression and non treatment-resistant depression: a resting-state functional magnetic resonance imaging study, *Progress in Neuro-Psychopharmacology and Biological Psychiatry*, *120*, https://api.semanticscholar.org/CorpusID:251867414

Tax, C. M. W., Haije, T. D., Fuster, A., Westin, C.-F., Viergever, M. A., Florack, L., & Leemans, A., (2016), Sheet probability index (spi): characterizing the geometrical organization of the white matter with diffusion mri, *NeuroImage*, *142*, 260–279, https://api.semanticscholar.org/CorpusID:24790131

Tej., B., Sotiropoulos, S. N., & Jbabdi, S., (2009), Mr diffusion tractography, https://api.semanticscholar.org/CorpusID:148645040

Toh, B., Wang, X., Keeble, J., Sim, W. J., Khoo, K., Wong, W.-C., Kato, M., Prévost-Blondel, A., Thiery, J. P., & Abastado, J. P., (2011), Mesenchymal transition and dissemination of cancer cells is driven by myeloid-derived suppressor cells infiltrating the primary tumor, *PLoS Biology*, *9*, https://api.semanticscholar.org/CorpusID:6854321

Tournier, J.-D., Calamante, F., & Connelly, A., (2005), Improved characterisation of crossing fibres: spherical deconvolution combined with tikhonov regularization, https://api.semanticscholar.org/CorpusID:225101508

Tournier, J.-D., Calamante, F., & Connelly, A., (2007), Robust determination of the fibre orientation distribution in diffusion mri: non-negativity constrained super-resolved spherical deconvolution, *NeuroImage*, *35*, 1459–1472, https://api.semanticscholar.org/CorpusID:30217586

Tournier, J.-D., Calamante, F., & Connelly, A., (2010a), Effect of step size on probabilistic streamlines : implications for the interpretation of connectivity analyses, https://api.semanticscholar.org/CorpusID:34010371

Tournier, J.-D., Calamante, F., & Connelly, A., (2012), Mrtrix: diffusion tractography in crossing fiber regions, *International Journal of Imaging Systems and Technology*, *22*, https://api.semanticscholar.org/CorpusID:11336177

Tournier, J.-D., Calamante, F., Gadian, D. G., & Connelly, A., (2004), Direct estimation of the fiber orientation density function from diffusion-weighted mri data using spherical deconvolution, *NeuroImage*, *23*, 1176–1185, https://api.semanticscholar.org/CorpusID:24169627

Tournier, J.-D., Yeh, C.-H., Calamante, F., Cho, K.-H., Connelly, A., & Lin, C.-P., (2008), Resolving crossing fibres using constrained spherical deconvolution: validation using diffusion-weighted imaging phantom data, *NeuroImage*, *42*, 617–625, https://api.semanticscholar.org/CorpusID:18967334

Tournier, J.-D., et al., (2010b), Improved probabilistic streamlines tractography by 2nd order integration over fibre orientation distributions, *Proceedings of the ISMRM*, *1670*, https://doi.org/10.1038/s41467-017-01285-x

Tournier, J., Calamante, F., & Connelly, A., (2007), Robust determination of the fibre orientation distribution in diffusion mri: non-negativity constrained super-resolved spherical deconvolution, *NeuroImage*, *354*, 1459–1472, https://doi.org/https://doi.org/10.1016/j.neuroimage.2007.02.016

Tournier, J., Calamante, F., Connelly, A., et al., (2010), Improved probabilistic streamlines tractography by 2nd order integration over fibre orientation distributions, *Proceedings of the international society for magnetic resonance in medicine*, *1670*.

Tournier, J., Smith, R., Raffelt, D., Tabbara, R., Dhollander, T., Pietsch, M., Christiaens, D., Jeurissen, B., Yeh, C., & Connelly, A., (2019), Mrtrix3: a fast, flexible and open software framework for medical image processing and visualisation, *NeuroImage*, *202*, 116137, https://doi.org/https://doi.org/10.1016/j.neuroimage.2019.116137

Tu, T.-W., Williams, R. A., Lescher, J. D., Jikaria, N., Turtzo, L. C., & Frank, J. A., (2016), Radiological–pathological correlation of diffusion tensor and magnetization transfer imaging in a closed head traumatic brain injury model, *Annals of Neurology*, *79*, https://api.semanticscholar.org/CorpusID:21630965

Tuch, D. S., (2004), Q-ball imaging, *Magnetic Resonance in Medicine*, *52*, https://api.semanticscholar.org/CorpusID:1368461

Tuch, D. S., Belliveau, J. W., & Wedeen, V. J., (2000), A path inte-gral approach to white matter tractography, https://api.semanticscholar.org/CorpusID:115620634

Tuch, D. S., Reese, T. G., Wiegell, M. R., Makris, N., Belliveau, J. W., & Wedeen, V. J., (2002), High angular resolution diffusion imaging reveals intravoxel white matter fiber heterogeneity, *Magnetic Resonance in Medicine*, *48*, https://api.semanticscholar.org/CorpusID:2048187

Tuch, D. S., Reese, T. G., Wiegell, M. R., & Wedeen, V. J., (2003), Diffusion mri of complex neural architecture, *Neuron*, *40*, 885–895, https://api.semanticscholar.org/CorpusID:18068745

Tuch, D., et al., (2002), High angular resolution diffusion imaging reveals intravoxel white matter fiber heterogeneity, *Magn Reson Med.*, *48(4)*, 577–82, https://doi.org/10.1002/mrm.10268.PMID:12353272.

van Dalen, J. W., van Wanrooij, L. L., van Charante, E. P. M., Brayne, C., van Gool, W. A., & Richard, E., (2018), Association of apathy with risk of incident dementia: a systematic review and meta-analysis, *JAMA Psychiatry*, *75*, 1012–1021, https://api.semanticscholar.org/CorpusID:51702943

Wager, T. D., & Woo, C.-W., (2017), Imaging biomarkers and biotypes for depression, *Nature Medicine*, *23*, 16–17, https://api.semanticscholar.org/CorpusID:4007919

Wasserthal, J., et al., (2018a), Tractseg - fast and accurate white matter tract segmentation, *NeuroImage*, *183*, 239–253, https://doi.org/https://doi.org/10.1016/j.neuroimage.2018.07.070

Wasserthal, J., Neher, P., & Maier-Hein, K., (2018b), Tractseg-fast and accurate white matter tract segmentation, *NeuroImage*, *183*, 239–253.

Wasserthal, J., Neher, P., Hirjak, D., & Maier-Hein, K., (2019), Combined tract segmentation and orientation mapping for bundle-specific tractography, *Medical image analysis*, *58*, 101559, https://api.semanticscholar.org/CorpusID:59336306

Wasserthal, J., Neher, P., & Maier-Hein, K., (2018c), Tractseg - fast and accurate white matter tract segmentation, *Neuroimage*, *183*, 239–253, https://api.semanticscholar.org/CorpusID:29170530

Wasserthal Jakob, M.-H. K., Neher Peter, (2018), High quality white matter reference tracts (1.2.0) [data set], *Zenodo*, https://doi.org/10.5281/zenodo.1477956

Wedeen, V., Wang, R., Schmahmann, J., Benner, T., Tseng, W., Dai, G., Pandya, D., Hagmann, P., D'Arceuil, H., & de Crespigny, A., (2008), Diffusion spectrum magnetic resonance imaging (dsi) tractography of crossing fibers, *NeuroImage*, *414*, 1267–1277, https://doi.org/https://doi.org/10.1016/j.neuroimage.2008.03.036

Wheeler-Kingshott, C. A. M., & Cercignani, M., (2009), About "axial" and "radial" diffusivities, *Magnetic Resonance in Medicine*, *61*, https://api.semanticscholar.org/CorpusID:1401715

Wu, X., Xu, Q., Xu, L., Zhou, J., Anderson, A. W., & Ding, Z., (2009), Genetic white matter fiber tractography with global optimization, *Journal of Neuroscience Methods*, *184*, 375–379, https://api.semanticscholar.org/CorpusID:1827830

Yang, Q., Huang, X.-R., Hong, N., & Yu, X., (2007), White matter microstructural abnormalities in late-life depression, *International Psychogeriatrics*, *19*, 757–766, https://api.semanticscholar.org/CorpusID:28620888

Yap, P., Gilmore, J. H., Lin, W., & Shen, D., (2011), Poptract: population-based tractography, *IEEE transactions on medical imaging*, *3010*, 1829–1840.

Yeatman, J. D., Dougherty, R. F., Myall, N. J., Wandell, B. A., & Feldman, H. M., (2012), Tract profiles of white matter properties: automating fiber-tract quantification, *PLoS ONE*, *7*, https://api.semanticscholar.org/CorpusID:10768676

Yendiki, A., Panneck, P., Srinivasan, P., Stevens, A., Zollei, L., Augustinack, J., Wang, R., Salat, D., Ehrlich, S., Behrens, T., et al., (2011), Automated probabilistic reconstruction of white-matter pathways in health and disease using an atlas of the underlying anatomy, *Frontiers in neuroinformatics*, *5*, 23.

Yuen, G. S., Bhutani, S., Lucas, B. J., Gunning, F. M., AbdelMalak, B., Seirup, J. K., Klimstra, S. A., & Alexopoulos, G. S., (2015), Apathy in late-life depression: common, persistent, and disabling., *The American journal of geriatric psychiatry : official journal of the American Association for Geriatric Psychiatry*, *23 5*, 488–94, https://api.semanticscholar.org/CorpusID:46173847

Zalesky, A., (2008), Dt-mri fiber tracking: a shortest paths approach, *IEEE Transactions on Medical Imaging*, *27*, 1458–1471, https://api.semanticscholar.org/CorpusID:10734587

Zalesky, A., Fornito, A., Cocchi, L., Gollo, L. L., van den Heuvel, M. P., & Breakspear, M., (2016), Connectome sensitivity or specificity: which is more important?, *NeuroImage*, *142*, 407–420, https://api.semanticscholar.org/CorpusID:21043401

Zhang, F., Hancock, E. R., Goodlett, C., & Gerig, G., (2009), Probabilistic white matter fiber tracking using particle filtering and von mises-fisher sampling, *Medical image analysis*, *13 1*, 5–18, https://api.semanticscholar.org/CorpusID:13243013

Zhang, F., Hoffmann, N., Karayumak, S. C., Rathi, Y., Golby, A. J., & O'Donnell, L. J., (2019), Deep white matter analysis: fast, consistent tractography segmentation across populations and dmri acquisitions, *Medical image computing and computer-assisted intervention : MICCAI ... International Conference on Medical Image*

Computing and Computer-Assisted Intervention, *11766*, 599–608, https://api.semanticscholar.org/CorpusID:204027881

Zhang, H., Schneider, T., Wheeler-Kingshott, C. A. M., & Alexander, D. C., (2012a), Noddi: practical in vivo neurite orientation dispersion and density imaging of the human brain, *NeuroImage*, *61*, 1000–1016, https://api.semanticscholar.org/CorpusID:10581162

Zhang, H., Schneider, T., Wheeler-Kingshott, C. A. M., & Alexander, D. C., (2012b), Noddi: practical in vivo neurite orientation dispersion and density imaging of the human brain., *NeuroImage*, *61 4*, 1000–1016, http://dblp.uni-trier.de/db/journals/neuroimage/neuroimage61.html#0005SWA12

Zhang, K., Johnson, B., Pennell, D., Ray, W. J., Sebastianelli, W. J., & Slobounov, S., (2010), Are functional deficits in concussed individuals consistent with white matter structural alterations: combined fmri & dti study, *Experimental Brain Research*, *204*, 57–70, https://api.semanticscholar.org/CorpusID:25853259

Zucchelli, M., Deslauriers-Gauthier, S., & Deriche, R., (2018), A closed-form solution of rotation invariant spherical harmonic features in diffusion mri, *Computational Diffusion MRI*, https://api.semanticscholar.org/CorpusID:125498468

COLLEGE MATHS, TELECOMS
DOCTORAL INFORMATIQUE, SIGNAL
BRETAGNE SYSTEMES, ELECTRONIQUE

Université de Rennes

Titre : Tractographie informée par l'anatomie et la microstructure pour l'évaluation de la connectivité dans les pathologies neurologiques

Mot clés : IRM de diffusion, A priori anatomiques, Tractographie, Tractometrie

Résumé : La tractographie de la matière blanche cérébrale est une méthode très prometteuse pour l'évaluation des trajectoires des fibres nerveuses, à partir d'IRM de diffusion (IRMd). En utilisant des méthodes d'analyse novatrices, elle permet d'estimer une veritable cartographie anatomique et fonctionnelle. L'avancement des techniques IRM a grandement amélioré notre capacité à quantifier la structure des réseaux cérébraux, accélérant ainsi la compréhension des altérations liées aux maladies. Malgré cela, de telles approches de tractographie restent encore limitées pour diverses raisons. En effet, des eudes ont indiqué que les algorithmes de tractographie les plus avancés ont tendance à generer un grand nombre de faisceaux de fibres, ce qui entraîne par conséquent un taux élevé de faux positifs. Dans cette thèse, notre objectif a été de proposer des méthodes innovantes pour améliorer l'estimation des fibres.

Nous nous sommes, dans un premier temps, intéressés au développement d'une méthode visant à guider les algorithmes de tractographie en utilisant des a priori anatomiques, basés sur des « Orientation Distribution functions » (ODF), avec pour objectif d'améliorer l'estimation des fibres dans des régions complexes. Cette méthode utilise des a priori anatomiques, exprimés sous la forme de "Track Orientation Distribution (TOD)" calculés à partir d'atlas de fibres segmentées. Cette approche permet ainsi de mieux caractériser la variabilité de la microstructure entre les individus. Durant l'étape de tractographie, les données IRMd et les a priori TOD sont combinés à l'aide de géométrie Riemannienne améliorant l'estimation de la fibre dans des régions complexes. Des études, à la fois sur données IRMd simulées et sur données réelles hautes qualités, ont montré que l'ajout d' a priori anatomique augmente de façon significative la qualité de l'estimation des faisceaux dans les régions de croisement de fibres.

Nous avons ensuite testé nos approches sur une cohorte clinique de patients atteints de dépression résistante afin d'identifier des biomarqueurs de cette pathologie. Pour cela, nous avons réalisé des analyses multivariées des métriques de microstructure extraites des modèles ODF le long des fibres. Nous avons identifié des modifications sur plusieurs faisceaux de fibres associées à la résistance au traitement. Cette étude nous a permis de monter que l'ajout d'a priori anatomiques peut servir à guider les algorithmes de tractographie de données cliniques de basses résolutions.

En parallèle à ce travail, nous avons développé une nouvelle métrique de comparaison de tractogrammes, basée sur la théorie de transport optimale et sur la distance de Wasserstein. Notre étude montre que l'utilisation de cette métrique donne des informations complémentaires à celles couramment utilisées (score de Dice, corrélation). En effet, cette mesure permet de mesurer une distance entre chaque fibre du tractogramme.

Title: Anatomically and microstructure-informed tractography for connectivity assessment in neurological pathologies

Keywords: Diffusion MRI, Anatomicals priors, Tractography, Tractometry

Abstract: White matter tractography is a highly promising method for assessing the trajectories of nerve fibers in the brain, based on diffusion MRI (dMRI). Using innovative analysis methods, it enables us to estimate a true anatomical and functional map. Advances in MRI techniques have greatly improved our ability to quantify the structure of brain networks, accelerating our understanding of disease-related alterations. Despite this, such tractography approaches remain limited for a variety of reasons. Indeed, studies have shown that the most advanced tractography algorithms tend to generate a large number of fiber bundles, resulting in a high false-positive rate. In this thesis, our aim was to propose innovative methods for improving fiber estimation.

We first developed a method to guide tractography algorithms using priors, based on Orientation Distribution functions (ODF), with the aim of improving fiber estimation in complex brain regions. This method uses anatomical priors, expressed as Track Orientation Distribution (TOD) from segmented fiber atlases. This approach enables us to better characterize microstructure variability between individuals. During the tracking stage, dMRI data and TOD priors are combined using Riemannian geometry to improve fiber estimation in complex regions. Studies, both on simulated dMRI data and on high-quality real data, have shown that the addition of anatomical a priori significantly increases the quality of bundles estimation in fiber crossing regions.

We then tested our approaches on a clinical cohort of patients with resistant depression to identify biomarkers of this pathology. To this end, we performed multivariate analyses of microstructure metrics extracted from ODF models along fibers. We identified changes in several fiber bundles associated with resistance to treatment. This study enabled us to show that the addition of anatomical priors can be used to guide algorithms for tractography of low-resolution clinical data.

In parallel with this work, we have developed a new metric for comparing tractograms, based on optimal transport theory and Wasserstein distance. Our study shows that the use of this metric provides complementary information to those commonly used (Dice score, correlation). In fact, this metric measures the distance between each fiber in the tractogram.